

POLITECNICO DI TORINO

Faculty of Engineering

Department of Mechanical and Aerospace Engineering

Master's Degree in Mechanical Engineering



**Politecnico
di Torino**

Master's Degree Thesis

**Residual Stress Characterization in Gears:
"DIC Analysis"**

Supervisors

Prof. Francesca CURÀ

Prof. Luca CORSARO

Prof. Andrea MURA

Prof. Raffaella SESANA

Candidate

Amair REVILLA

25/07/2023

A.Y 2022/2023

Abstract

The thesis study focuses on the innovative use of the Digital Image Correlation (DIC) technique, particularly 3D image correlation (3D-DIC or stereo-DIC), applied to measuring displacements, local deformation fields, and stresses in a sample during mechanical tensile and bending tests. DIC provides a full-field measurement capability without contact, unlike other Non-Destructive Techniques (NDT).

An experimental analysis was conducted to assess how the geometry of gear teeth affects the deformation field and stress distribution near the tooth root. For this purpose, dedicated equipment was used to perform a bending condition in the elastic field, and the deformations of the teeth of both standard and Thin-rim gears were monitored using the 3D Digital Image Correlation (DIC) technique.

Particular attention was paid to determining the most stressed point for both types of gears since establishing the position of the most stressed point and the corresponding equivalent stress value is essential for gear design.

A specific methodology was followed to perform a correct DIC analysis, proceeding with several steps. First, the cameras were positioned symmetrically, maintaining a certain distance between them. The angle formed between the cameras ensured a correct stereo angle, leading to better results. Additionally, a blue light source was positioned facing the sample to be analyzed.

This was followed by the preparation of the speckles, calibration with targets associated with the sample dimensions, and the execution of the test with DIC measurements. Finally, the DIC images are processed using the VIC 3D software.

The Stereo Vision technique, which involves the use of two Correlated Solutions cameras for 3D-DIC analysis, was more than sufficient to track the behavior of materials during a mechanical bending test, overcoming alignment problems and compensating for any errors during the calibration and images acquisition process.

Subsequently, this method was applied to examine residual stresses in gears subjected to shot peening surface treatment. Generally, a gear that presents residual stresses following

shot peening could show slightly improved bending resistance.

The deformation fields due to bending, evaluated during the experimental process and acquired using the digital image correlation technique, were compared with both the results derived from a finite element model and a theoretical trend according to ISO 6336-3 Standard. This comparison allowed for a full understanding of the stress and deformation conditions characterizing the material's behavior.

In conclusion, the implementation of the Digital Image Correlation (DIC) technique has allowed a thorough understanding of deformation maps and principal stresses in gears. This study highlighted how geometric parameters can influence the position of the point of maximum stress at the base of the tooth. These results, both reliable and accurate, lay the groundwork for further research and applications in the optimization of gear design and lifecycle.

Keywords: Digital Image Correlation; Residual Stress; Stereo Calibration; Shot peening; 2D analysis; 3D analysis

Contents

Abstract	i
Contents	iii
Introduction	1
1 State of art	5
1.1 Residual stress	5
1.1.1 Shot peening's impact on RS	6
1.2 Destructive Techniques	9
1.3 Non Destructive Techniques	10
1.3.1 X-ray and neutron diffraction methods	10
1.3.2 Thermoelastic stress analysis	11
1.3.3 Holographic interferometry	14
1.4 Digital Image Correlation	15
1.4.1 Primary concepts	15
1.4.2 Pattern and subset	18
1.4.3 Correlation Criterion	21
1.4.4 Stereovision and 3D-DIC	21
2 Materials and Methods	27
2.1 Equipment	28
2.1.1 Cameras	28
2.1.2 Lens selection and extension tubes	30
2.1.3 DAQ Unit	32
2.1.4 Light Source	34
2.2 Software	36
2.3 Samples	41
2.3.1 Standard Gear	41

2.3.2	Thin-Rim Gear	42
2.4	Experimentation Preparation	43
2.4.1	Sample Preparation with Speckle Technique	43
2.4.2	Vertical Support and Punch	52
2.4.3	DIC Assembly	57
2.4.4	Sample Calibration	58
2.4.5	Brightness and Focus	61
2.5	Experimental 3D-DIC - Bending Test	63
2.5.1	ROI and Subset	66
2.5.2	Local Reference System	68
3	Experimental Results and Discussion	71
3.1	Standard Gear - Load 4	71
3.1.1	Local strain maps ϵ_{xx}	71
3.1.2	Local strain maps ϵ_{yy}	72
3.1.3	Local strain maps ϵ_{xy}	73
3.1.4	Local strain maps ϵ_1	74
3.1.5	Local strain maps ϵ_2	74
3.1.6	Local strain maps γ_1	75
3.2	Thin-Rim Gear - Load 4	76
3.2.1	Local strain maps ϵ_{xx}	76
3.2.2	Local strain maps ϵ_{yy}	77
3.2.3	Local strain maps ϵ_{xy}	78
3.2.4	Local strain maps ϵ_1	79
3.2.5	Local strain maps ϵ_2	80
3.2.6	Local strain maps γ_1	80
3.3	Shot-Peened Gear - Load 3	81
3.3.1	Local strain maps ϵ_{yy}	81
3.3.2	Local strain maps ϵ_1	82
3.3.3	Local strain maps γ_1	82
3.4	Non-Shot-Peened Gear - Load 3	82
3.4.1	Local strain maps ϵ_{yy}	83
3.4.2	Local strain maps ϵ_1	83
3.4.3	Local strain maps γ_1	84
3.5	Data Analysis - Load 4	84
3.5.1	Local strain maps ϵ_{xx}	84
3.5.2	Local strain maps ϵ_{yy}	86

3.5.3	Local strain maps ϵ_{xy}	88
3.5.4	Local strain maps ϵ_1	91
3.5.5	Local strain maps γ_1	94
3.5.6	Local strain maps $L_1(X = 0)$	96
4	Conclusions and future developments	101
	Bibliography	103
A	Appendix A	105
A.1	Experimental Results and Discussion	105
A.2	Standard Gear - Load 1	105
A.2.1	Local strain maps ϵ_{xx}	105
A.2.2	Local strain maps ϵ_{yy}	106
A.2.3	Local strain maps ϵ_{xy}	107
A.2.4	Local strain maps ϵ_1	108
A.2.5	Local strain maps ϵ_2	109
A.2.6	Local strain maps γ_1	110
A.3	Standard gear - Load 2	110
A.3.1	Local strain maps ϵ_{xx}	111
A.3.2	Local strain maps ϵ_{yy}	112
A.3.3	Local strain maps ϵ_{xy}	113
A.3.4	Local strain maps ϵ_1	114
A.3.5	Local strain maps ϵ_2	115
A.3.6	Local strain maps γ_1	116
A.4	Standard Gear - Load 3	116
A.4.1	Local strain maps ϵ_{xx}	117
A.4.2	Local strain maps ϵ_{yy}	118
A.4.3	Local strain maps ϵ_{xy}	119
A.4.4	Local strain maps ϵ_1	120
A.4.5	Local strain maps ϵ_2	121
A.4.6	Local strain maps γ_1	122
A.5	Thin-Rim- Gear - Load 1	122
A.5.1	Local strain maps ϵ_{xx}	123
A.5.2	Local strain maps ϵ_{yy}	124

A.5.3	Local strain maps ϵ_{xy}	125
A.5.4	Local strain maps ϵ_1	126
A.5.5	Local strain maps ϵ_2	127
A.5.6	Local strain maps γ_1	128
A.6	Thin-rim Gear - Load 2	128
A.6.1	Local strain maps ϵ_{xx}	129
A.6.2	Local strain maps ϵ_{yy}	130
A.6.3	Local strain maps ϵ_{xy}	131
A.6.4	Local strain maps ϵ_1	132
A.6.5	Local strain maps ϵ_2	133
A.6.6	Local strain maps γ_1	134
A.7	Thin-Rim Gear - Load 3	134
A.7.1	Local strain maps ϵ_{xx}	135
A.7.2	Local strain maps ϵ_{yy}	136
A.7.3	Local strain maps ϵ_{xy}	137
A.7.4	Local strain maps ϵ_1	138
A.7.5	Local strain maps ϵ_2	139
A.7.6	Local strain maps γ_1	140
A.8	Shot-Peened Gear - Load 1	140
A.8.1	Local strain maps ϵ_{yy}	141
A.8.2	Local strain maps ϵ_1	141
A.8.3	Local strain maps γ_1	142
A.9	Shot-Peened Gear - Load 2	142
A.9.1	Local strain maps ϵ_{yy}	142
A.9.2	Local strain maps ϵ_1	143
A.9.3	Local strain maps γ_1	143
A.10	Non-Shot-Peened Gear - Load 1	143
A.10.1	Local strain maps ϵ_{yy}	144
A.10.2	Local strain maps ϵ_1	144
A.10.3	Local strain maps γ_1	145
A.11	Non-Shot-Peened Gear - Load 2	145
A.11.1	Local strain maps ϵ_{yy}	145
A.11.2	Local strain maps ϵ_1	146
A.11.3	Local strain maps γ_1	146
A.12	Load Analysis	146
A.13	Standard Gear - Load 3	146
A.13.1	Local strain maps ϵ_{xx}	147

A.13.2	Local strain maps ϵ_{yy}	147
A.13.3	Local strain maps ϵ_{xy}	147
A.13.4	Local strain maps ϵ_1	148
A.13.5	Local strain maps γ_1	148
A.13.6	Local strain maps $1(X = 0)$	149
A.14	Standard Gear - Load 4	149
A.14.1	Local strain maps ϵ_{xx}	150
A.14.2	Local strain maps ϵ_{yy}	150
A.14.3	Local strain maps ϵ_{xy}	151
A.14.4	Local strain maps ϵ_1	151
A.14.5	Local strain maps γ_1	152
A.14.6	Local strain maps $1(X = 0)$	152
A.15	Thin Rim Gear - Load 3	153
A.15.1	Local strain maps ϵ_{xx}	153
A.15.2	Local strain maps ϵ_{yy}	154
A.15.3	Local strain maps ϵ_{xy}	154
A.15.4	Local strain maps γ_1	155
A.15.5	Local strain maps $1(X = 0)$	155
A.16	Thin Rim Gear - Load 4	156
A.16.1	Local strain maps ϵ_{xx}	156
A.16.2	Local strain maps ϵ_{yy}	157
A.16.3	Local strain maps ϵ_1	157
A.16.4	Local strain maps γ_1	158
A.16.5	Local strain maps $1(X = 0)$	158
A.17	Comparison with FEM results	159
List of Figures		161
List of Tables		167
List of Symbols		169
Acknowledgements		171

Introduction

Residual stress analysis is a crucial step in the design of structural elements and in estimating their reliability. To predict the behavior of a system, the most commonly used failure criteria involve stress, either individually or in combination with the geometric parameters of the object.[18]

In the context of bending failure in gears, crack nucleation and propagation are influenced by various factors that can be classified into geometric factors and load factors. Geometric factors include parameters such as rim thickness, web thickness, and gear configuration. Load factors include the effect of centrifugal loads. In the case of bending loading conditions, lightweight gears exhibit a complex strain and stress distribution due to their unique geometry. Understanding the position of the most stressed point and determining the corresponding equivalent stress value is crucial, particularly during the design phase, to predict the potential path of crack propagation reliably. By analyzing the stress and strain fields, engineers can identify critical locations on the gear where crack nucleation is likely to occur. This information helps in designing the gear with appropriate material selection, geometry optimization, and load distribution to minimize stress concentrations and reduce the likelihood of crack initiation. The equivalent stress value provides a measure of the maximum stress experienced at a specific location on the gear. This value is essential in assessing the gear's strength and determining its resistance to failure. By comparing the equivalent stress with the material's fatigue strength, it can estimate the gear's durability and predict its fatigue life under cyclic bending loads.[6]

Stiff or dynamic extensometers offer precise strain measurements but are limited to a 5% strain measurement range. On the other hand, soft or static extensometers can measure larger strains up to 50%, but with less precision compared to their stiff/dynamic counterparts. One of the key assumptions of traditional extensometers is the uniformity of deformation, meaning they can only measure the average strain within the gauge length and do not provide information about strain distribution between two knife points. To overcome these limitations, a digital image correlation (DIC) system has been employed. DIC allows for the measurement of the full-range strain distribution at the macroscopic level during a tensile test, which is not possible with conventional extensometers. DIC

provides a point-by-point strain field, whereas traditional methods only provide uniform strain measurements. DIC offers several advantages, including the ability to measure displacement at thousands of points on the specimen's surface. It also utilizes a normal white light source instead of lasers, which can be considered a positive quality of the DIC technique.[21]

DIC (Digital Image Correlation) is a non-contact optical method used for measuring full-field displacement and deformation. It enables the acquisition of a map or image showing the distribution of displacements and deformations across the component being examined. [12] DIC involves comparing digital images from the unloaded state to various loading conditions, tracking surface patterns to evaluate displacement fields and obtaining strain fields through differentiation. DIC can measure planar displacements and strains (2D-DIC) using a single camera or obtain the full spatial field, including out-of-plane displacements (3D-DIC), by using stereoscopic vision. DIC is versatile and can be applied to different scales, from microscopic to macroscopic specimens (from 10^{-9} m to 10^2 m).[7] DIC is part of the family of non-destructive techniques, which are used to investigate the local behavior of a material without causing any alteration or removal from the structure being examined. These techniques are primarily applied to identify the causes of failure in solid components and to determine preventive measures to avoid such failures. The automobile industry has an increasing demand for lightweight components, improved product performance, efficiency and increased safety. To meet these demands, it is crucial to optimize the design and manufacturing processes by accurately measuring critical material properties such as strain limit, strength coefficients, and anisotropy coefficients. In the modern manufacturing industry, there is a growing need for high-strength materials to achieve more economical and lightweight products. These new materials require testing to determine their material properties for production purposes. Tensile testing, which includes measuring the stress-strain relationship, is crucial for various material processing techniques like stretching, stamping, and bending. By employing DIC, manufacturers can gain a deeper understanding of material behavior, optimize their designs, and make informed decisions about material processing techniques. DIC offers a more comprehensive and accurate assessment of strain and displacement, aiding in the development of stronger, more efficient, and safer automotive components.[17]

In the modern gear industry, the assessment of gear load capacity is commonly done using either standard rating methods or traditional design rules. This approach involves computing nominal values to describe the stress field within the gear. These values are then juxtaposed with limit values, which are derived from tests conducted on gears. The evaluation of tooth bending strength typically employs a cantilever-beam model for the determination of bending stress. This approach dates back to 1892, when the engineer

Wilfred Lewis first computed the tooth root stress of spur gear teeth. This model remains a fundamental basis for the standard calculation methods used in gear design today. Nevertheless, the actual stress state, or the "true" stress, present in the tooth root fillet can differ from the nominal values computed using this method. In essence, the computation of the highest tensile stress at the tooth root is a complex three-dimensional issue. The plane strain or plane stress model can be used without approximations only in the case of infinite, or infinitesimal, face width.[5]

The thesis work focuses on validating the Digital Image Correlation (DIC) technique for characterizing the behavior of materials. The methodology uses gears with different geometries as samples and compares their theoretical behaviors with the experimental ones obtained through DIC during bending tests. This comparison will allow assessing the accuracy and reliability of the technique by characterizing some of the significant geometric parameters in stress distribution due to bending. The CFR (Fiat Research Center) provided the research group with a shot-peened gear and a non-shot peened gear with the aim of finding a non-destructive technique to determine the maximum value of RS with accurate results. These gears are unique because they are placed within the automobile transmission system and are therefore subjected to high cycle fatigue, cracking, fracture, plastic deformation, wear, scuffing. The main objective of the thesis is to develop a practical, fast, and cost-effective method to assess the accuracy of DIC (Digital Image Correlation). This includes defining accuracy evaluation metrics, creating a reference dataset for comparing DIC measurements and developing procedures for DIC system calibration. Additionally, the thesis evaluates the effects of different data pre-processing operations on the quality of measurements. These pre-processing operations include noise reduction, lighting correction, image registration, and pattern quality. Through the analysis of these operations, it will be possible to understand their impact on the precision and reliability of the results obtained with DIC.

The following chapters are organized in this way: first, the state of art of residual stress measurement techniques, both destructive and non-destructive, will be described. A deepening on DIC functioning is carried out, describing primary concepts like pattern, subset, and matching, attentioning over all the 3D-DIC based on stereovision method. In the second chapter, materials and methods will be presented more specifically: it includes the equipment (cameras, lenses and DAQ Unit), softwares and the four types of sample used for the experimentation (standard gear, thin-rim gear, shot-peened gear and non-shot-peened gear). Then, the experimentation will be described with a focus on the experimental preparation with two fundamental steps such as speckle technique and sam-

ple calibration. Subsequently, the bending test and experimental 3D-DIC analysis will be shown. The third chapter focuses on the presentation of the collected data and the discussion and critical interpretation of these results. In detail, local strain maps of four loads for each type of studied gear will be presented, with a subsection that allows direct comparison between standard and thin-rim gear on the fourth load. Furthermore, the comparison with Finite Element Method (FEM) results will be highlighted. Finally in the conclusion, future developments are proposed.

1 | State of art

1.1. Residual stress

The study of Residual Stress (RS) is a well-established field in engineering and research due to its significant impact on the strength, hardness, fracture toughness, fatigue resistance, and other material properties. Residual stress refers to the internal stresses present in a material without the influence of external loading or thermal gradients. These stresses are self-equilibrating, meaning they reach a state of balance within the material. However, unlike live stresses, residual stresses are often the result of complex thermo-mechanical or chemical inelastic processes. Consequently, residual stress can be considered a partial reflection of the entire deformation history of the object. The study of residual stress provides valuable insights into the mechanical behavior and performance of materials, aiding in the optimization of design and manufacturing processes. The literature describes three types of residual stress (Figura 1.1): macro RS, which develop in the body of a component on a larger scale; micro RS, which vary on the scale of an individual grain; and micro RS, which exist within a grain.

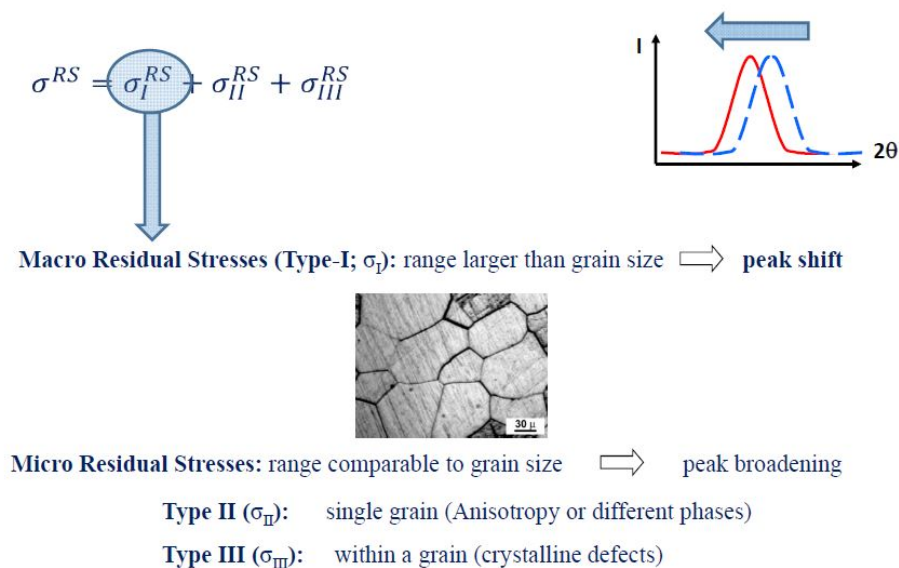


Figure 1.1: Types of Residual Stress (from biofotonica.it)

Residual stress originates from various deformation processes such as heat treatment, shape transformation, or changes in material properties. For instance, processes like welding, machining, grinding, or wire drawing can introduce tensile residual stresses, which are generally detrimental and often the leading cause of fatigue failure and stress-corrosion cracking. Conversely, peening processes (such as shot peening, hammer peening, laser peening, or ultrasonic peening) induce compressive residual stresses that are typically beneficial. Compressive residual stresses help prevent the initiation and propagation of fatigue cracks and enhance corrosion resistance.

Given these factors, it is essential to determine, analyze, and manage residual stress using the approach known as Residual Stress Management (RSM). RSM consists of three stages:

1. Residual stress determination through measurement (destructive and non-destructive) and computational methods;
2. Analysis of the effects of residual stress through experimental studies;
3. Modification of residual stress, if necessary, through changes in manufacturing/assembly techniques or the application of stress-relieving methods. [18]

1.1.1. Shot peening's impact on RS

Gear engineers play a crucial role in designing and improving gear systems by considering various factors. Surface treatment, including shot peening, is an important aspect that can significantly enhance the bending and contact fatigue properties of gears when implemented correctly. By introducing residual compressive stresses through shot peening, the gear's fatigue resistance can be improved. Compressive stresses help to counteract the tensile stresses that are generated during gear operation, especially under bending and contact fatigue conditions. The presence of compressive stresses reduces the likelihood of crack initiation and propagation, enhancing the gear's fatigue life and durability. [4]

Shot peening is a mechanical surface treatment process that involves bombarding a metal surface with small spherical particles, known as shot, at high velocities. The impact of these shots induces compressive residual stresses in the surface layer of the material (Figure 1.2), which helps to improve its resistance to fatigue and other failure mechanisms.[8]

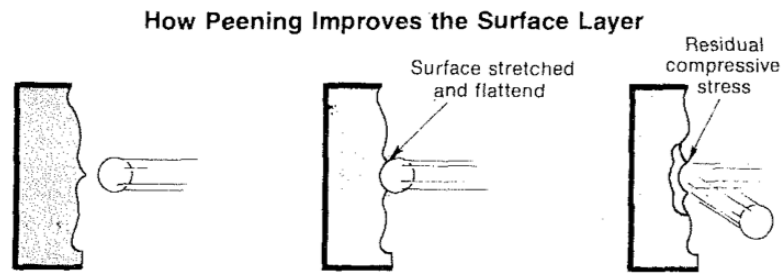


Figure 1.2: Shot peening process [8]

By subjecting gear teeth and other critical components to shot peening, the surface layer is hardened and residual compressive stresses are introduced, which counteract the tensile stresses that can lead to fatigue failure. New designs for agricultural machinery, speed reducers, and gear motors are now incorporating shot peening into their initial design stages. This trend is driven by the desire to improve the durability and reliability of these components, especially when they are subjected to cyclic loading and high-stress conditions.[8]

The stress distribution through the cross-section of a part can be shown as in Figure 1.3.

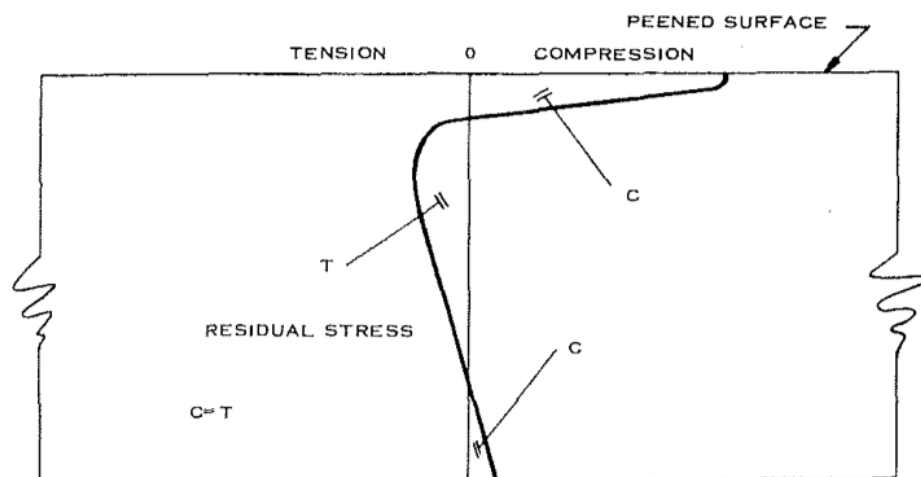


Figure 1.3: Distribution of stress in a shot-peened beam with no external Load [8]

In [8] the author explains: «When a part that has been peened has an external load applied to it, the off-setting tensile stress produced by the load will decrease the magnitude of the compressive stress introduced by the peening. This compressive stress will be retained if the part is loaded no more than 40 to 50 per cent of the ultimate tensile strength of the material or below the elastic limit or yield point.»

For example for a material with a hardness of Rc31, the part has the stress distribution shown without an external load. Upon application of the load, the curve will shift as shown in Figure 1.4.

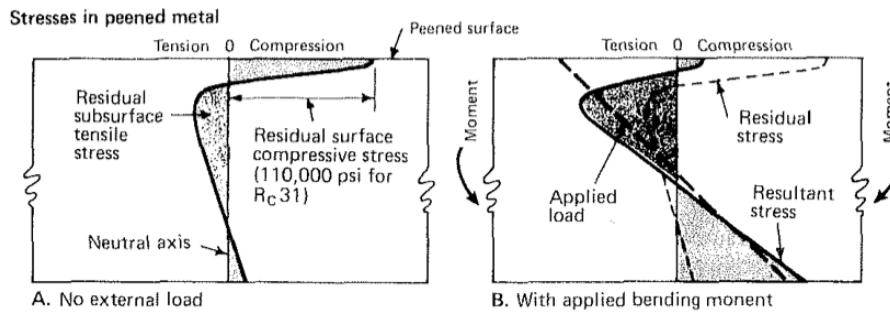


Figure 1.4: Peening continues to protect the surface from fatigue as long as tensile stress from applied load are less than residual stresses. [8]

The gear tooth is modeled as a cantilevered beam, hence a failure due to a cyclical load occurs at the root of the gear. The most significant effects of shot peening are, in fact, to improve the fatigue strength in the root fillet, and to increase surface fatigue life to reduce pitting (Figure 1.5)

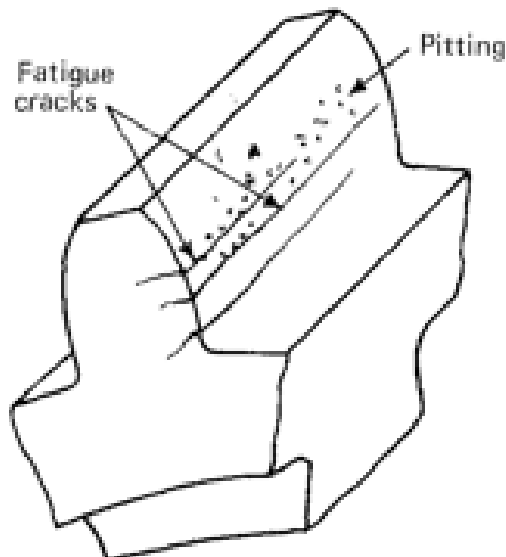


Figure 1.5: Tensile and shear stresses cause pits and fatigue cracks.[8]

1.2. Destructive Techniques

Destructive techniques involve disrupting the state of balance of residual stress in the specimen after a deformation process. These techniques, such as sectioning, machining, layer removal, or hole drilling, induce local strains that can be measured to determine the residual stress field.

One commonly used destructive method is the hole drilling method. It involves drilling a small hole in the sample and measuring the surface strain relief in the material surrounding the hole using a strain gauge rosette. This method provides valuable information about the residual stress distribution.

Another destructive method, similar to hole drilling, is the ring core method. Instead of drilling a hole, a ring-shaped hole is created, and the measurements are taken on the surface inside the ring. This method offers an alternative approach to assess the residual stress state in a specimen. Both the hole drilling method and the ring core method are effective in determining residual stress by analyzing the strain relief resulting from the introduced disruptions in the material.[18]

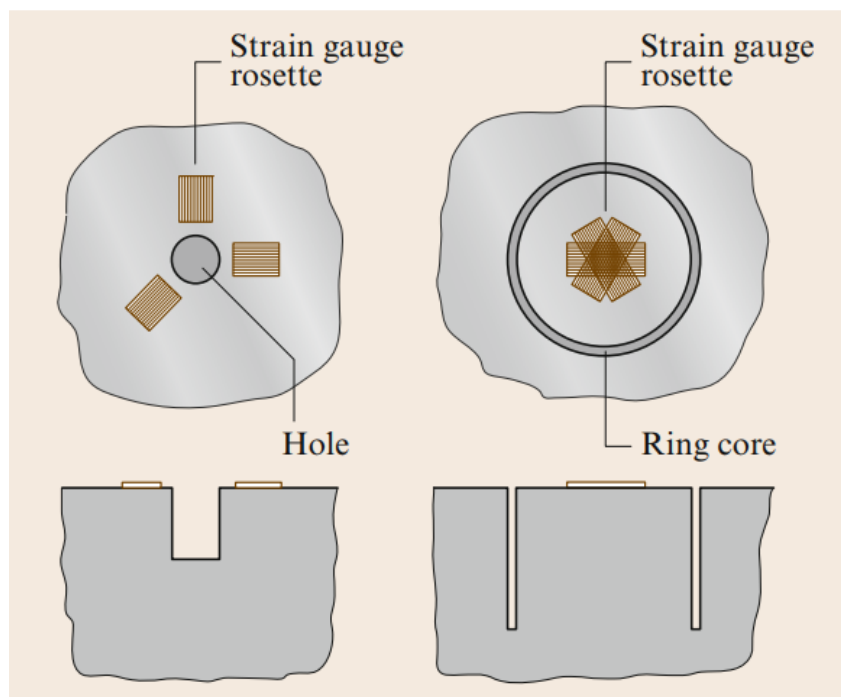


Figure 1.6: Application of hole-drilling and ring core methods [18]

1.3. Non Destructive Techniques

Non-destructive techniques (NDT) are another essential aspect of Residual Stress Management (RSM) that does not involve the destruction of the specimen. These techniques allow for the investigation of the local behavior of a material without altering or removing it from the structure being examined. As a result, NDT methods can be used for field measurements and assessments. NDT techniques rely on establishing a relationship between physical parameters and residual stress to obtain valuable information about the material's internal stress state.[18]

1.3.1. X-ray and neutron diffraction methods

These methods are non-destructive testing (NDT) techniques that utilize lattice spacing as the strain gauge. The x-ray method is the most commonly employed technique for Residual Stress Management (RSM). However, it has limitations related to sample geometry. Specifically, the measurement area must be accessible to x-rays, allowing for diffraction to reach the detector without encountering any obstructions. X-ray diffraction offers a spatial resolution ranging from 1-2 mm down to tens of microns, and it can penetrate a depth of approximately 10-30 μm depending on the material and the x-ray source.[18]

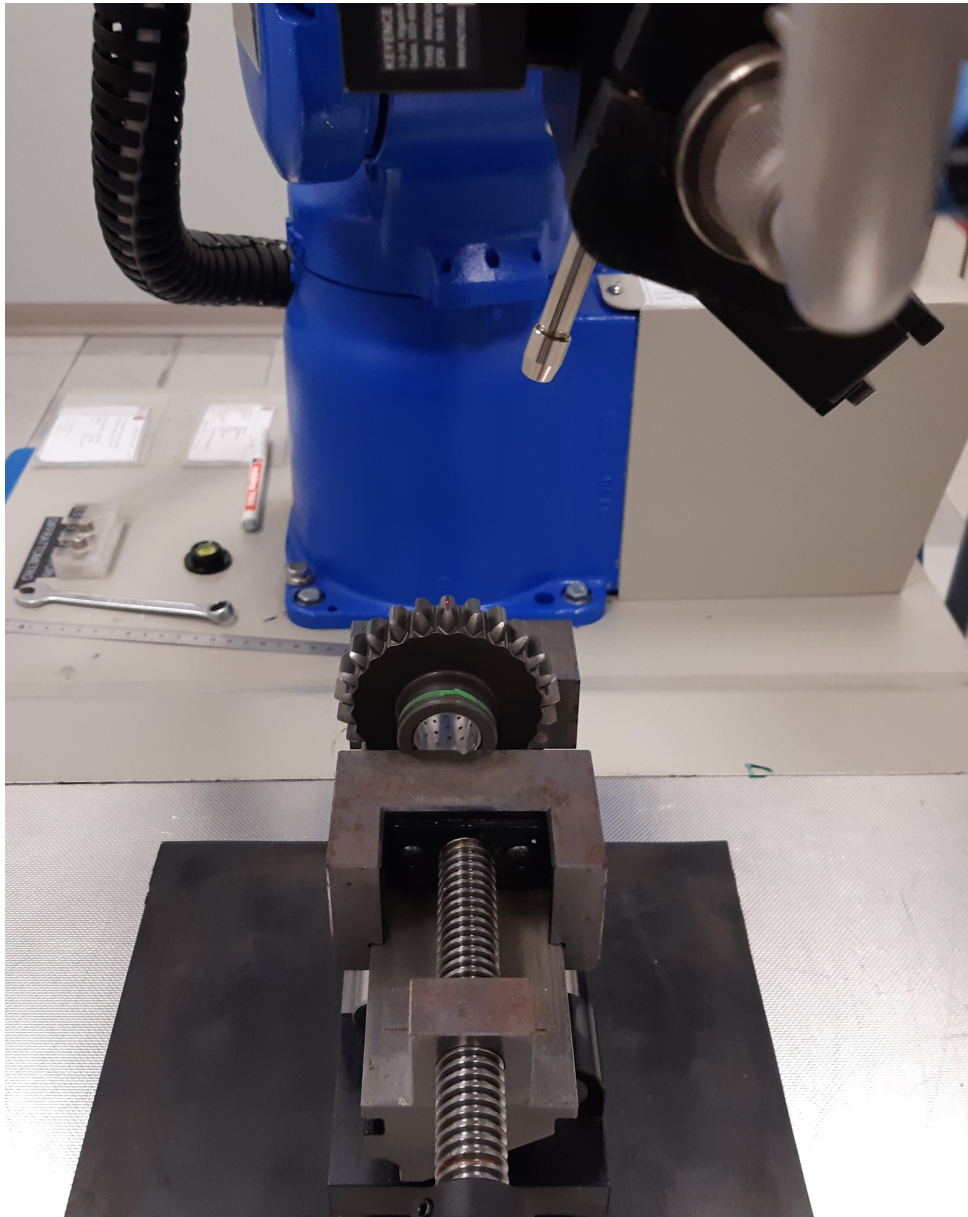


Figure 1.7: Diffractometer

1.3.2. Thermoelastic stress analysis

When a specimen is subjected to cyclic stresses under adiabatic conditions (meaning minimal heat exchange with the surroundings), it experiences a small cyclic temperature change (ΔT). This temperature change can be related to the change in the sum of principal stresses ($\Delta(\sigma_1 + \sigma_2)$) according to following equation:

$$\Delta T = -(\alpha T_0 / \rho c P) \Delta(\sigma_1 + \sigma_2)$$

Here, α represents the coefficient of thermal expansion, T_0 is the absolute temperature,

ρ is the density of the material, and c_P is the specific heat capacity at constant pressure. This relationship assumes elastic stresses and isotropic material behavior, but it can be modified to account for orthotropic materials. Adiabatic conditions are typically achieved by cycling the stresses at frequencies ranging from approximately 10 to 25 Hz. The magnitude of ΔT can be quite small, often requiring measurement resolutions on the order of 0.001 °C. The temperature change ΔT results in the emission of infrared photons from the specimen's surface. This flux of photons is monitored using a highly sensitive infrared camera, which acts as a photon detector, producing a corresponding voltage signal. The change in the sum of principal stresses ($\Delta(\sigma_1 + \sigma_2)$) can be expressed in terms of the camera signal (S) using the following equation:

$$\Delta(\sigma_1 + \sigma_2) = AS$$

The constant A in this equation combines various parameters such as detector responsivity, system amplification, surface emissivity, etc., and can be determined through calibration. Thermoelastic stress data can be obtained over a desired surface region to map the distribution of stress. Thermoelastic stress analysis has found applications in various areas, including the determination of fracture mechanics parameters, detection and monitoring of crack growth, and evaluation of adhesive joint quality. Different methods have been developed to separate the individual principal stresses (σ_1 and σ_2) if desired. Additionally, in practical scenarios, a mean value of stress may be present. Experimental studies have shown that mean stress can influence the thermoelastic behavior of materials (Figure 1.8). A theory has been proposed to explain this effect, considering the temperature dependence of elastic constants such as the modulus of elasticity. If thermoelastic data can be analyzed to determine the mean stress separately from cyclic stress, there is the potential to evaluate residual stress (which can be considered a mean stress). However, the influence of mean stress on thermoelasticity is relatively small, making it challenging to reliably determine residual stresses using this technique (Figure 1.9). Research on the effect of mean stress in thermoelasticity continues, but as of now, the ability to accurately determine residual stresses through thermoelastic analysis remains to be demonstrated.[10]

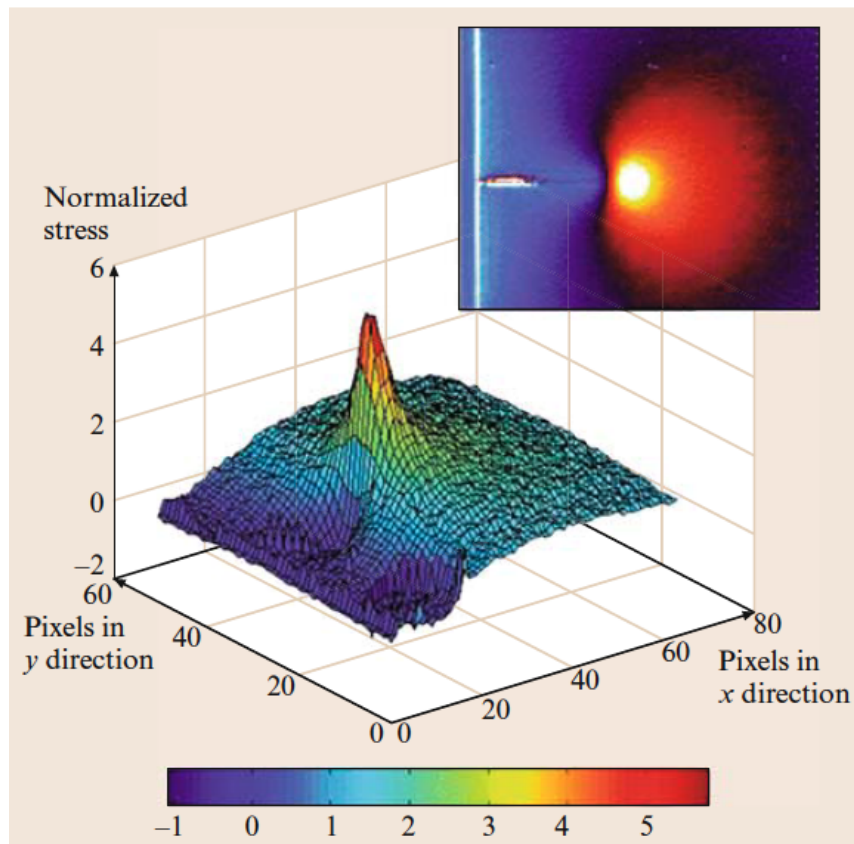


Figure 1.8: Typical thermoelastic image [18]

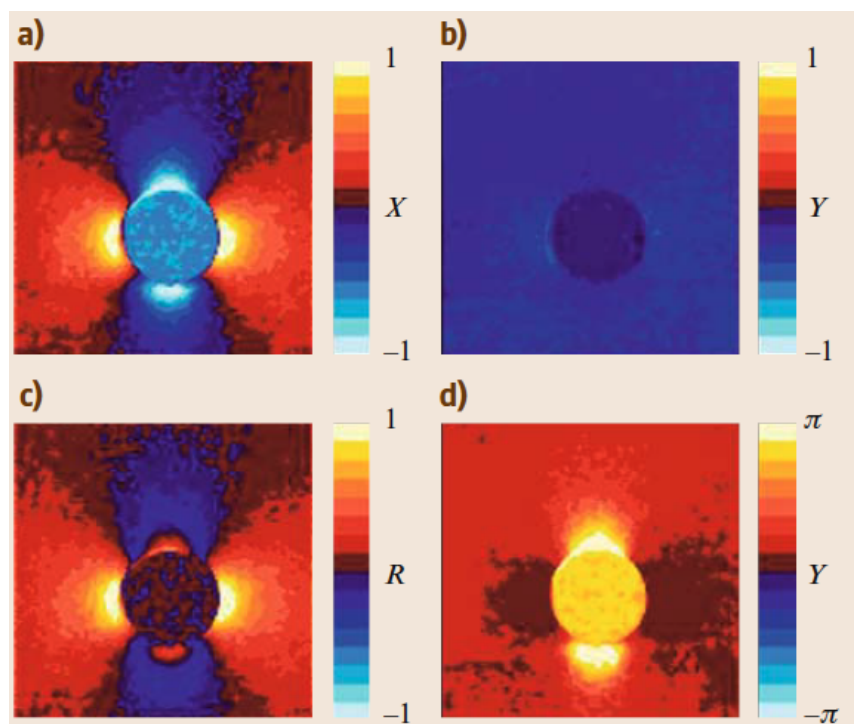


Figure 1.9: Thermoelastic response of a plate in uniaxial tension with a central hole [18]

1.3.3. Holographic interferometry

Holographic interferometry is a technique that allows for the measurement of surface displacements ranging from tens of nanometers to tens of microns. In this method, a laser beam illuminates the surface of a test object, and the scattered light is directed to a location where a hologram is generated. Reference light also illuminates the hologram location, and the interference between the reference and scattered light is recorded as an intensity distribution using analog or digital means.

Once a hologram is recorded, it can be re-illuminated with reference light, and a reconstructed image of the test object can be observed through the hologram, even if the object is removed. When the object remains in place and is re-illuminated, any microscopic deformation of the object's surface results in the combination of the reconstructed light and the scattered light, creating optical interference fringes on the object's surface as seen through the hologram.

These interference fringes represent phase differences, with each fringe corresponding to a phase difference of 2π relative to an adjacent fringe. By analyzing these phase differences, surface displacements can be determined. Fringes resulting from in-plane displacements are shown in Figure 1.10(b), while fringes resulting from out-of-plane displacements are shown in Figure 1.10(c). The phase differences and displacement relationships differ for in-plane and out-of-plane displacements.[10]

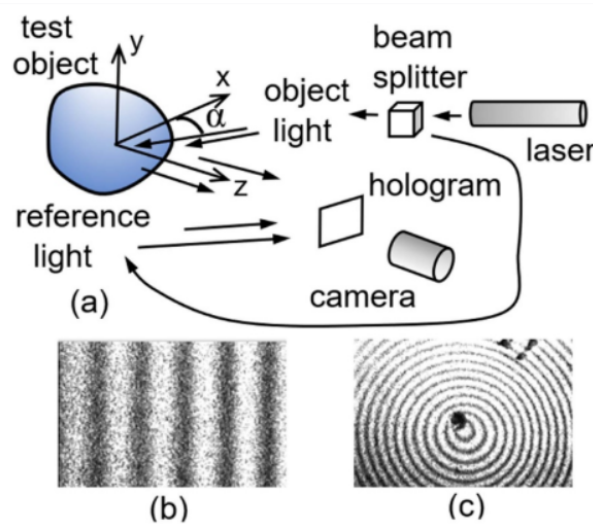


Figure 1.10: (a) Schematic of holographic interferometry set-up, (b) interference fringes from in-plane displacements of a thin plate, stretched uniformly and (c) fringes from out-of-plane displacements of a disc supported around its circumference and loaded by a force normal to its surface and slightly off-center. [10]

Digital holographic interferometry provides a digital alternative to analog holograms. It involves recording holographic interference patterns using a CCD or CMOS camera and storing them digitally. By numerically reconstructing the "before" and "after" holograms, phase information can be retrieved and used to calculate surface displacements. [10]

1.4. Digital Image Correlation

Digital image correlation (DIC) is a non-contact optical method used for measuring full-field displacement and deformation. As a prominent non-interferometric optical technique, DIC has gained widespread acceptance and is commonly employed as a versatile tool for surface deformation measurement in the field of experimental solid mechanics. The DIC method was initially developed by a group of researchers at the University of South Carolina in the 1980s. Over the years, significant improvements have been made to the DIC method, including reducing computation complexity, achieving high-accuracy deformation measurement, and expanding its application range. The classical DIC approach, known as 2D-DIC, utilizes a single fixed camera to measure the in-plane deformation of planar object surfaces. Subsequently, the development of 3D-DIC enables the measurement of objects with curved surfaces or three-dimensional deformations resulting from loading. [15]

3D-DIC relies on binocular stereovision, involving two cameras, and it can measure displacement fields and surface strain fields of any three-dimensional specimen. The advancements in DIC have made it a valuable tool for comprehensive deformation analysis, offering a non-contact and full-field measurement approach in solid mechanics research. [12]

1.4.1. Primary concepts

DIC (Digital Image Correlation) provides an alternative method to interferometric techniques for determining surface displacements. In 2D measurements, a digital camera is used to capture images of a surface region illuminated by ordinary light. The first step is to acquire and digitize an initial image of the region, known as the reference image. This image is then divided into smaller subsets, referred to as subsets, each of which should have features suitable for tracking their movement under loading. If necessary, additional features can be added, such as a random pattern of tiny black dots on a contrasting background (speckle).

After loading is applied, a second image is captured, and each deformed sub-set is matched to its corresponding subset in the reference image using a correlation algorithm. This

matching process allows for the determination of the displacements experienced by each subset.

For 3D measurements, instead, a stereovision setup is used with two cameras placed at a sufficient distance apart. The images acquired by these cameras enable the determination of the 3D coordinates of surface locations through triangulation.

Commercially available 2D and 3D DIC systems incorporate computational algorithms that track and match sub-sets, and subsequently calculate displacements and strains. Prior to using a DIC system, calibration is necessary. Calibration involves accounting for camera characteristics, such as distortion, and in the case of 3D DIC, the orientation of the cameras relative to each other. (Figure 1.11)

Compared to interferometric methods discussed earlier, DIC relaxes the requirement for stringent mechanical stability of the test setup, which is a significant advantage. However, the displacement sensitivity of DIC may be lower than that of interferometric approaches, depending on the specific implementation. [10]

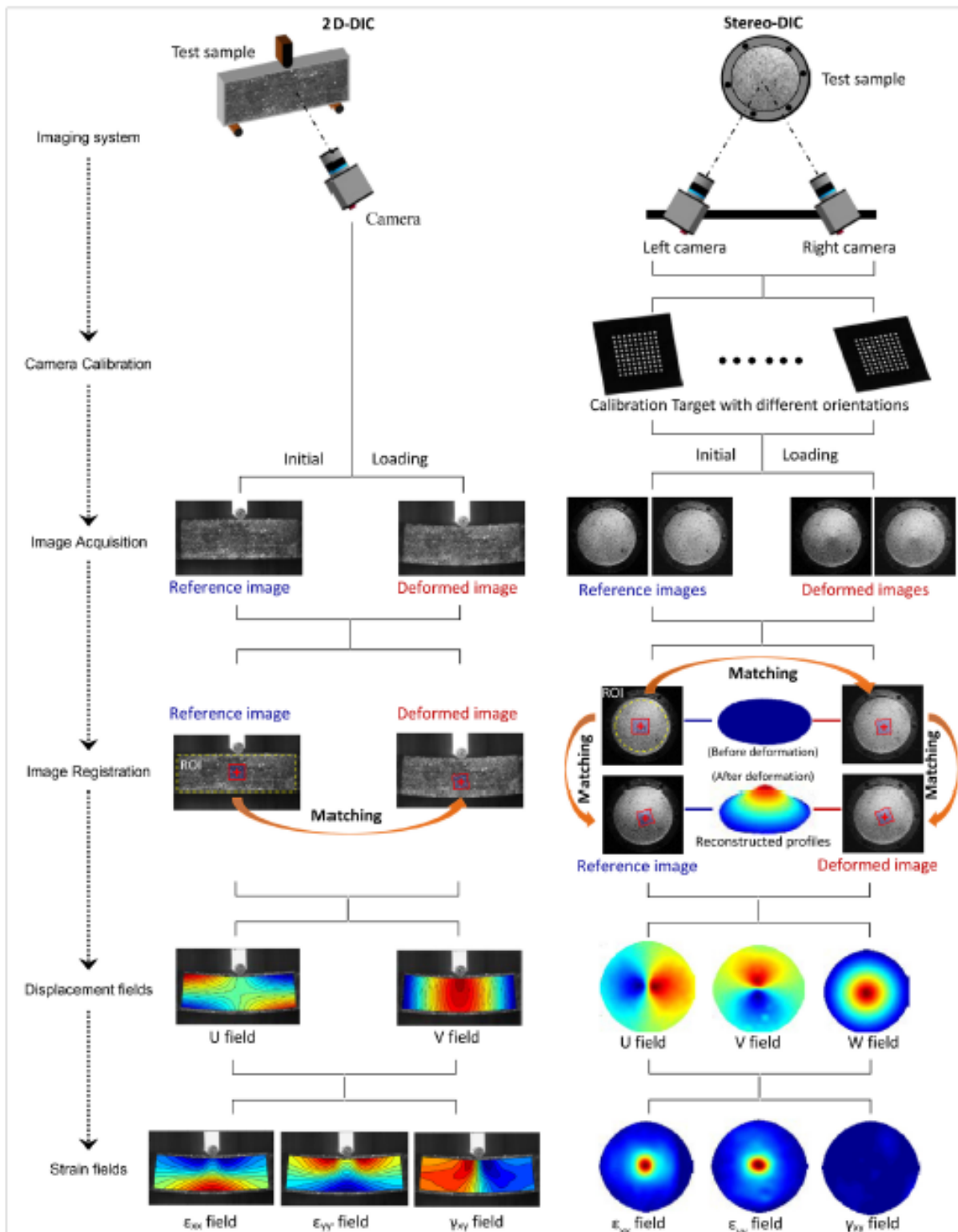


Figure 1.11: Implementation procedures of 2D-DIC and stereo-DIC techniques [15]

1.4.2. Pattern and subset

For the Digital Image Correlation (DIC) method to work accurately, the surface of the specimen needs to have a specific pattern. The DIC technique relies on non-uniform light reflection from the surface, which requires a pattern for tracking purposes. A uniform surface without features or light gradients would not be suitable for DIC. Therefore, it is necessary to have a random pattern on the specimen's surface that is integral to the material being observed and moves and strains with it.

In most cases, the test specimen does not naturally have a speckle pattern. To address this, a speckle pattern is often applied to the specimen's surface using an airbrush gun. A high-contrast speckle pattern is preferred to minimize noise, so a black-on-white pattern is commonly used.

In DIC, the pattern adheres to the surface and deforms with it. This means that as the object undergoes translations and deformations, the pattern on the surface also translates and deforms accordingly. This characteristic of the DIC pattern is crucial because it ensures that there is no loss of correlation between the reference pattern before deformation and the deformed pattern after deformation even under large translations and deformations. The ability of the pattern to deform with the surface allows for accurate tracking and measurement of displacements and strains across the entire field of view.[12] The subsets are shifted until the pattern in the deformed image matches the reference image as closely as possible; this match is calculated by the total difference in grey levels at each point (Figure 1.12) [19]

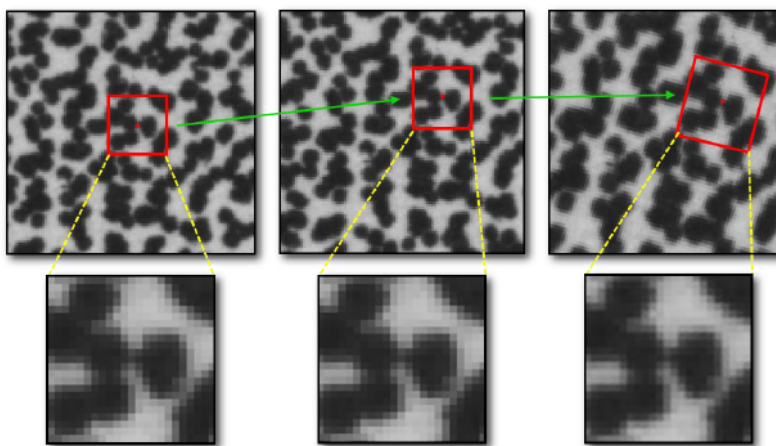


Figure 1.12: Visualization of subset tracking during movement and deformation [19]

To provide good tracking information, the speckle pattern should possess the following characteristics:

1. High Contrast: The speckle pattern should have a high contrast, which means using either dark black dots on a bright white background or bright white dots on a dark black background. This contrast helps in distinguishing and tracking the speckles accurately.
2. 50% Coverage: It is desirable to have approximately equal amounts of white and black on the surface, meaning the speckles should be evenly distributed.
3. For instance, if the speckles are 5 pixels in size, they should be approximately 5 pixels apart from one another. This distribution ensures that there is enough speckle coverage for reliable tracking.
4. Consistent Speckle Sizes: Ideally, the speckles should be 3-5 pixels in size to optimize spatial resolution. However, the most crucial aspect is consistency in size throughout the pattern. Speckles that are too small (less than 3 pixels) can lead to aliasing and inaccurate tracking results.
5. Isotropic: The speckle pattern should not exhibit a bias or preference for any particular orientation. In other words, there should be no discernible directional pattern in the arrangement of speckles. This isotropy helps prevent tracking errors that may occur due to a biased pattern.
6. Randomness: It is important for the speckle pattern to be random. While it is challenging to achieve a perfectly regular pattern that could cause false matching, even repeating patterns can lead to irregularities. When using templates or stencils with repeating dots, it is crucial that the paint seeping through the stencil is irregular enough to avoid false tracking caused by a predictable pattern.[19]

Some examples of speckle patterns are shown in Figure 1.13.

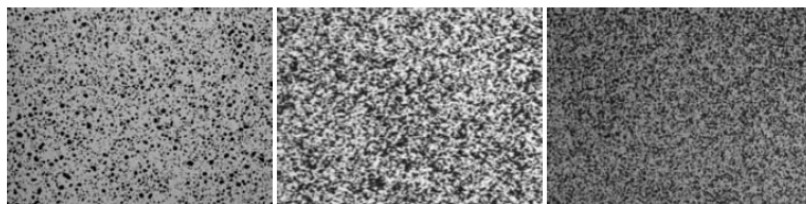


Figure 1.13: Example of typical speckle patterns [12]

The process of 2D DIC (Digital Image Correlation) involves the following steps:

1. Selection of Reference Subset: A square subset of pixels centered at point $P(x_0, y_0)$ is chosen from the reference image. This subset has a size of $(2M + 1) \times (2M + 1)$

pixels, where M determines the size of the subset.

2. Tracking the Corresponding Subset.
3. Similarity Evaluation: To evaluate the similarity between the reference subset and the deformed subset, a predefined correlation criterion is used. Common criteria include cross-correlation (CC) and sum-squared difference (SSD) correlation. These criteria measure the similarity of gray levels or pixel intensities between the two subsets.
4. Similarity Evaluation: To evaluate the similarity between the reference subset and the deformed subset, a predefined correlation criterion is used. Common criteria include cross-correlation (CC) and sum-squared difference (SSD) correlation. These criteria measure the similarity of gray levels or pixel intensities between the two subsets.
5. Matching Procedure: The matching procedure involves calculating the correlation coefficient or SSD value for different positions of the deformed subset in the deformed image. By searching for the peak position of the correlation coefficient or the minimum SSD value, the position of the deformed subset is determined.
6. Displacement Calculation: The displacement vector at point P is obtained by subtracting the position of the reference subset center from the position of the target subset center. This displacement vector represents the in-plane movement or displacement of point P between the reference and deformed images. (Figure 1.14) [16]

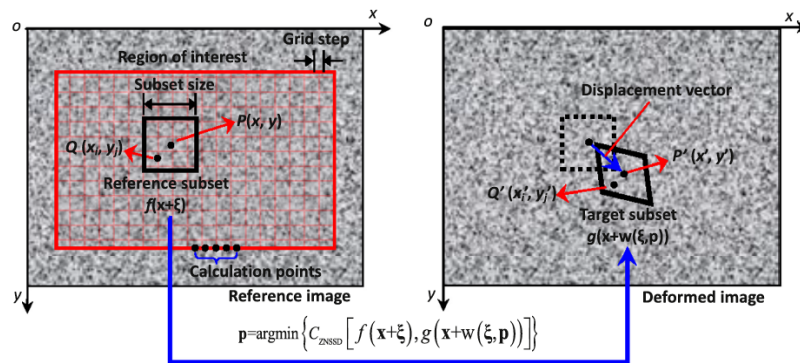


Figure 1.14: Basic principle of subset - based on DIC method [16]

1.4.3. Correlation Criterion

CC Criteria: CC stands for Cross-Correlation. Cross-correlation is a measure of similarity between two signals or datasets. In the context of image analysis or signal processing, cross-correlation is often used to compare two images or signals and quantify their similarity. The cross-correlation coefficient, also known as the correlation coefficient (CC), is a numerical value that ranges from -1 to 1. A value of 1 indicates a perfect match, 0 indicates no correlation, and -1 indicates a perfect negative correlation.

SSD Correlation Criteria: SSD stands for Sum of Squared Differences. In the context of image analysis, the Sum of Squared Differences is a method to measure the similarity or dissimilarity between two images. It involves calculating the squared difference between corresponding pixel values in the two images and summing them up. A lower value of SSD indicates a higher similarity between the images. So, in summary, CC criteria (such as correlation coefficient) focus on measuring the correlation or similarity between reference and deformed subsets, while SSD correlation criteria (like Sum of Squared Differences) quantify the dissimilarity between two subsets based on pixel-level differences. (Figure 1.15) [16]

Performance	CC criteria	SSD criteria
Sensitive to all changes of the deformed subset intensity	$C_{CC} = \sum f_i g_i$	$C_{SSD} = \sum (f_i - g_i)^2$
Insensitive to offset changes of the deformed subset intensity	$C_{ZCC} = \sum (\bar{f}_i \bar{g}_i)$	$C_{ZSSD} = \sum [\bar{f}_i - \bar{g}_i]^2$
Insensitive to scale changes of the deformed subset intensity	$C_{NCC} = \frac{\sum f_i g_i}{\sqrt{\sum f_i^2} \sqrt{\sum g_i^2}}$	$C_{NSSD} = \sum \left(\frac{f_i}{\sqrt{\sum f_i^2}} - \frac{g_i}{\sqrt{\sum g_i^2}} \right)^2$
Insensitive to the scale and offset changes of the deformed subset intensity	$C_{ZNCC} = \frac{\sum \bar{f}_i \bar{g}_i}{\sqrt{\sum \bar{f}_i^2} \sqrt{\sum \bar{g}_i^2}}$	$C_{ZNSSD} = \sum \left(\frac{\bar{f}_i}{\sqrt{\sum \bar{f}_i^2}} - \frac{\bar{g}_i}{\sqrt{\sum \bar{g}_i^2}} \right)^2$ $= 2(1 - C_{ZNCC})$

Figure 1.15: Types of correlation criteria used in DIC [14]

1.4.4. Stereovision and 3D-DIC

Binocular stereovision is a technique used to extract the 3D structure of a scene by capturing it from two different viewpoints. In this technique, two cameras are used, each capturing an image of the scene. In Figure 1.16 $P(X, Y, Z)$ is the 3-D point to be measured; $p1(u1, v1)$ and $p2(u2, v2)$ are its stereo projections in the images; $C1$ and $C2$ are the optical centers of the two cameras. [12]

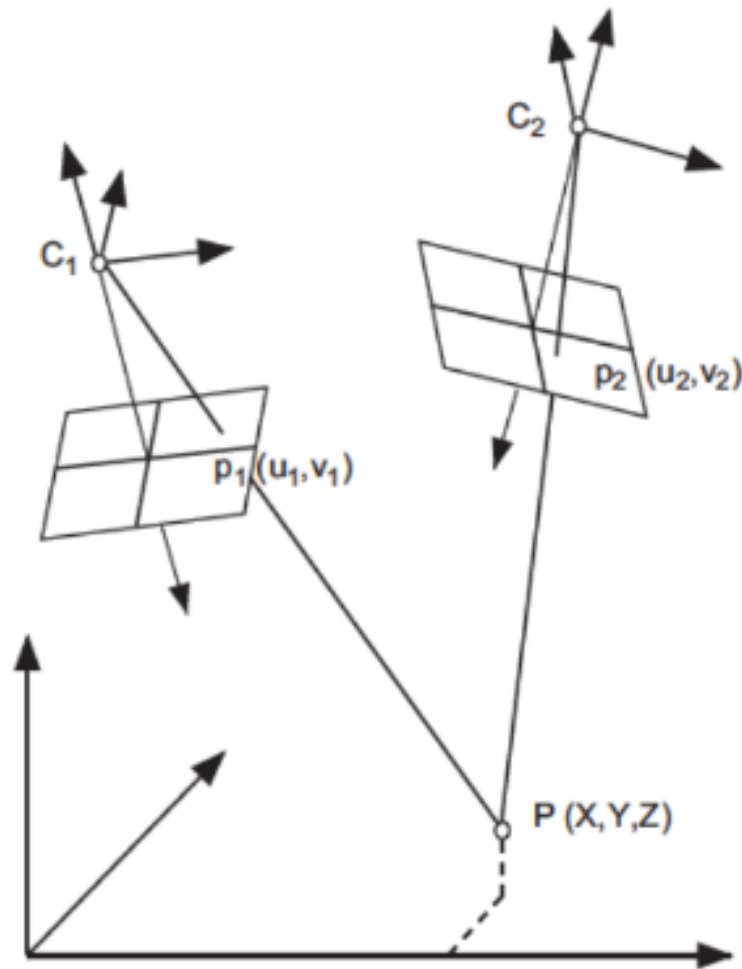


Figure 1.16: Binocular Stereovision [12]

To compute the 3D coordinates of a point using binocular stereovision, certain assumptions are made:

1. The geometry of the stereo rig, which refers to the relative position and orientation of the two cameras, is known. This information is obtained through an offline camera calibration procedure, where the intrinsic and extrinsic parameters of each camera are determined.
2. The image points p_1 and p_2 , corresponding to the same physical point P , are matched. This process is known as stereo matching, and it involves identifying the corresponding image points in the two images. Stereo matching algorithms are used to establish the correspondence between image points based on their similarity or disparity.

By knowing the geometry of the stereo rig and establishing the correspondence between image points, triangulation can be performed to compute the 3D coordinates of the physical point P . Triangulation involves calculating the intersection of rays projected from each camera's optical center to the corresponding image points. In a binocular stereo-vision system, when a point p_1 in image 1 is matched with its corresponding point p_2 in image 2, it is observed that it lies along a specific line in image 2. This line is entirely determined by the coordinates of p_1 , the relative position and orientation of the cameras, and their intrinsic parameters. This line is called the epipolar line associated with p_1 (Figure 1.17). [12]

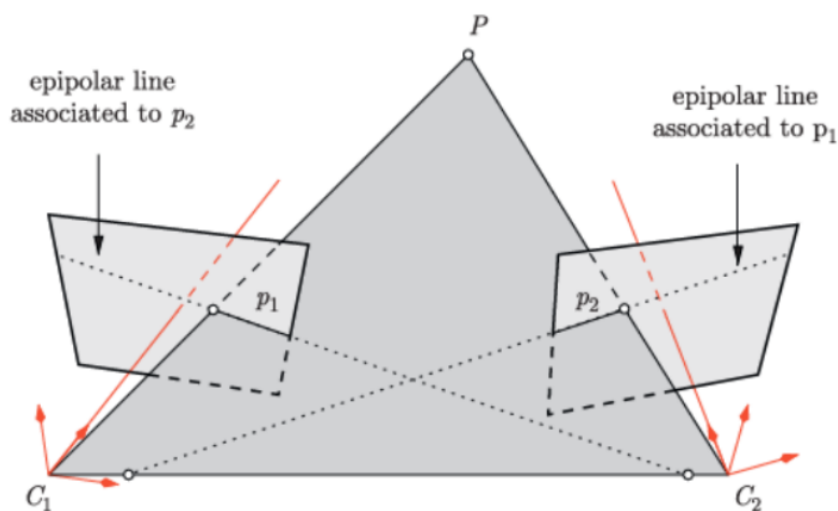


Figure 1.17: Epipolar plane [12]

The camera optical centers C_1 and C_2 , the 3-D point P and its images p_1 and p_2 lie in common plane. This plane intersects each image plane in an epipolar line. This geometric constraint, known as the epipolar constraint, is a fundamental property of any stereo imaging system. It simplifies the search for stereo-correspondence from a 2D search across the entire image to a 1D search along the epipolar line. This significantly reduces the computational complexity of finding corresponding points in the stereo images. In the case where the cameras are perfectly aligned, the epipolar lines are parallel to the rows of the images (Figure 1.18.)

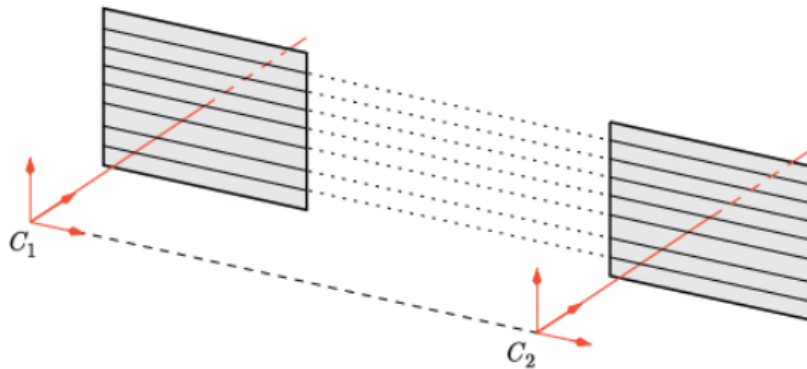


Figure 1.18: Epipolar line [12]

A rectified stereovision sensor: the epipolar lines are parallel to the image rows. This ideal configuration further simplifies the search for correspondences because the corresponding pixels lie on the same row in both images. In this configuration, the difference between the column coordinates of the matched points is referred to as "disparity," which represents the apparent horizontal shift between the points.

However, in practice, achieving perfect alignment of the cameras is challenging. To address this issue, a rectification procedure is performed at the processing level. This procedure involves applying a transformation, known as a plane-to-plane homography, to each image of the initial stereo pair. This transformation generates a new pair of stereo images that correspond to a virtual stereo rig with perfectly aligned cameras. The rectification procedure utilizes the calibration parameters obtained during the offline camera calibration phase. It should be noted that the rectification process also corrects for optical lens distortion, transforming the real distorted images into ideal distortion-free images.

The result of the rectification procedure is a pair of images that correspond to an ideal stereo rig with distortion-free and perfectly aligned cameras. This greatly simplifies the stereo-matching phase as the epipolar lines are now aligned with the rows of the rectified images. Importantly, it should be noted that the rectified or undistorted images themselves are not computed during the process. Instead, the computed rectification homographies and distortion parameters are directly used in the expression of the correlation function to operate on the raw images.

This approach allows for achieving high matching accuracy by avoiding pixel interpolations that are involved in distortion correction and image rectification. By directly using the raw images with the applied transformation parameters, the highest level of matching accuracy can be achieved in stereo-correspondence estimation.

The difficulty in stereovision lies in establishing correspondences between pairs of images.

Over the years, various algorithms have been proposed to tackle this challenge, and they can be broadly classified into two categories:

1. **Feature Matching:** Feature matching algorithms involve extracting distinctive primitives from the images. These features are then matched between the views being considered to establish correspondences. Feature matching methods are generally fast since they operate on a subset of image pixels, but they may yield sparse disparity maps with limited matches.
2. **Template Matching:** Template matching algorithms aim to correlate the gray levels of image patches between the views being considered. The assumption is that similar patterns or textures in the images will exhibit a high degree of similarity in their pixel intensities. Template matching methods can potentially provide dense disparity maps. However, they are more effective for relatively textured areas and image pairs with small differences.

In experimental mechanics, the focus is often on the surface strain field, which can be obtained by tracking the displacement of specific points on the surface of an object subjected to mechanical or thermal loads. Stereovision techniques enable the measurement of the 3D displacement field of an object undergoing 3D deformation. Using a pair of stereo images acquired at time t_0 , it is possible to calculate the shape of the object at that time. The same can be done using a pair of stereo images acquired at time t_1 . By matching the corresponding points between the images taken at times t_0 and t_1 (temporal matching or tracking), the 3D displacement of each image point can be computed.

When measuring 3D displacement fields using 3D DIC (Digital Image Correlation), a combination of stereo-correlation (stereovision + correlation-based stereo matching) and pixel tracking by correlation (DIC) is employed in the sequence of stereo images. This approach provides 3D information and allows for the tracking of pixel displacements. In order to achieve higher accuracy, an improved method has been proposed that combines temporal tracking and stereo-correlation. This method operates simultaneously on both pairs of stereo images, resulting in enhanced precision and reliability. By utilizing stereovision techniques and incorporating the benefits of temporal matching and stereo-correlation, it becomes possible to measure and analyze the 3D displacement field of objects undergoing deformation, providing valuable insights into their mechanical behavior. [12]

2 | Materials and Methods

After a detailed examination of the relevant thematic area, we move on to the next phase focusing on the review of tools used for experimental analyses. The general exposition on how the tools work for conducting research with DIC instrumentation has been partially discussed in previous chapters. We will focus on a concise recapitulation of the necessary tools before moving on to describe those used in the experiments of this thesis. The DIC machinery used during the research is housed at the Department of Mechanics and Aerospace (DIMEAS). The following image provides a schematic view of the experimental setup. (Figure 2.1)

Schematic Overview:

(Images / components may differ depending on configuration)

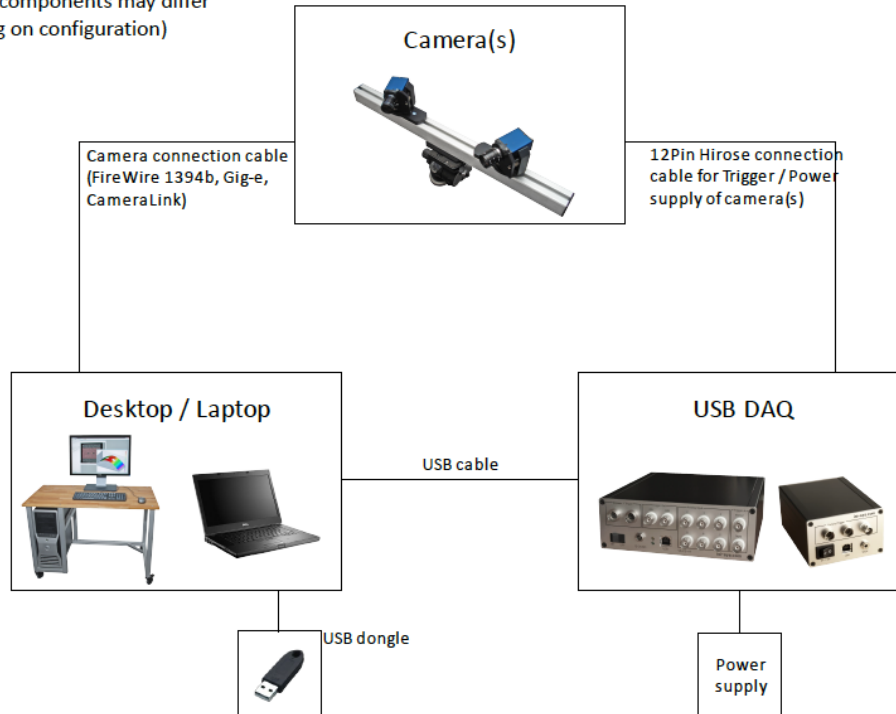


Figure 2.1: DIC overview (from isi-sys DIC Setup Guide)

2.1. Equipment

2.1.1. Cameras

The DIC setup is composed of two Basler ace ac4096-30um cameras (Figure 2.2).

The size of the optical sensor can be obtained from the technical specifications provided by the manufacturer or calculated by knowing the sensor's resolution and the size of a single pixel. In the case of the Basler ace acA4096-30um, the sensor's resolution is 4096×2168 pixels, and the size of a pixel is $3.45 \times 3.45 \mu\text{m}$. By multiplying the resolution by the size of a single pixel, the sensor size is obtained as $14.1 \times 7.5 \text{ mm}$. (<https://www.baslerweb.com>)



Figure 2.2: Basler ace ac4096-30um camera

The characteristics of its sensor are collected in the tables 2.3 and 2.4.

Sensor	
Sensor Vendor	Sony
Sensor	IMX267
Shutter	Global Shutter
Sensor Format	1"
Sensor Type	CMOS
Sensor Size	14.1 mm x 7.5 mm
Resolution (HxV)	4096 px x 2168 px
Resolution	9 MP
Pixel Size (H x V)	3.45 μm x 3.45 μm
Frame Rate	32 fps
Mono/Color	Mono

Figure 2.3: Sensor Characteristics

Camera Data	
Interface	USB 3.0
Pixel Bit Depth	10 or 12 bits
Synchronization	<ul style="list-style-type: none"> ▪ software trigger ▪ free-run ▪ hardware trigger
Exposure Control	<ul style="list-style-type: none"> ▪ hardware trigger ▪ programmable via the camera API
Digital Input	1
Digital Output	1
General Purpose I/O	2
Power Supply	<ul style="list-style-type: none"> ▪ Via USB 3.0 interface
Power Requirements (typical)	3 W

Figure 2.4: Camera Characteristics

The cameras have two image acquisition modes: standard and long exposure.

1. Standar mode: This is the default camera operation mode. It is suitable for most operating conditions, that is, when parameters are not set to extreme values.
2. Long Exposure mode: is useful when capturing images with long exposure times to optimize image quality.

To maximize the effect of this feature, it is recommended to provide heat dissipation, increase the exposure time, and minimize the frame rate as much as possible. If the

application permits, it is advisable to operate the camera in single shot mode and acquire only the images you need.

Hardware Triggering (Figure 2.5) is a triggering method that uses a pulse signal, just like the Digital Pulse Capture feature, but instead by-passes the need for the data acquisition device and connects directly from the signal generator to the cameras. (<https://www.baslerweb.com>)

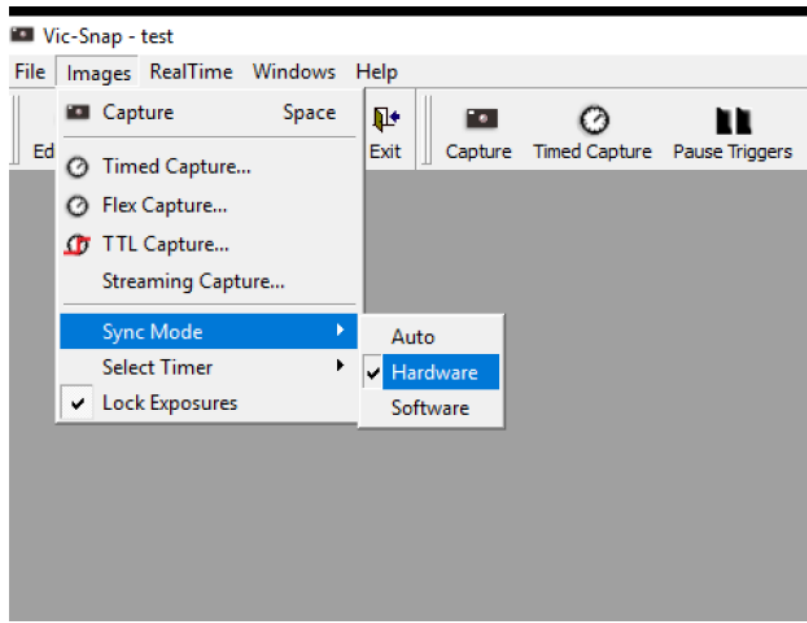


Figure 2.5: Hardware triggering (from Application Note AN-1703 Triggering Methods)

To correctly connect the Basler ace acA4096-30um camera to the equipment or experimental tools used, a C-Mount adapter will be required. The choice of adapter depends on the compatibility between the camera, the equipment, and the object of study. It is important to consider the size of the object you want to observe, the sensor size of the camera, and the type of available equipment.

2.1.2. Lens selection and extension tubes

It's crucial to emphasize that both the object's size, the sensor's scale, and the type of adapter are all variables subject to limitations, stemming from the conditions of the available equipment and the characteristics of the sample we are analyzing. Similarly, there are restrictions in the choice of lens; despite the software having a wide selection of lenses, we will only have a few that are actually usable in our set. Specifically, we are limited to using two Rodagon 80 mm lenses and two Rodagon 135 mm lenses, compatible with our DIC - Correlate Solution equipment. The only element where we have some flexibility is

the distance between the front portion of the lens and the sample (Free Working Distance, FWD). We enter all the parameters into the Mach Vis software, choosing a 400 mm analysis field. Subsequently, the software provides the configuration and physical positioning of our DIC device in relation to the sample we are examining.

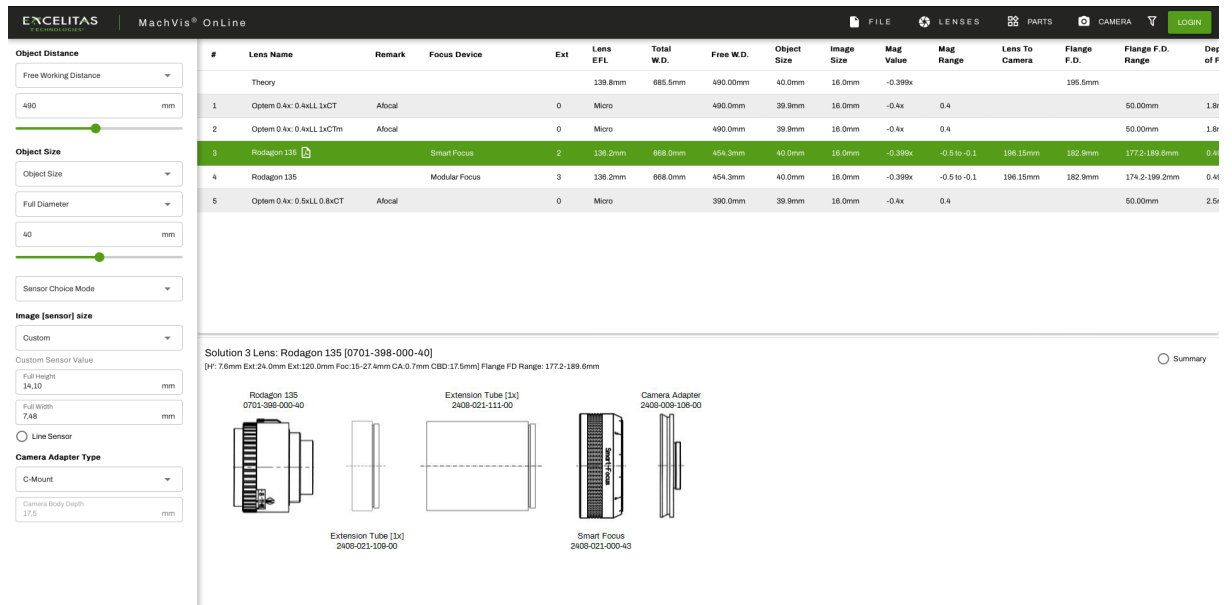


Figure 2.6: Selection of lenses to be used through the Mach Vis software.

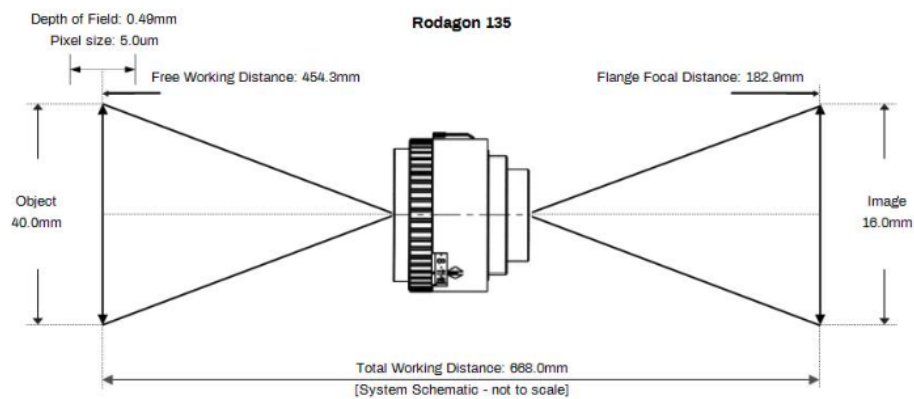


Figure 2.7: Optical parameters of the Rodagon 135 mm lens

The software (Figure 2.6) has provided us with a configuration for using the Rodagon 135 mm lenses (Figure 2.7) with two extension tubes: 120 mm and 24 mm. We proceed with the assembly of the cameras, Smart Focus and extension tubes as shown in Figure 2.8.

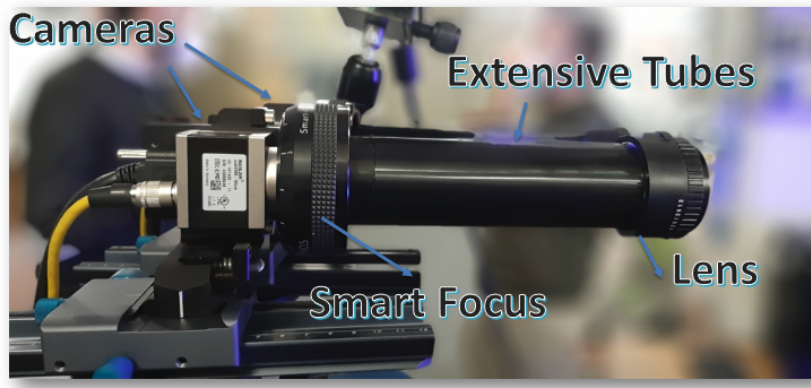


Figure 2.8: Assembly of lenses, cameras and extensive tubes

2.1.3. DAQ Unit

The DAQ (Data Acquisition) devices (Figure 2.9) are configured to work with the Vic software for Digital Image Correlation (DIC) provided by Correlated Solutions. These devices are an essential component of DIC systems, serving the purpose of triggering the cameras using a hardware trigger and simultaneously recording analog data. There are three types of DAQ devices available, each offering different performance and features. For this specific experiment, the DAQ-STD-8D Synchronization was utilized (Figure 2.10). This device acts as a trigger mechanism, facilitating the operation of the High-Speed module and providing power to the cameras. The hardware trigger is transmitted through the 12-pin Hirose connectors located on the DAQ unit. Two of these connectors are available, allowing for the connection of up to two cameras.



Figure 2.9: Control elements front layout of DAQ unit

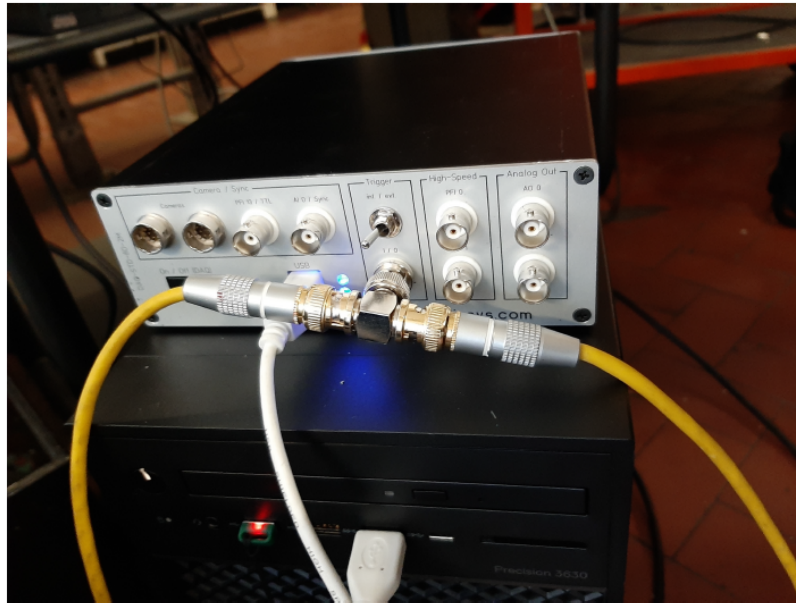


Figure 2.10: DAQ-STD-8D

The standard hardware trigger mode in Vic-Snap can be employed with the Transistor-Transistor Logic (TTL) Capture method. This configuration enables the cameras to be triggered using standard hardware triggering. The hardware trigger mode can be selected within the Vic-Snap software. In our setup, there is no requirement to connect any TTL signal to the PFI 13/Light connector. In the context of cameras, a TTL trigger can be utilized to initiate the capture of an image or to synchronize the capture of images across multiple cameras. The "trigger" refers to the event that initiates this action. (Figure 2.11)

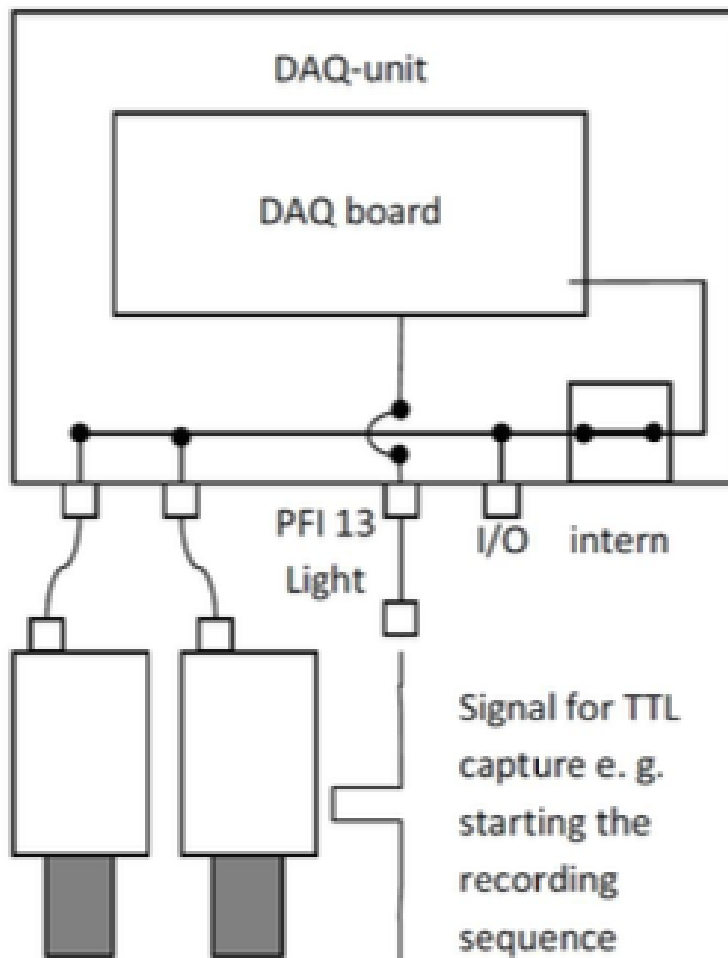


Figure 2.11: Schematic DAQ Operation (from isi-sys DAQ-unit)

2.1.4. Light Source

Light is a crucial and significant element in ensuring the accuracy of the acquisition system. Therefore, the use of a blue light source is chosen to improve the lighting conditions of the sample. [14]

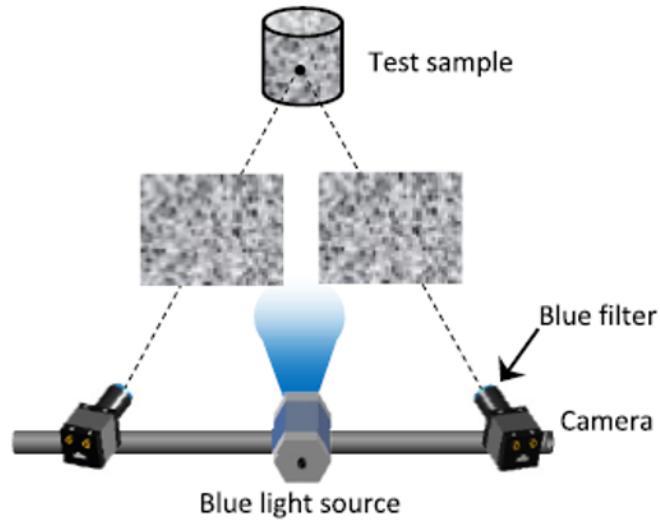


Figure 2.12: Schematic view of sample image acquisition through 3D-DIC [14]

The illumination of the specimen plays a fundamental role in achieving optimal results, as it provides the following advantages: It allows for the unique identification of the pattern. It enables the tracking of the speckle during the test. Various light sources can be used, such as halogen light, white LED, or monochromatic LED. It is essential that the lighting is as uniform and intense as possible. Intensity is necessary to adequately illuminate the pattern on the object, thereby avoiding the formation of areas of uncertainty. Uniformity, on the other hand, is important to prevent reflections that could cause differences in lighting between the two cameras or areas where the pattern is not clearly visible. [13]

How can be observed in the Figure 2.13, that light is a significant factor in the accuracy of the machinery, as it reduces noise levels and also minimizes systematic errors. [7]

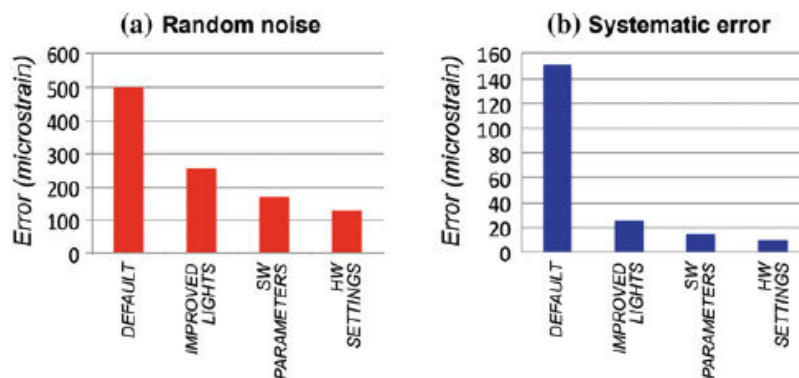


Figure 2.13: Improvements in terms of accuracy and precision of DIC [7]

2.2. Software

The software that will be used for image processing is VIC 3D in its version 9.4. How it can be observed in the Figure 2.14, the user interface is simple. The windows, such as the AOI Editor and tracking windows, are grouped within a Workspace. The list view on the left side of the main window provides a quick overview of image and data files.[20]

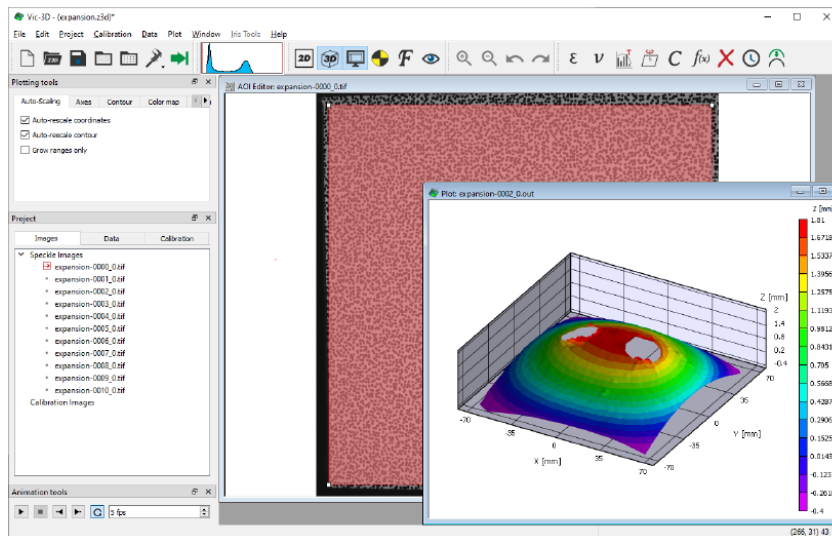


Figure 2.14: Vic-3D Application Window [20]

It is initialized by creating a project as illustrated in the following figure.

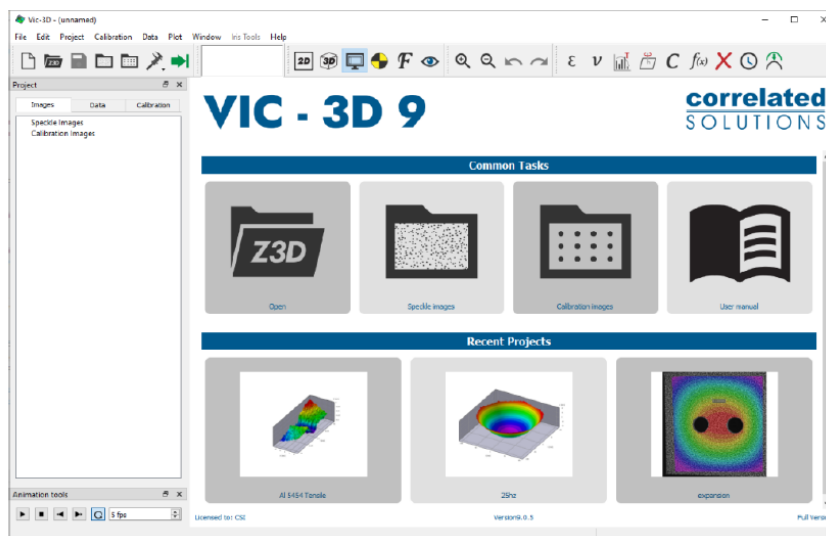


Figure 2.15: Vic-3D start page [20]

To add calibration images, you need to select *Immagini* (Images), then click on *Immagini*

di calibrazione (Calibration images) from the menu bar, or click on the icon for calibration images on the main toolbar (Figure 2.16).



Figure 2.16: The main toolbar [20]

There are two important panels to consider during the processing: the panel for captured images and the panel for the calibration process.

The data panel for captures images shows the output data generated by Vic-3D as well as any analog data acquired with Vic-Snap. The file names of the output files generated by Vic-3D correspond directly to the image file names and differ only in the extension.(Figure 2.17)

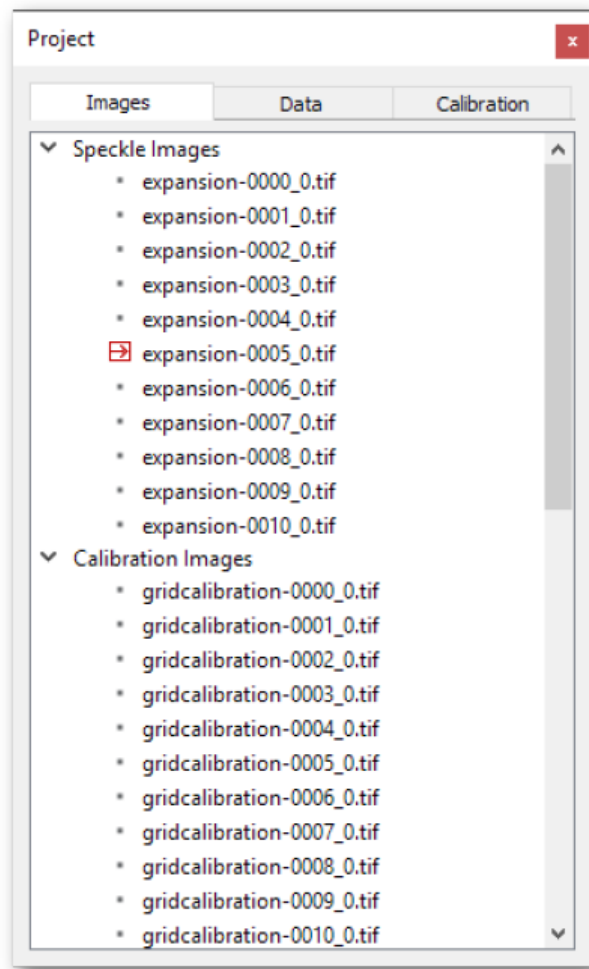


Figure 2.17: Data Panel [20]

The calibration panel displays shows the current calibration information for the project. The calibration panel does not permit editing the calibration values and merely displays the results of the calibration process calibration process.(Figure 2.18)

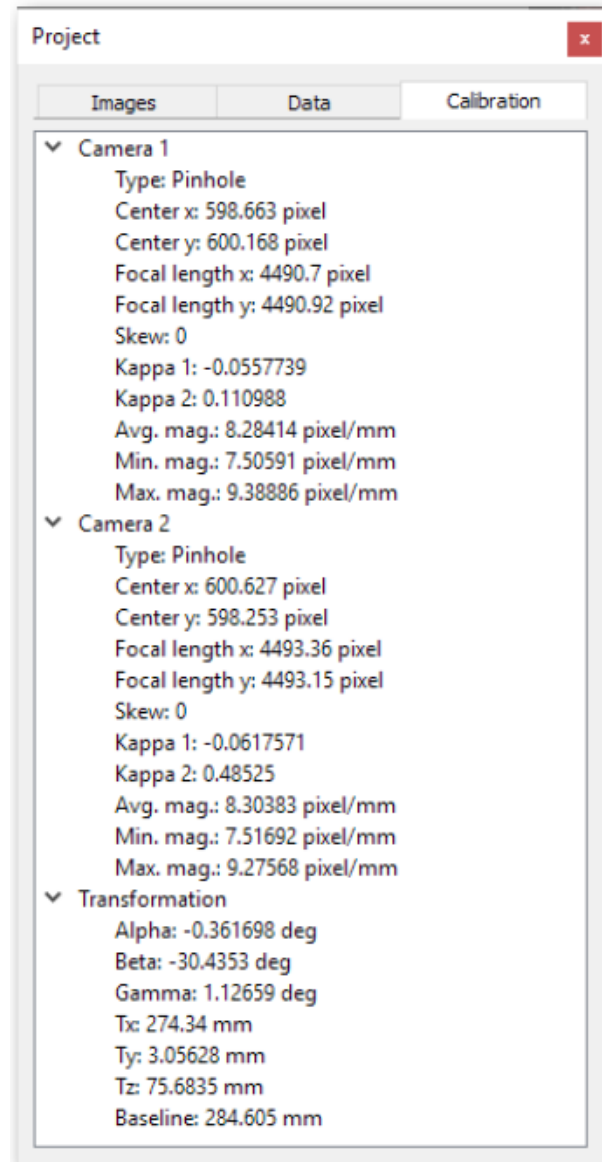


Figure 2.18: Calibration Panel [20]

Intrinsic camera parameters are displayed for each camera:

1. sensor center
2. focal length (in pixels)
3. estimated magnification

4. rotation angles alpha, beta (stereo angle) and gamma
5. translation components Tx, Ty and Tz between the cameras
6. baseline: distance between cameras (resultant of Tx, Ty, Tz) [20]

In the following Figures 2.19, 2.20, 2.21 are presented a wide range of output data obtained during correlation and optional post-processing.

Always Present

- X [mm] – metric position along the X-axis (by default, the horizontal axis).
- Y [mm] – metric position along the Y-axis (by default, the vertical axis).
- Z [mm] – metric position along the Z-axis (by default, the out-of-plane axis).
- Sigma [pixel] – the 1-standard deviation confidence in the match, in pixels. 0 indicates a perfect match; higher numbers indicate a noise, excessive gradients, or possibly a failed match.
- U [mm] – metric *displacement* along the X-axis, from the reference image. For the reference image, this value will always be 0.
- V [mm] – metric displacement along the Y-axis.
- W [mm] – metric displacement along the Z-axis.
- x [pixel] – the X location, in the raw image, of the data point,
- y [pixel] – the Y location, in the raw image, of the data point.
- u [pixel] – the raw X-axis displacement between the reference image and a given image, in pixels. This is an internal variable which feeds into the triangulation algorithm to generate the 3D metric **displacement** data. Effectively, this variable is the output of a 2D correlation between the reference camera 0 image and the deformed camera 0 image.
- v [pixel] – the raw Y-axis displacement between the reference image and a given image, in pixels.
- q [pixel] – the raw X-axis disparity between the camera 0 image and camera 1 image, in pixels. This is an internal variable which feeds into the triangulation algorithm to generate the 3D metric **shape** data. Effectively, this variable is the output of a 2D correlation between the reference camera 0 image and a given camera 1 image.
- r [pixel] – the raw Y-axis disparity between the camera 0 image and camera 1 image, in pixels.
- q_ref [pixel]– this is the same as the computed X-axis disparity but is reserved for the software and cannot be edited by the user. This variable is used for retriangulation.
- r_ref [pixel]– the reserved Y-axis disparity.

Figure 2.19: Always present output [6]

Strain Variables

- ϵ_{xx} [1] – strain in the X-direction. Positive numbers indicate tension; negative numbers indicate compression.
- ϵ_{yy} [1] – strain in the Y-direction.
- ϵ_{xy} [1] – shear strain.
- ϵ_1 [1] – the major principal strain.
- ϵ_2 [1] – the minor principal strain.
- γ [1] – the principal strain angle, measure counterclockwise from the positive X-axis.

Velocity Variables

- dU/dt [1] – the rate of change of the U-displacement; that is, the velocity of a given point in the X direction.
- dV/dt [1] – velocity in the Y direction.
- dW/dt [1] – velocity in the Z direction.
- $d\epsilon_{xx}/dt$ [1] – the rate of change of strain in X, or *strain rate* in X.
- $d\epsilon_{yy}/dt$ [1] – the strain rate in Y.
- $d\epsilon_{xy}/dt$ [1] – the shear strain rate.
- Note: principal strain rates are not calculated because principal strains, by nature, do not have a consistent reference frame from one image to the next.

Confidence Margins

- σ_X [mm]– the 1-standard-deviation (67%) uncertainty in the X-axis.
- σ_Y [mm]–the 1-standard-deviation (67%) uncertainty in the Y-axis.
- σ_Z [mm]–the 1-standard-deviation (67%) uncertainty in the Z-axis.

2D-Specific Variables

- x_c, y_c, u_c, v_c - these variables appear in the extraction dialog. If a scale calibration is present, they represent the scaled position and displacement. If no scale calibration is present, they're equal to the pixel values.

Figure 2.20: Strain variables, velocity variables, confidence margin and 2D specific variables [6]

Deformed Variables (export only)

- X_p – the deformed X value, equal to $X+U$. This is an option in the export dialog and is added for convenience.
- Y_p – the deformed Y value, equal to $Y+V$.
- Z_p – the deformed Z value, equal to $Z+W$.

Figure 2.21: Deformed variables [6]

2.3. Samples

During the experimentation, four samples are analyzed: a standard gear, a thin-rim gear, a non-shot-peened gear, and a shot-peened gear. At first analysis, two types of gears with different geometries were used: Standard Gear and Thin rim Gear. During a static bending test, these gears were subjected to four different loads:

- Load 1: 1920N
- Load 2: 3992N
- Load 3: 5980N
- Load 4: 7980N

Throughout the testing process, a DIC (Digital Image Correlation) machine captured images of the deformation process caused by the different loads. These gears are made of C45 steel, without a thermal treatments.

2.3.1. Standard Gear

The technical drawing of a standard gear is shown in Figure 2.22.

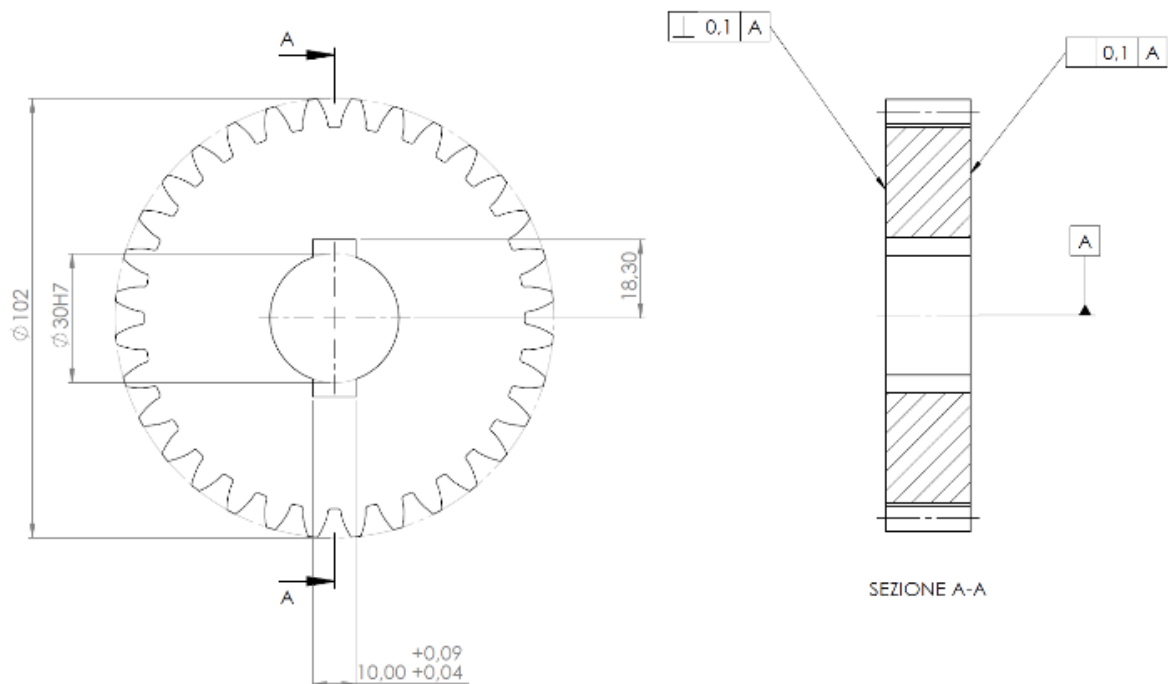


Figure 2.22: Technical drawings of standard gear [6]

In table 2.1 are presented the geometric values of the standard gear:

Table 2.1: Standard Gear Geometry

Pitch diameter (d_p)	96 mm
Face width (b)	20 mm
Number of teeth (Z)	32 mm
Modulus (m)	3 mm
Backup ratio (mb)	1
Web ratio (mw)	1
Gear blank factor	1

2.3.2. Thin-Rim Gear

The technical drawing of a thin rim gear is shown in Figure 2.23.

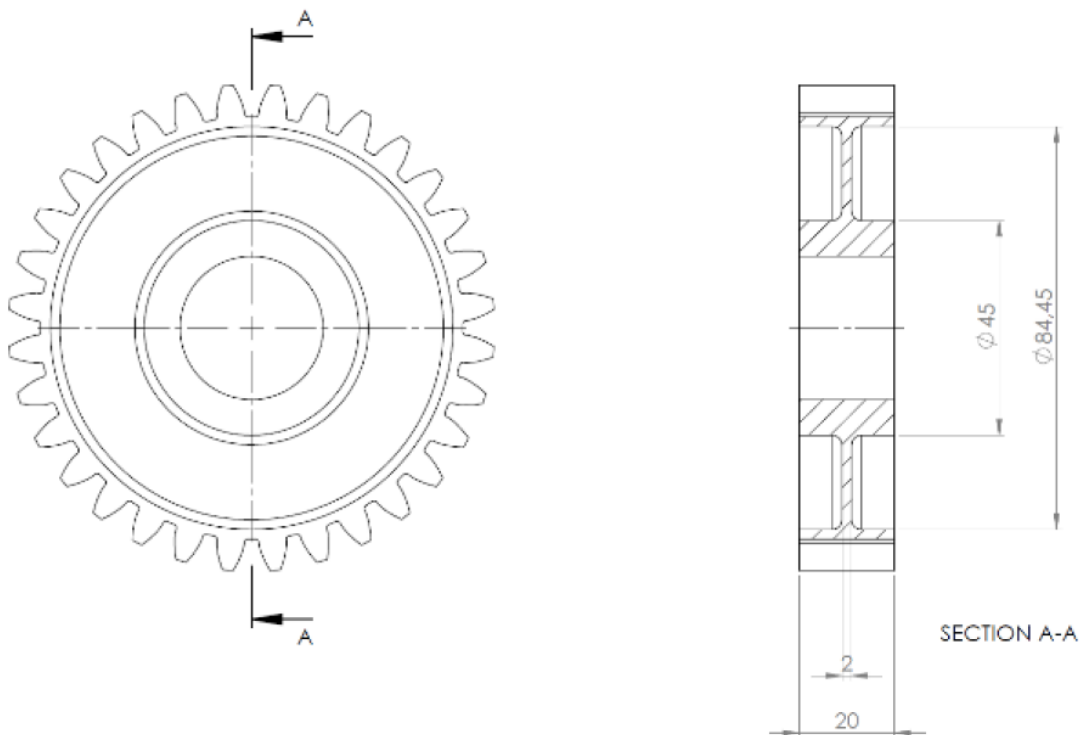


Figure 2.23: Technical drawings of thin-rim gear [6]

In table 2.2 are presented the geometric values of the thin-rim gear:

Table 2.2: Thin-rim Gear Geometry

Pitch diameter (dp)	96 mm
Face width (b)	20 mm
Number of teeth (Z)	32 mm
Modulus (m)	3 mm
Backup ratio (mb)	0,3
Web ratio (mw)	0,1
Gear blank factor	0,63

2.4. Experimentation Preparation

2.4.1. Sample Preparation with Speckle Technique

In digital image correlation, the quality of the data often depends on the quality of the speckle pattern. Having an optimal speckle pattern is crucial for reducing measurement noise and improving overall results. Understanding the requirements of an ideal speckle pattern and its proper application to a specimen is essential for using DIC effectively.

The purpose of speckle preparation is to ensure that the area to be analyzed is suitable for recognition by the cameras and subsequent analysis. This area should have a flat surface without roughness to avoid any issues during the analysis process. The entire surface of the sample should be thoroughly cleaned to remove any residual materials that could influence deformation results. The surface is then painted with a layer of white paint followed by a layer of black paint. The speckle pattern, which consists of the black paint, is created using an airbrush with a pressure of 2 Bar to achieve a uniform distribution of patterns. The choice of pressure and airbrush settings is determined through tests to obtain the desired pattern.

The speckle pattern should have specific characteristics, including a correct pixel size and a uniform distribution across the entire surface of the material or sample. It is important that the pattern remains fixed throughout the loading process, ensuring that the spatial distribution of patterns is maintained across the sample's surface.

The speckle distribution should ideally have a black percentage of 50-60%. This helps achieve better results during analysis and result validation, enhancing accuracy and distribution. Each point can be uniquely identified during the material deformation process.



Figure 2.24: Painted standard gear



Figure 2.25: Speckled standard gear



Figure 2.26: Painted thin-rim gear



Figure 2.27: Speckled thin-rim gear

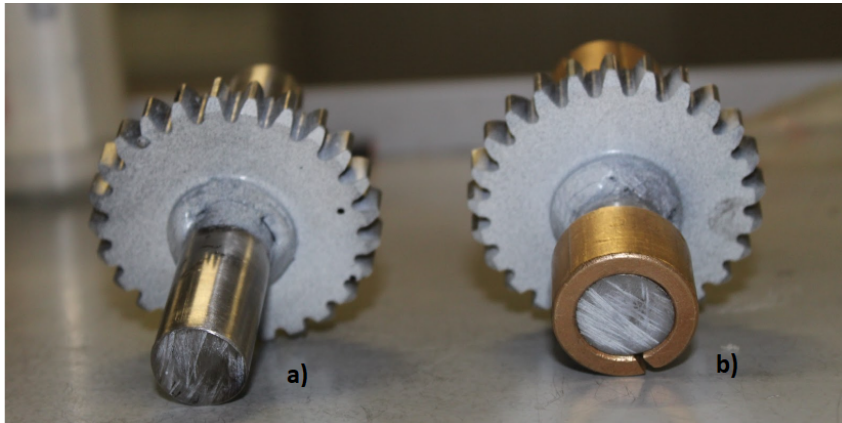


Figure 2.28: Speckled non-shot-peened gear (a) and speckled shot-peened gear (b)

To assess the quality of the pattern, particularly the speckle size and black-on-white contrast, a MATLAB code is used. This code determines the speckle size by identifying black areas on white areas, confirming the creation of an excellent and "clean" pattern for analysis. Specifically, a Matlab code allows for the identification of teeth with good speckle distribution, favorable light conditions, and appropriate size, making them suitable for analysis and providing more accurate results.

The following images and their corresponding data are extracted from the program that allows understanding the size of the speckle and, therefore, the quality of the pattern 2.29- 2.30; 2.31 - 2.32; 2.35 - 2.34; 2.35 - 2.36.

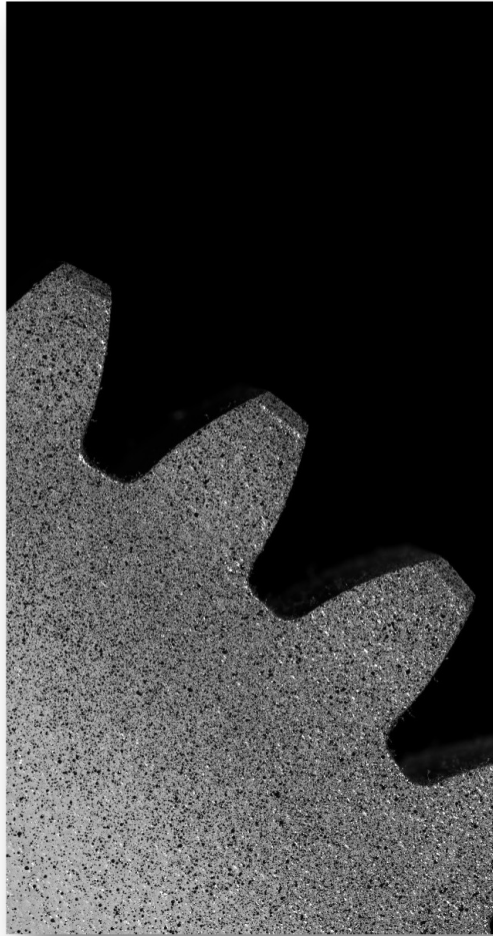


Figure 2.29: Photo of a speckled standard gear through DIC

```
thresholdValue = 0.3412
```

```
numTotale = 29766
```

```
bwRatio = 49.5432
```

Figure 2.30: Resulting data from Matlab analysis of speckled standard gear

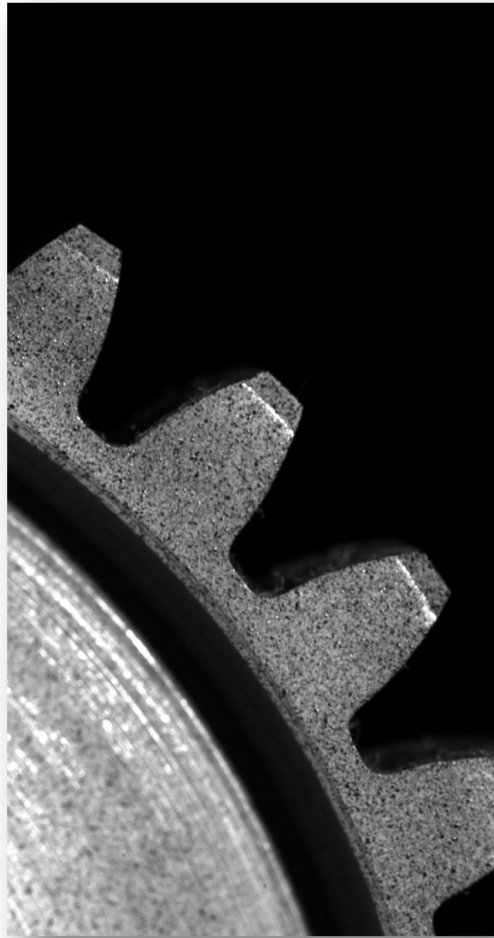


Figure 2.31: Photo of a speckled thin-rim gear through DIC

```
thresholdValue = 0.2353
```

```
numTotale = 685
```

```
bwRatio = 62.9751
```

Figure 2.32: Resulting data from Matlab analysis of speckled thin-rim gear

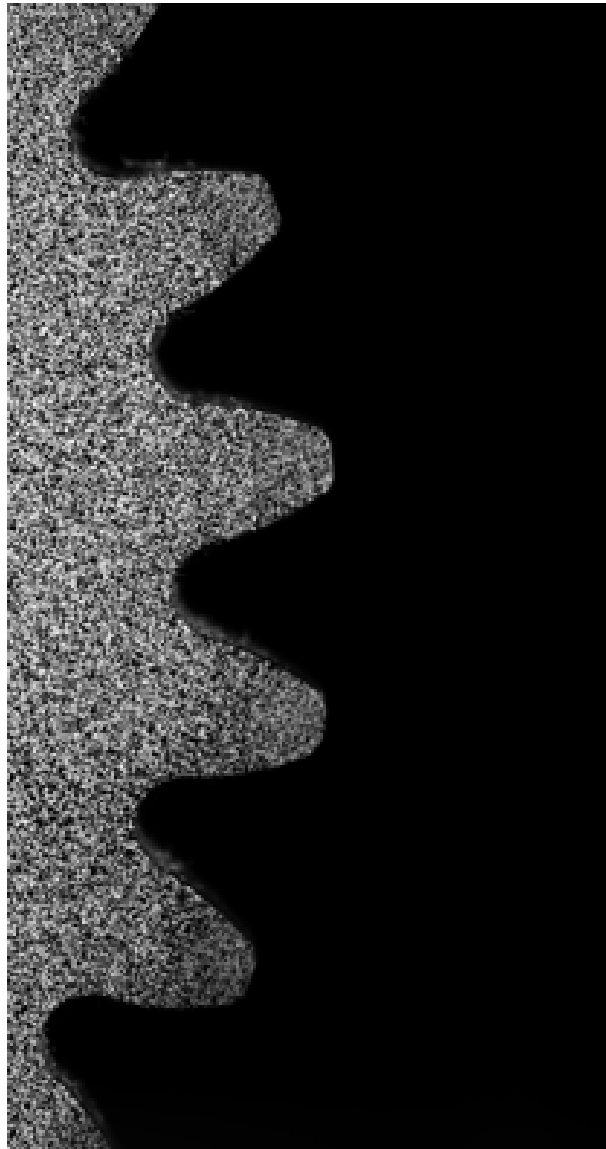


Figure 2.33: Photo of a speckled shot-peened gear through DIC

```
thresholdValue = 0.3608
```

```
numTotale = 21085
```

```
bwRatio = 71.2675
```

Figure 2.34: Resulting data from Matlab analysis of speckled shot-peened gear

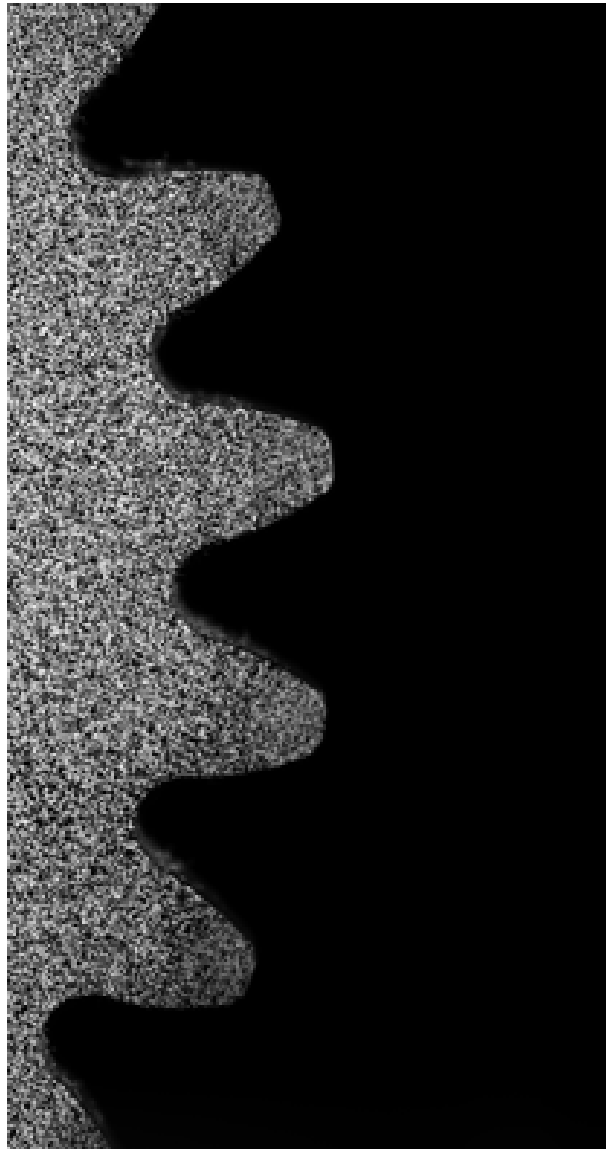


Figure 2.35: Photo of a speckled shot-peened gear through DIC

```
thresholdValue = 0.3529
```

```
numTotale = 15081
```

```
bwRatio = 77.9355
```

Figure 2.36: Resulting data from Matlab analysis of speckled non-shot-peened gear

2.4.2. Vertical Support and Punch

A crucial aspect of the experiment involves assembling a vertical support on which a gear will be mounted. This vertical support has been specifically modified and created for the purpose of conducting a bending test. The test involves applying stress to the gear placed on top of the support and connected to the ISTRON standard testing machine.

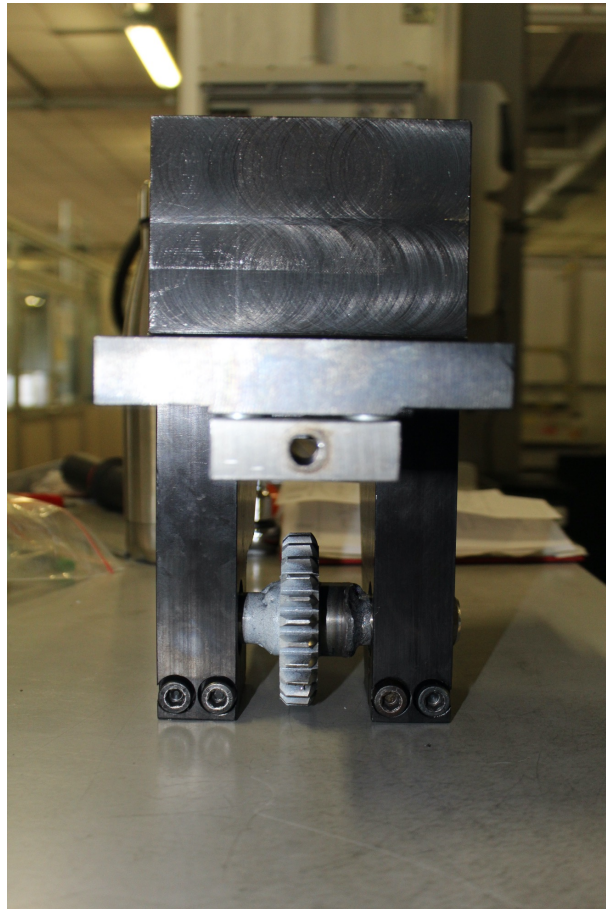


Figure 2.37: Side view of vertical support with mounted gear

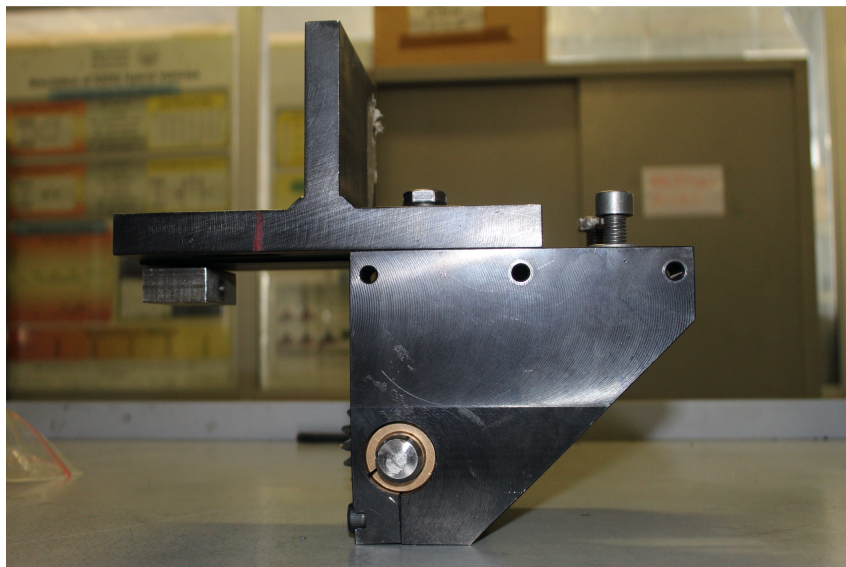


Figure 2.38: Front view of vertical support with mounted gear

This vertical support is a special device connected to a standard testing machine Instron. The device is designed to hold the gears in place while applying a controlled loading of bending stress. Gears, especially thin rim gears, are prone to bending stress due to the forces applied during operation.



Figure 2.39: Vertical support permanently mounted on the apex of the Instron machine

The device incorporates a specialized punch that is capable of applying multiple loadings to the gear tooth. The punch is designed to deliver these loadings along the tooth's invo-

lute profile, taking into consideration both the position and direction of the loading with respect to the single contact point between the gear tooth and its mating component.(ISO standards in [2], [3])

By applying loadings along the involute profile, the punch ensures that the gear tooth experiences a range of loading conditions that mimic the actual operating conditions it will encounter. This loading configuration allows for a comprehensive evaluation of the tooth's response to different load magnitudes, directions, and positions. The punch is precisely positioned to align with the gear tooth's involute profile, ensuring that the load is applied accurately and consistently throughout the testing process.



Figure 2.40: The punch that will apply different loads to Standard Gear during the bending test

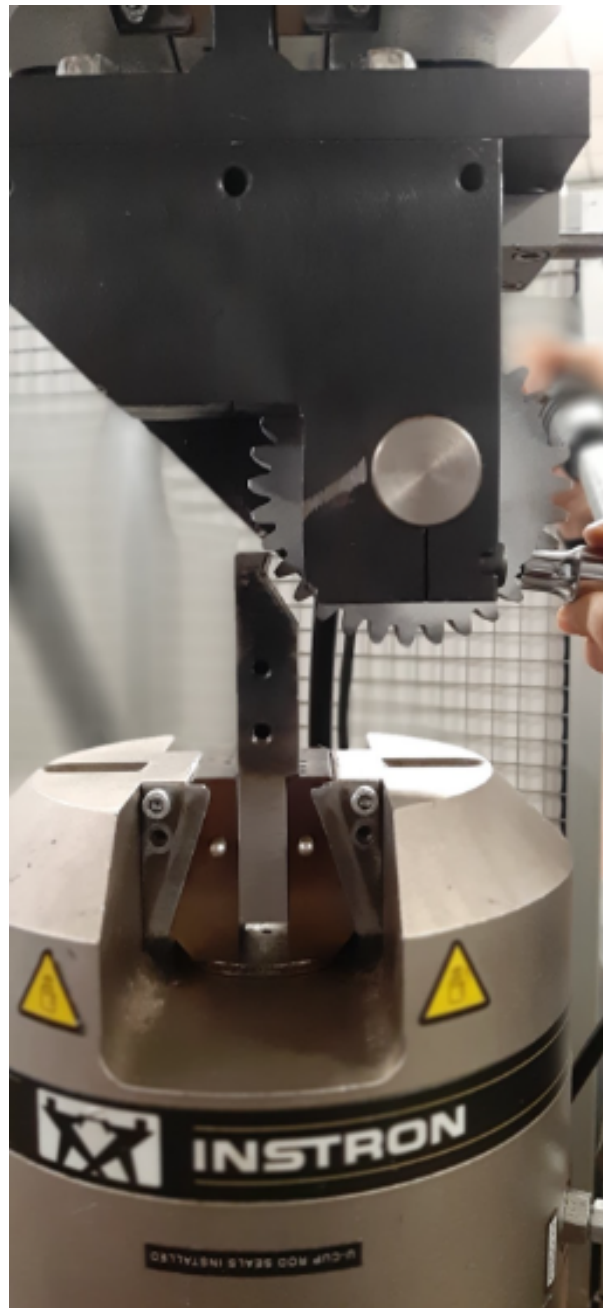


Figure 2.41: Contact moment between punch and gear

2.4.3. DIC Assembly

The assembly of the DIC instrumentation is carried out following the procedure outlined below:

- Connect the two cameras to a bar supported by a tripod.
- Add a blue light source for illuminating the sample.

- The choice of lenses depends on the size of the sample being examined. To determine the appropriate lenses, the sample is evaluated using the VIC Smat software. This evaluation helps determine the necessary lenses, camera positions, lens-to-sample distance, and depth of field.
- During the assembly, extension tubes can be added to improve visual space and spatial resolution.

Based on the collected data, the analysis of the standard gear and the lightweight gear utilizes 135 mm Rodagon lenses. Two extension tubes, one of 120 mm and another of 24 mm, are added. The DIC instrumentation is positioned at a distance of 49 cm from the sample, with a depth of field (f) of 11 Hz.

The two cameras are placed at a distance of 50 mm from each other, while there is a 25 mm distance between the lenses. The cameras are nearly parallel, allowing for analysis with a very small stereo angle of approximately 10 degrees. This parameter is significant as it demonstrates the validity of the experiment and ensures the accuracy of the results.

2.4.4. Sample Calibration

The calibration of the sample involves placing a target at a specific distance, determined by the software, to simulate the positioning of the sample during testing. By employing rotational or tilting movements, various points on the target can be framed, establishing a correlation between the target and the sample. The software converts the image into a digital signal and performs a perspective transformation, linking an external three-dimensional system to the reference system of the camera model originating from the lens's optical center.

As can be seen, the target has two different types of points: three black points with a white center, which are used by the software to evaluate the target's orientation, and a grid of points, which are actually used for calibration. It is not important for all the grid points to be contained within the image, but it is essential for the three points marked with a white center to always be within it. The reference length of the measurements is relative to the center of gravity between two points with a white center, as shown in the Figure 2.42.

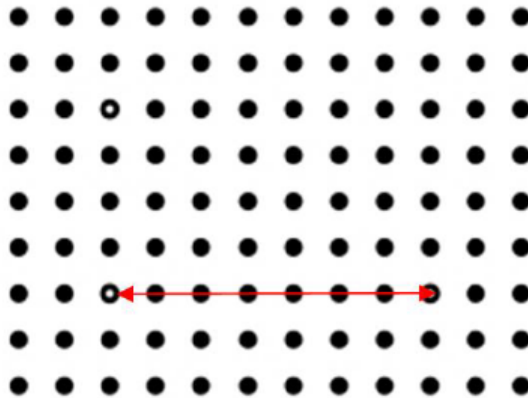


Figure 2.42: Reference length of the measurements

The size of the target should be chosen so that it fills the field of view as much as possible. For calibration, images of the target are acquired in different positions. Specifically, the target is slightly rotated around its three axes to acquire images showing it in different positions and orientations.

Once the images are acquired, with the help of the Vic-3D software, the detected points are extracted, and the system is calibrated. At the end of the process, a score is obtained, indicating the quality of the calibration achieved. Generally, a value between 0.03 and 0.05 pixels is acceptable (the lower the score, the better the calibration) (Figure 2.43).

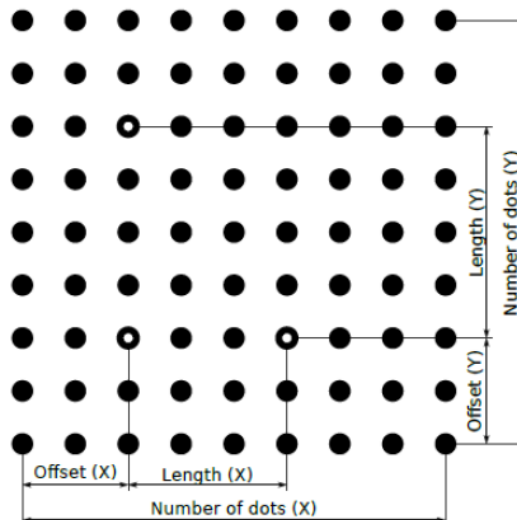
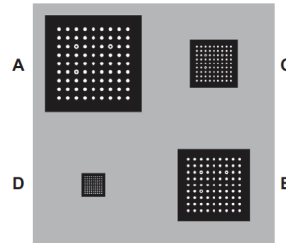


Figure 2.43: Main parameters of the target calibration

For this experiment, a 9x9 dot target with a diameter of 0.84 mm was utilized. A type C

glass target with a pitch of 0.890 mm was selected, enabling better visibility of the dots (Figures 2.44, 2.45). However, special care needs to be taken to maintain a clean surface to ensure the calibration results are not compromised.



Grid	Size (mm)	Pitch (mm)	Vic-3D settings for all grids:	
A	14.929	1.780	Number of dots in X	9
B	10.720	1.340	Number of dots in Y	9
C	7.120	0.890	Offset in X	3
D	3.600	0.450	Offset in Y	3
Tolerances +/- 0.002 mm			Length in X	3
			Length in Y	4

Figure 2.44: 4-in-1 Calibration Glass Target

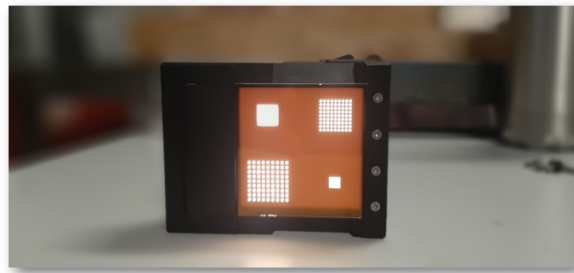
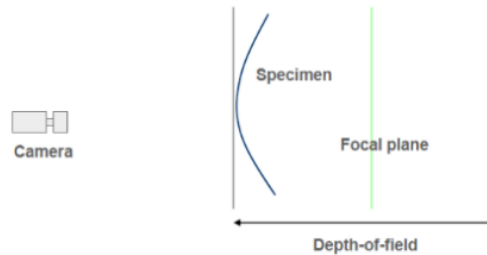


Figure 2.45: Glass target Used during experimentation

A recommended practice is to reduce the aperture of the lens, thereby limiting the exposure time, to prevent any movement of the target from being captured. In this particular case, the analysis was conducted with a very short exposure time to achieve an optimal depth of field (11 Hz) (Figure 2.46). During the calibration process, it is possible to adjust the exposure time to ensure that there are no reflections or glare on the calibration target. However, it is not possible to change the aperture of the lens, the focus, or the camera position during this stage. Once the calibration settings are finalized, image acquisition for the calibration process begins. There is no fixed number of images required for gear calibration, but 42 images are considered to yield satisfactory results for the calibration procedure. The quality of the acquired images depends on crucial parameters such as accurate focus, the absence of reflections, and good lighting conditions.

a) Small aperture (high f-number):



b) Large aperture (small f-number):

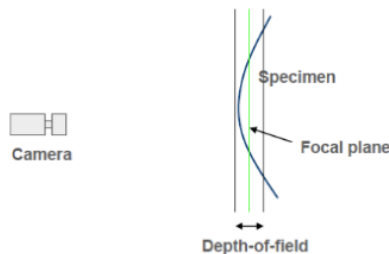


Figure 2.46: Representation of depth of field (f): a) If the lens aperture width is reduced, f has a high numerical value; b) If the lens aperture width is wider, f has a low numerical value. [1]

2.4.5. Brightness and Focus

As discussed earlier, lighting is an important parameter for the accuracy of the DIC machine. During the experiment, efforts were made to achieve optimal focus. Different settings of the lens, such as aperture and exposure time, were adjusted to find the optimal conditions for brightness and focus. In Figure 2.47, Figure 2.48, Figure 2.49, a close-up of the focus of the two cameras in various DIC analyses can be observed. Using the Vic Snap software, the color map representing an estimation of the expected noise is analyzed. As can be seen, the closer the color tends to purple, the lower the expected noise, indicating a better focus of the image.

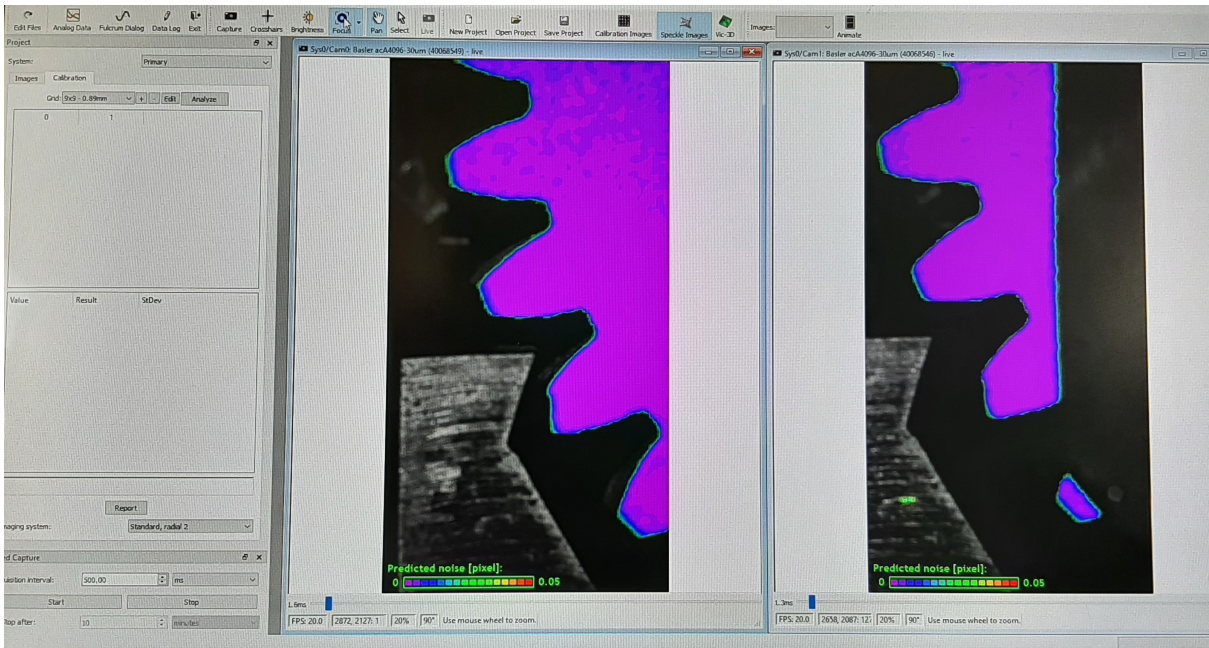


Figure 2.47: Brightness and Focus - Standard Gear

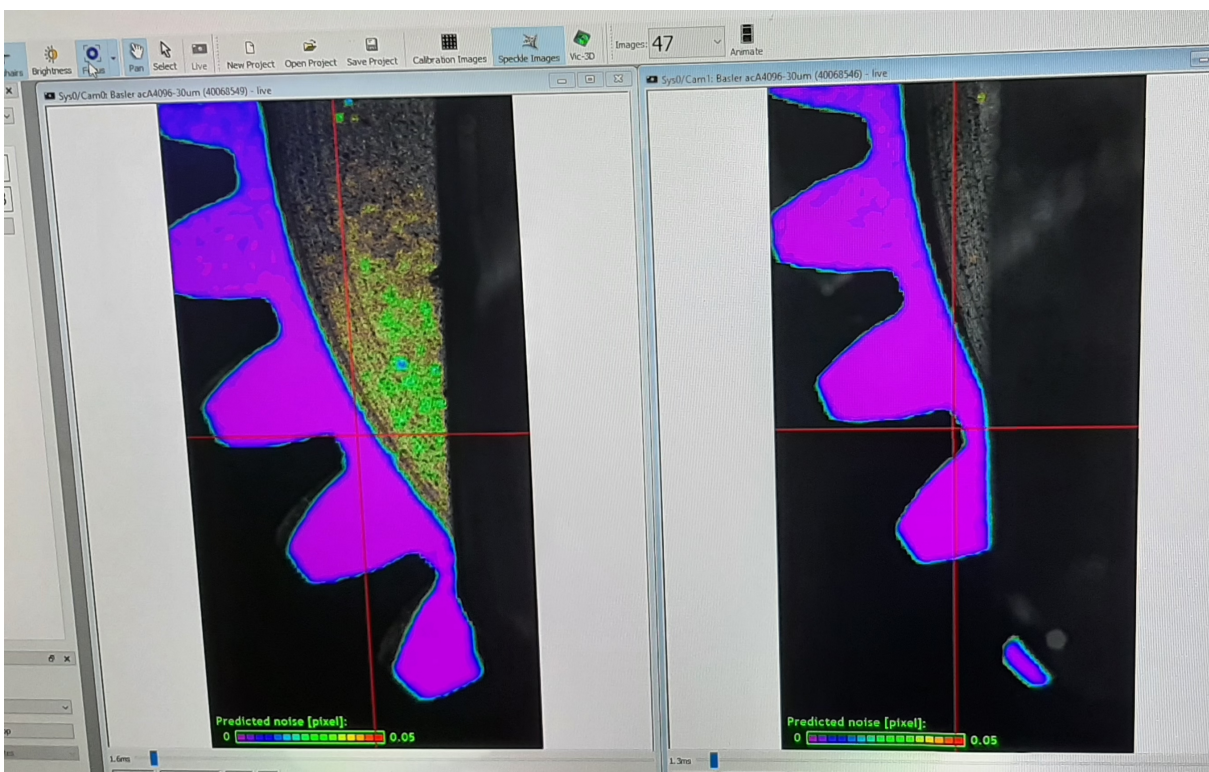


Figure 2.48: Brightness and Focus - Thin Rim Gear

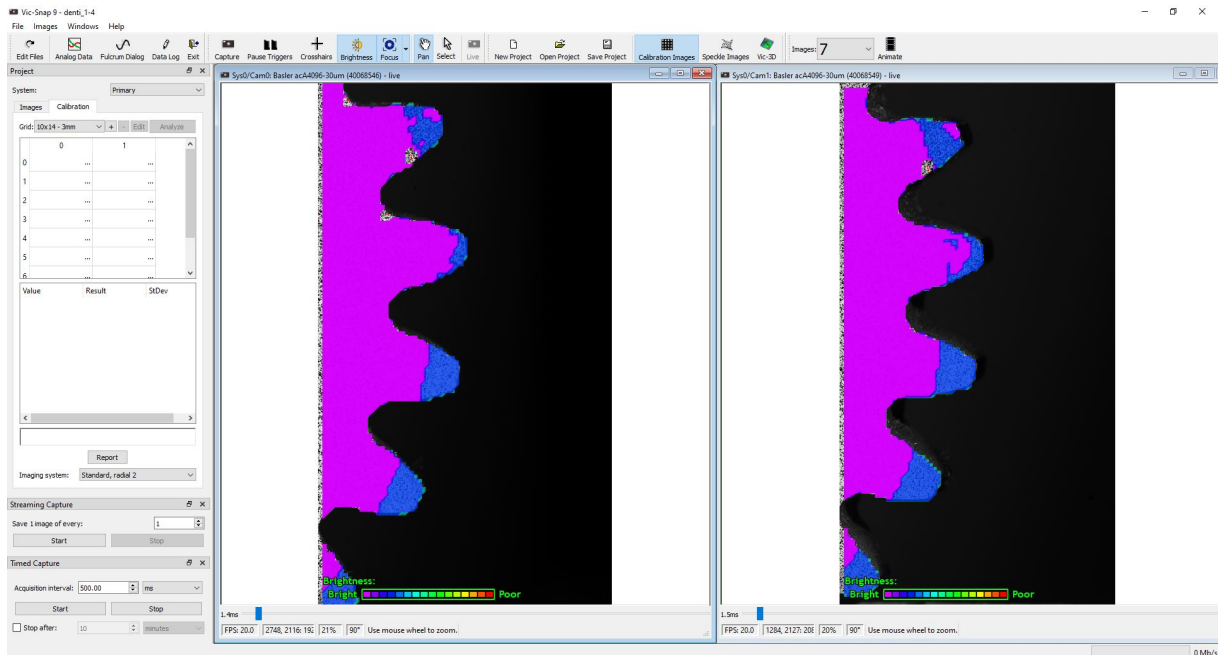


Figure 2.49: Brightness and Focus - Shot-Peened Gear

2.5. Experimental 3D-DIC - Bending Test

A bending test was conducted applying through a punch four loads of stress to the gear tooth, following the ISO 6336 standards ([2], [3]). Each type of gear, namely Standard Gear, Thin Rim Gear, Shot-Peened Gear, and Non-Shot Peened Gear, was subjected to four approximate loads of around 2000N, 4000N, 6000N, and 8000N. During the execution of this process, the DIC system captured images at a frame rate of 20 fps.[6]

The following Table 2.3 summarizes the experimental DIC settings and performance adopted during the analysis.[6]

Table 2.3: 3D Digital Image Correlation Parameters

Technique used	3D Digital Image Correlation
Subset size	about 61x61 pixel ²
Subset weight	Gaussian weight
Step	11 pixel
Investigated area	about 9x9 mm ²
Shape function	Affine
Interpolation Function	Optimized 8-tap
Correlation criterion	Normalized squared differences
Smoothing applied to the image	Low-pass filter image
Displacement accuracy	1/100 of the field of view (in-plane rule-of-thumb)
Strain resolution	100 $\mu \epsilon$ (microstrain)
Differentiation method	Lagrange
Smoothing method	Lagrange - dimension 25

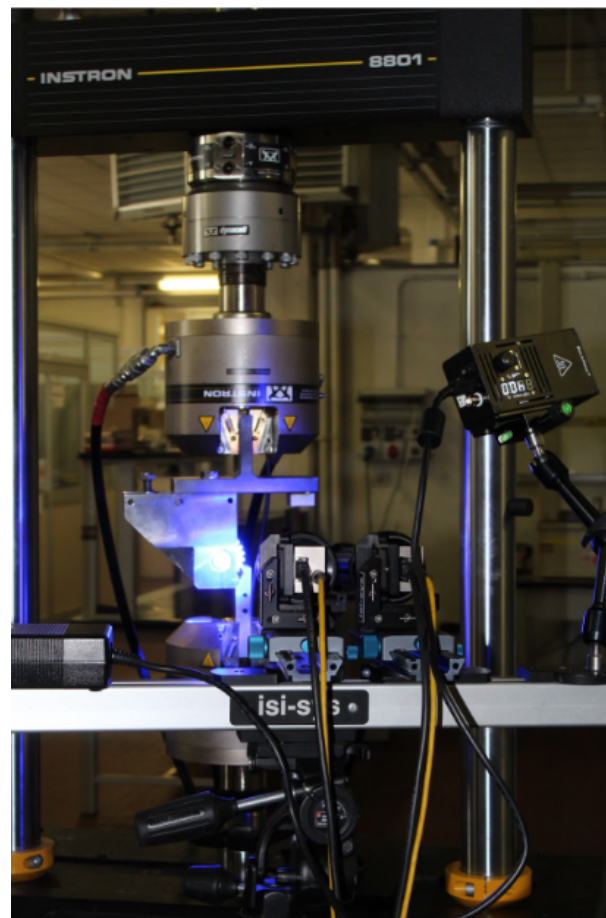


Figure 2.50: Images/Experimental analysis with Digital Image Correlation

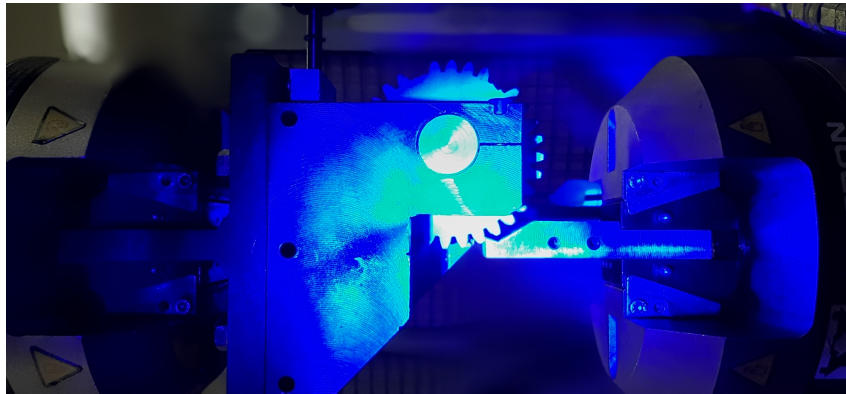


Figure 2.51: Image acquisition and loading application during bending test of a standard gear

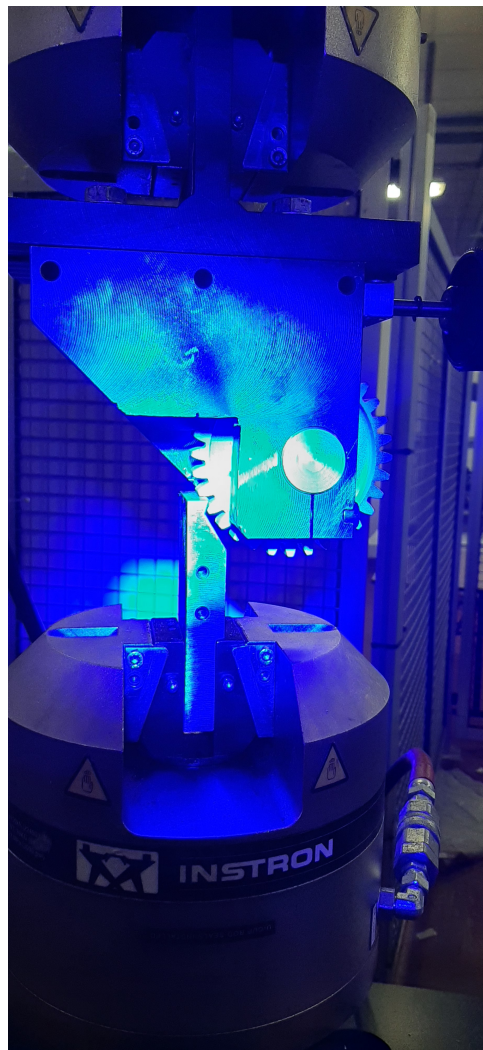


Figure 2.52: Image acquisition and loading application during bending test of a thin-rim gear

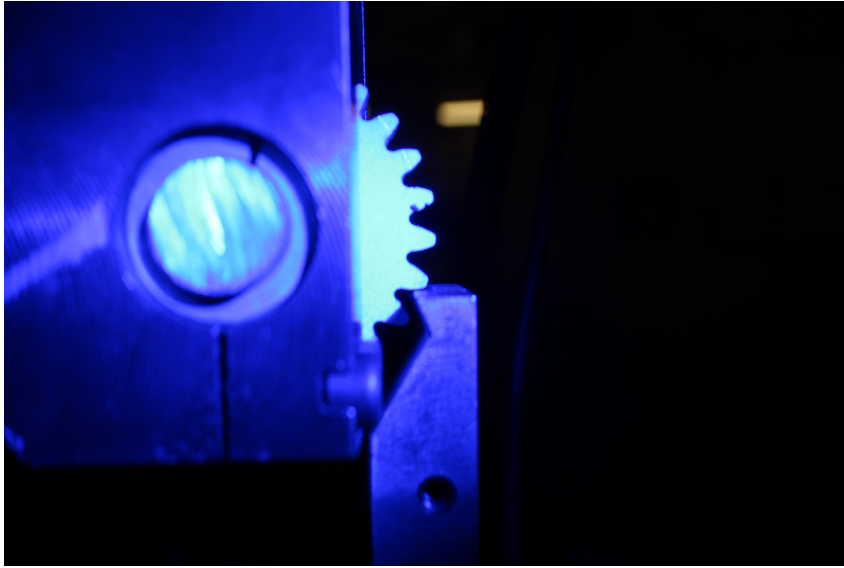


Figure 2.53: Image acquisition and loading application during bending test of a shot-peened gear

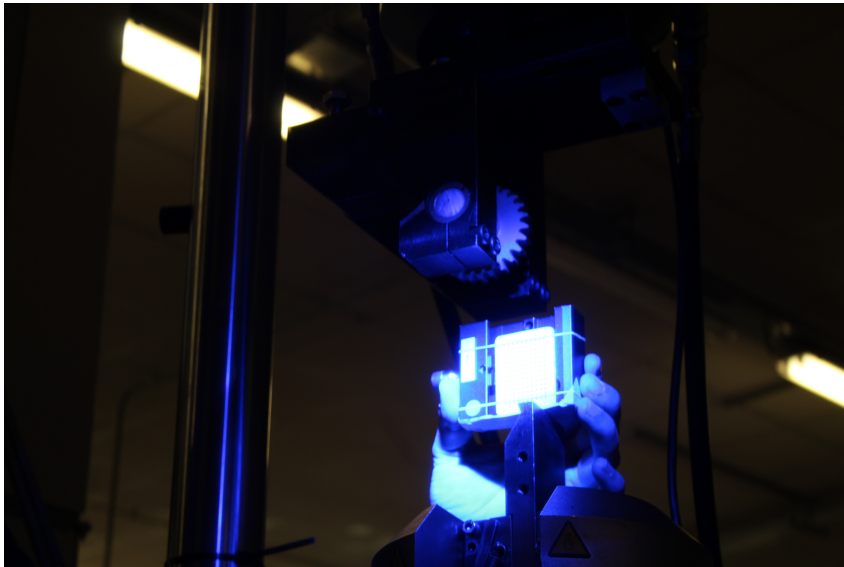


Figure 2.54: Calibration acquisition before of bending test of a non-shot-peened gear

2.5.1. ROI and Subset

The subset size controls the area of the image that is used to track the displacement between images. The subset size has to be large enough to ensure that there is a sufficiently distinctive pattern contained in the area used for correlation. If you change the subset size, you will see the current size illustrated by a grid briefly displayed on the AOI.[20]

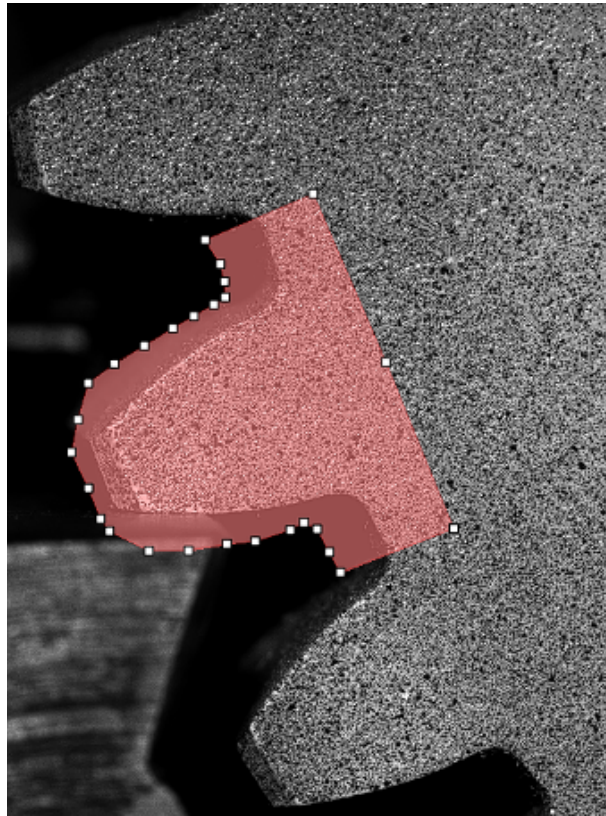


Figure 2.55: Region Of Interest (ROI) made with VIC 3D Software

The step size controls the spacing of the points that are analyzed during correlation. If a step size of 1 is chosen, a correlation analysis is performed at every pixel inside the area-of-interest. A step size of 2 means that a correlation will be carried out at every other pixel in both the horizontal and vertical direction, etc.[20]

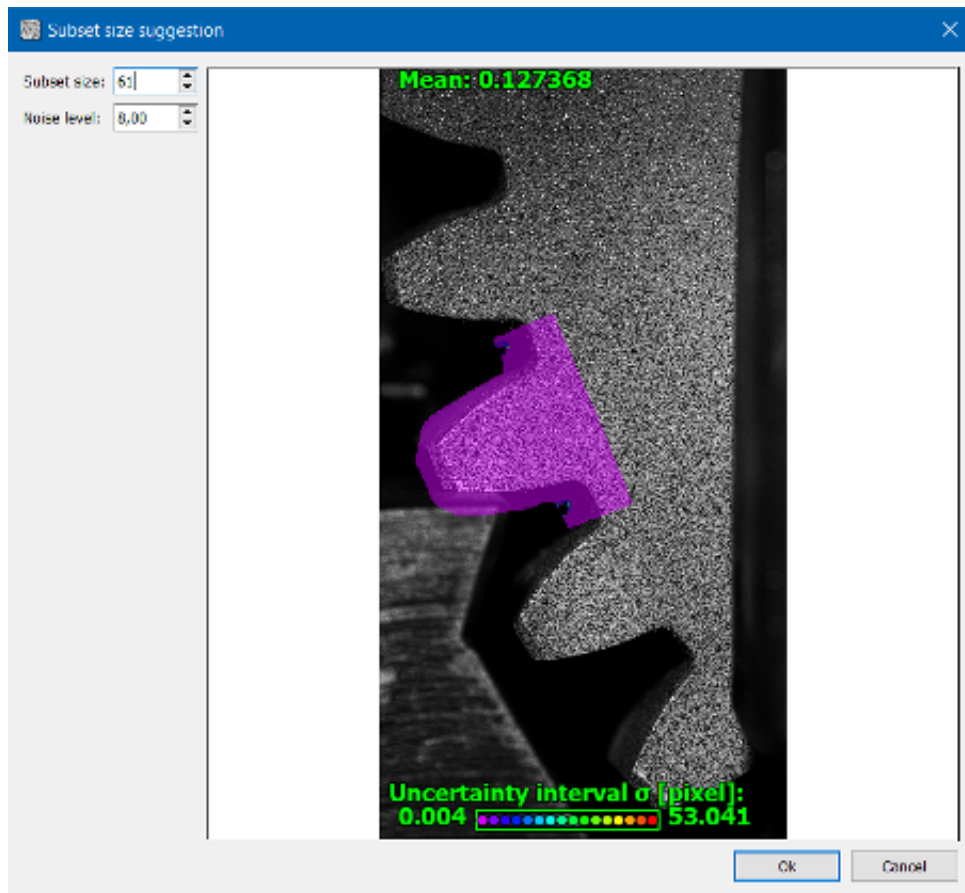


Figure 2.56: Selection of subset parameters with indication of external noise using VIC 3D software

2.5.2. Local Reference System

The local reference system of the DIC (Digital Image Correlation) used for conducting the analyses was created based on the geometry of the wheel, as shown in the figure. By overlaying the images acquired through DIC with the CAD drawing of the wheel, two reference points are determined. Subsequently, through a geometric construction, the origin of the local reference system for the wheel is obtained. This local reference system allows for the evaluation and analysis of deformations and stresses in the wheel during loading or usage.

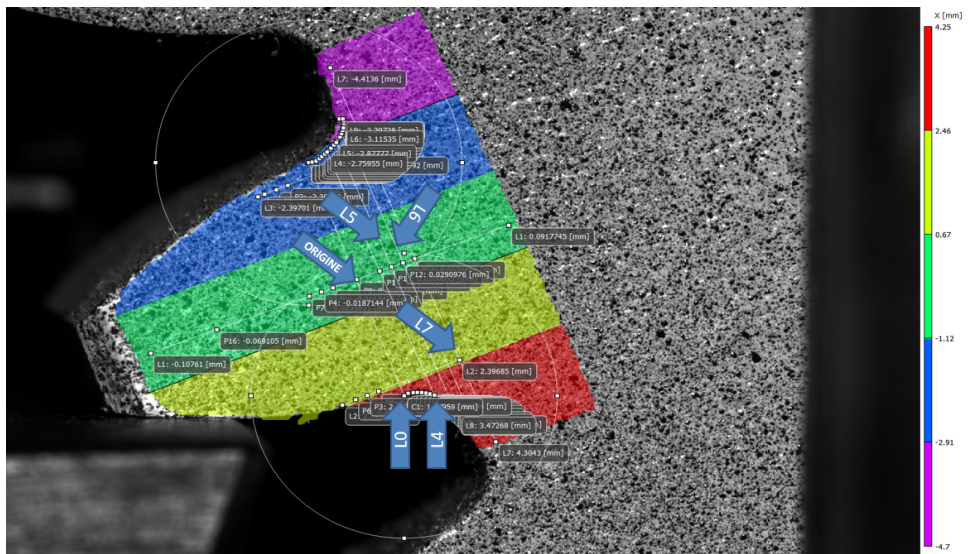


Figure 2.57: Geometric calculation for the determination of the reference system

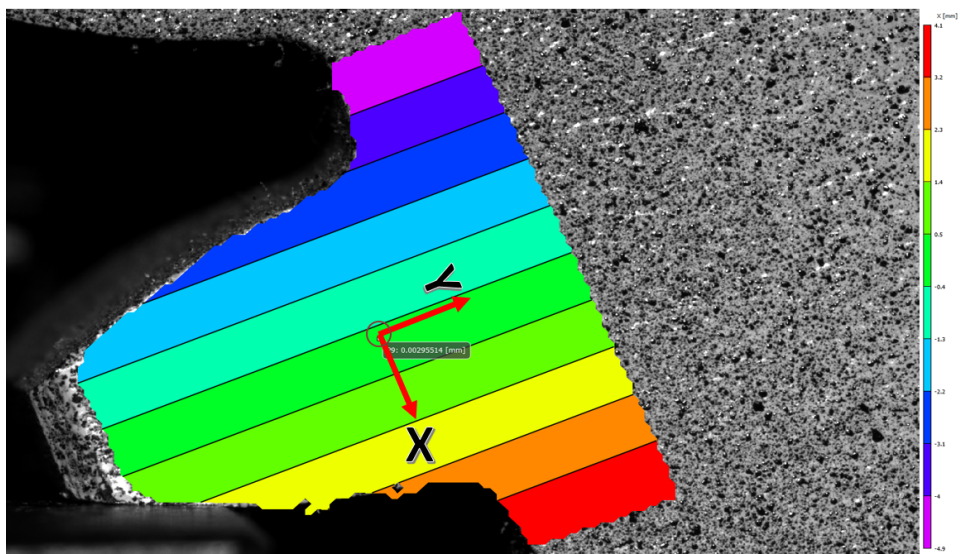


Figure 2.58: Local Reference System - Standard Gear

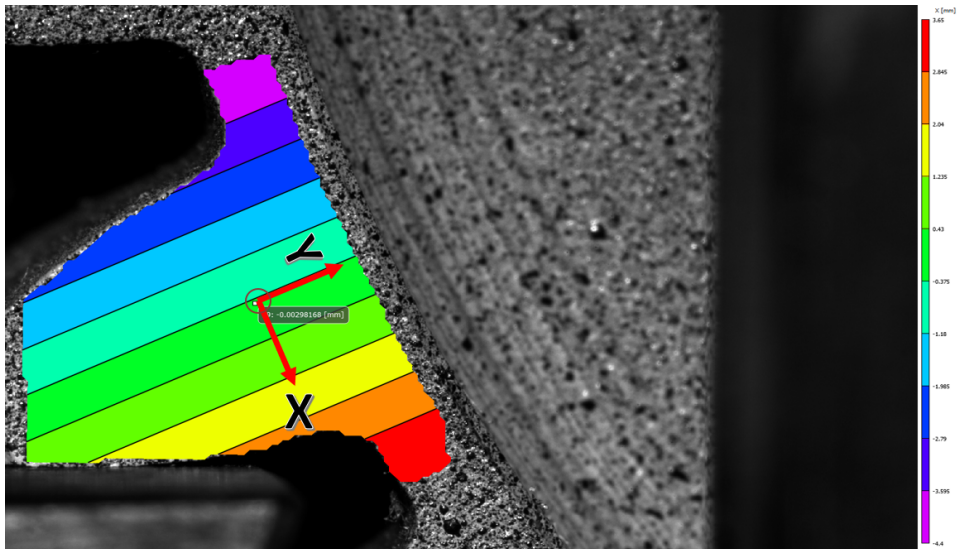


Figure 2.59: Local Reference System - Thin Rim Gear

3 | Experimental Results and Discussion

The results obtained from VIC 3D at the maximum load of 7980 N, stabilized, can be represented through a contour mapping. This representation will allow visualizing the distribution of deformations, principal strains, and principal angles. The additional results from tests 1 to 3 will be included in the appendix, providing further details on the material's behavior. Subsequently, we will proceed to analyze the material's response in a gear where there is a change in its geometry.

3.1. Standard Gear - Load 4

3.1.1. Local strain maps ϵ_{xx}

In this figure 3.1, it can be observed that the tooth is subjected to bending due to the tangential force applied to the tooth, which adds to the deformations obtained from bending.

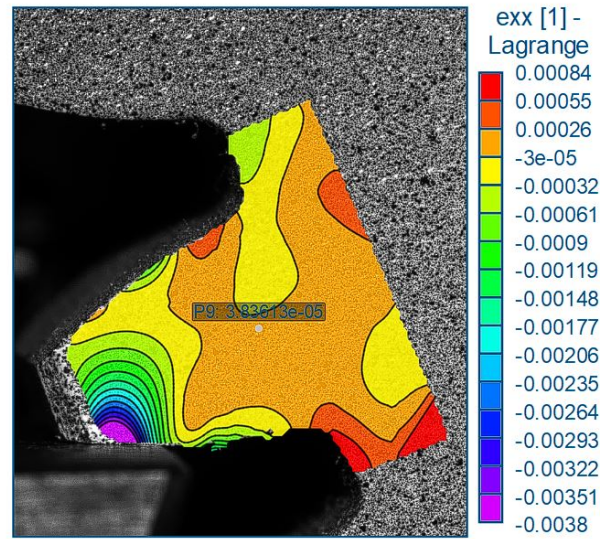


Figure 3.1: Standard gear: local strain in the X-direction map ϵ_{xx} - Load 4

3.1.2. Local strain maps ϵ_{yy}

In the analysis of the bending test, the material's response is observed. The local strain map ϵ_{yy} can be compared to the behavior of the tooth profile according to Lewis theory.

In the distribution of deformations, a nearly uniform trend is observed from the compression zone to the tension zone. However, on the neutral plane, the bending effect is not observed, only the compression effect. If the tooth is modeled as a beam, it can be noticed how the normal stress is uniformly distributed, without the presence of the notch effect that could be present in other configurations (Figure 3.2).

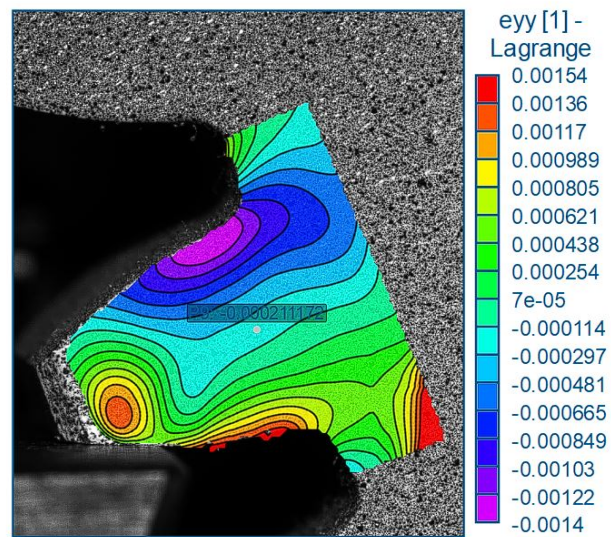


Figure 3.2: Standard gear: local strain in the Y-direction map ϵ_{yy} - Load 4

3.1.3. Local strain maps ϵ_{xy}

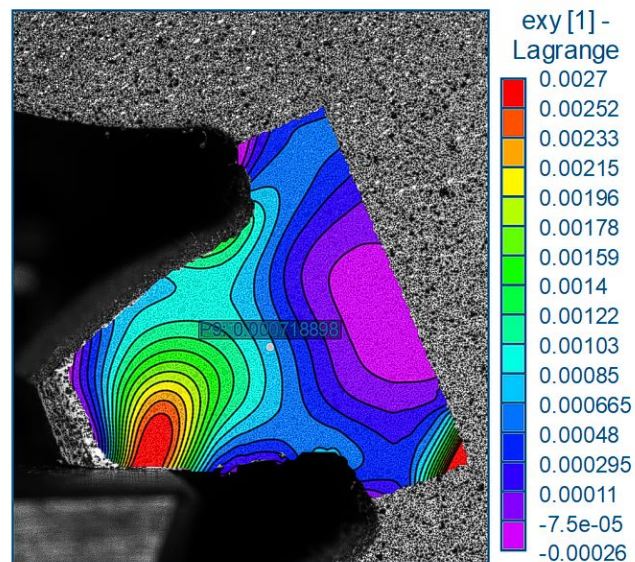


Figure 3.3: Standard gear: local shear strain map ϵ_{xy} - Load 4

The figure 3.3 illustrates a predominant effect in the contact zone between the punch and the tooth. This effect generates Hertzian-type stresses. As we move towards the body of the gear, the effect gradually decreases until it disappears completely. However, in the compression zone, shear plays an important role in the potential material fracture.

3.1.4. Local strain maps ϵ_1

In the figure 3.4, it is observed that the maximum deformation occurs in the tension zone, in accordance with the theory of maximum stress at the base of the tooth. It is important to consider the effect of the notch at the root of the tooth, as it can influence the stress distribution and the possibility of material failure.[11]

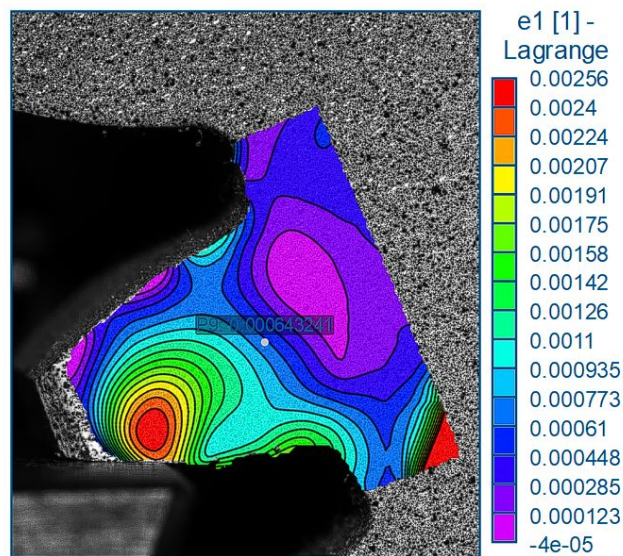


Figure 3.4: Standard gear: major principal strain map ϵ_1 - Load 4

3.1.5. Local strain maps ϵ_2

In the figure, it can be observed that there is a minimal compressive stress, even in the tooth root area of the traction zone.

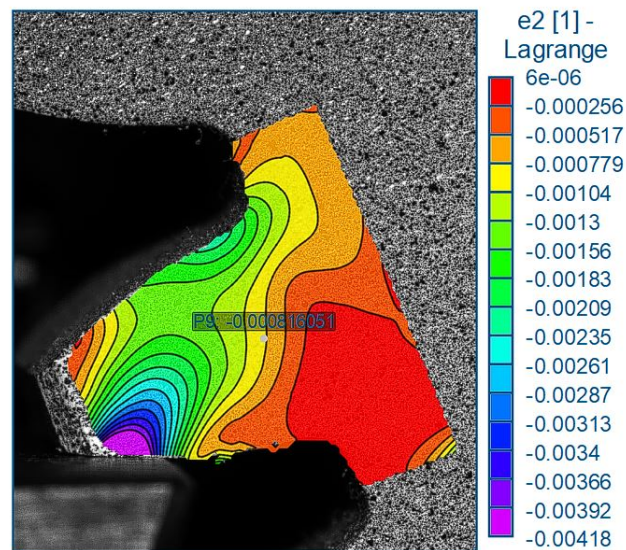


Figure 3.5: Standard gear: minor principal strain map ϵ_2 - Load 4

3.1.6. Local strain maps γ_1

In the figure 3.6, it is observed that at the origin, the material has a principal angle of approximately 45° , which corresponds to a specific feature or arrangement of the component. Furthermore, it is noted that the maximum deformation occurs at an angle of approximately 58° , indicating a significant variation in the configuration or applied load on the material.

The measurement of the gamma angle in the figure 3.6 is obtained by considering the variation of the angle with respect to the X-axis counterclockwise.

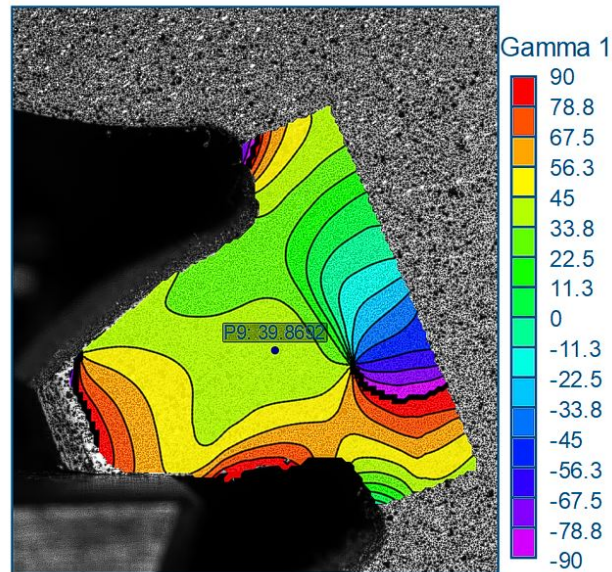


Figure 3.6: Standard gear: principal strain angle map γ_1 - Load 4

3.2. Thin-Rim Gear - Load 4

3.2.1. Local strain maps ϵ_{xx}

The tooth is under compression in the central part, while tension is observed at the tooth root's end on the side of the force. A uniform distribution process can be noticed where the tangential force generates deformation, decreasing gradually as one moves from the tooth axis towards the tooth root on the compression side. (Figura 3.7)

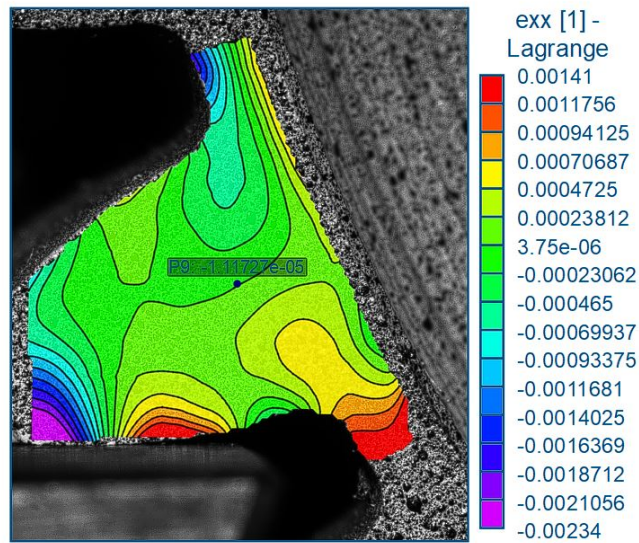


Figure 3.7: Thin-rim gear: local strain in the X-direction map ϵ_{xx} - Load 4

3.2.2. Local strain maps ϵ_{yy}

In the figure 3.8, it is observed that the wheel is subjected only to tension, while the effect of compression (normal force) is either not present or negligible. This means that the analysis focuses primarily on the effect of the tensile force on the wheel, without considering the effect of the tooth or any compressive forces that could affect the stress distribution. Therefore, the attention is primarily directed towards the analysis of stresses and deformations caused by the tensile force on the crown of the Thin-Rim Gear.

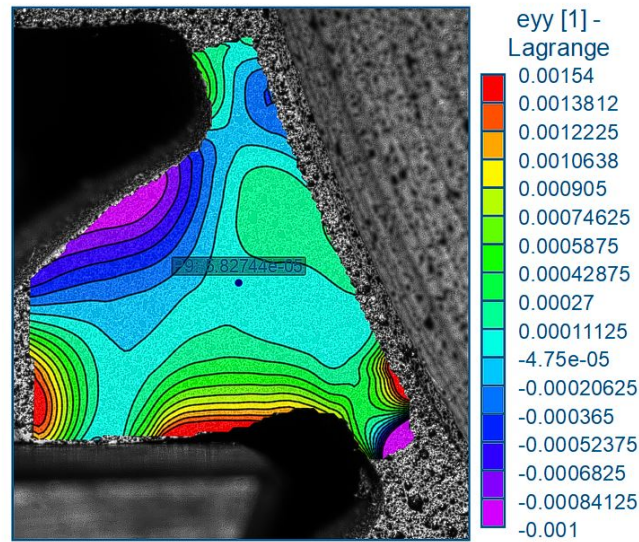


Figure 3.8: Thin-rim gear: local strain in the Y-direction map ϵ_{yy} - Load 4

3.2.3. Local strain maps ϵ_{xy}

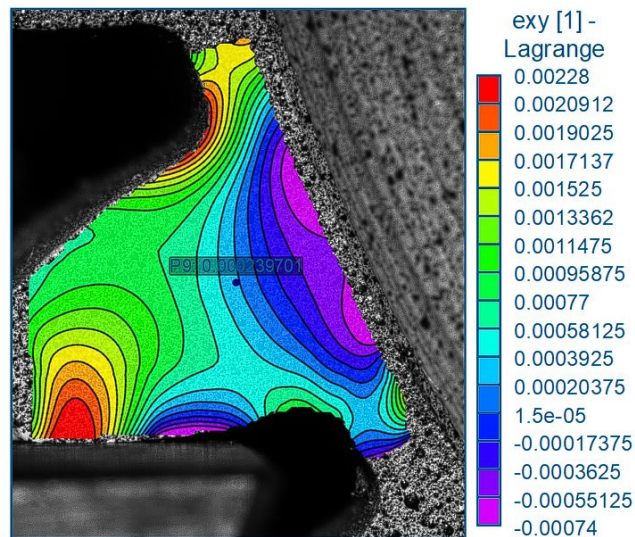


Figure 3.9: Thin-rim gear: local shear strain map ϵ_{xy} - Load 4

In the Figure 3.9, the contribution of tangential deformation is evident both on the compression side of the tooth (tooth root) and in the contact area with the punch, increasing Herzian stress.

3.2.4. Local strain maps ϵ_1

The study examined how both rim and web thickness influence the stress distribution in the gears. The findings indicate that when the backup ratio values are greater than 0.75, there is minimal impact on the stress at the tooth root. However, as the backup ratio value decreases below 0.75, the maximum fillet stress experiences a significant increase. Moreover, the more the web thickness is increased, the more the stress concentration factor decreases. [5]

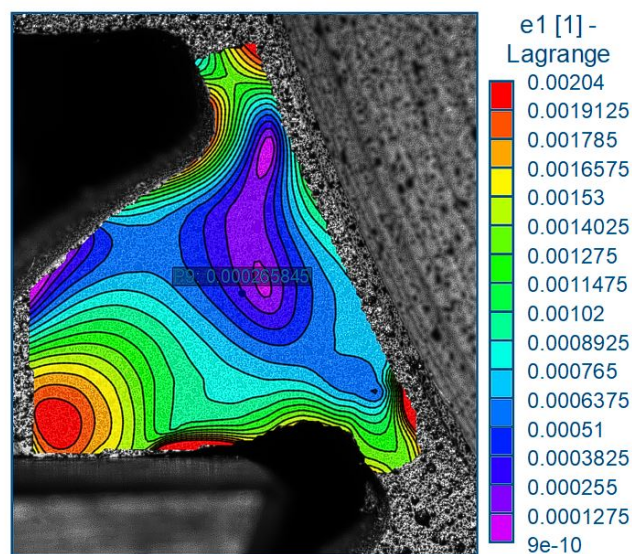


Figure 3.10: Thin-rim gear: major principal strain map ϵ_1 - Load 4

3.2.5. Local strain maps ϵ_2

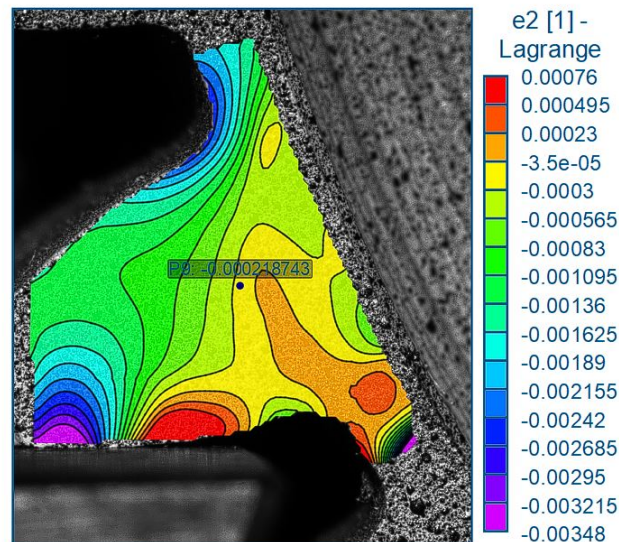


Figure 3.11: Thin-rim gear: minor principal strain map ϵ_2 - Load 4

It can be observed from the figure that the minimum deformation values are due to compression. It can be seen that on the bottom side of the tooth, specifically in the compression area, we have the minimum value of deformation with a uniform trend.

3.2.6. Local strain maps γ_1

In the Figure 3.12, high values of FAMs (Maximum Amplitude Factors) can be observed in the region of the contact line because the stress values concentrate in that area. As we move towards the center of the wheel, a rapid change in the direction of the principal deformations can be observed due to the wheel's behavior becoming more variable inside the rim.

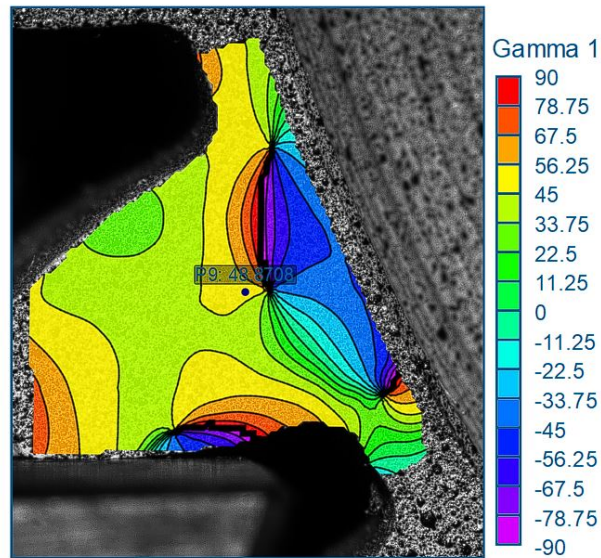


Figure 3.12: Thin-rim gear: principal strain angle map γ_1 - Load 4

3.3. Shot-Peened Gear - Load 3

The experiment did not succeed because the gear moved while applying the load. This led to an inconsistent behavior, which excludes these gears from the results analysis. Below are the images 3.13, 3.14, 3.15 obtained with Digital Image Correlation (DIC) to identify the issues that may occur in such gears.

3.3.1. Local strain maps ϵ_{yy}

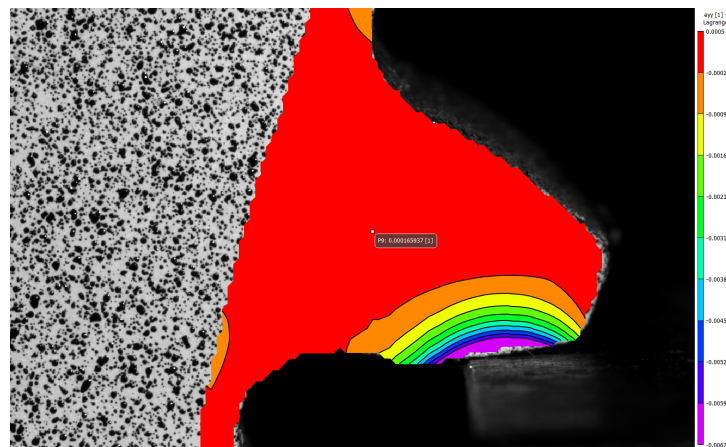


Figure 3.13: Shot-Peened Gear: local strain in the Y-direction map ϵ_{yy} - Load 3

3.3.2. Local strain maps ϵ_1

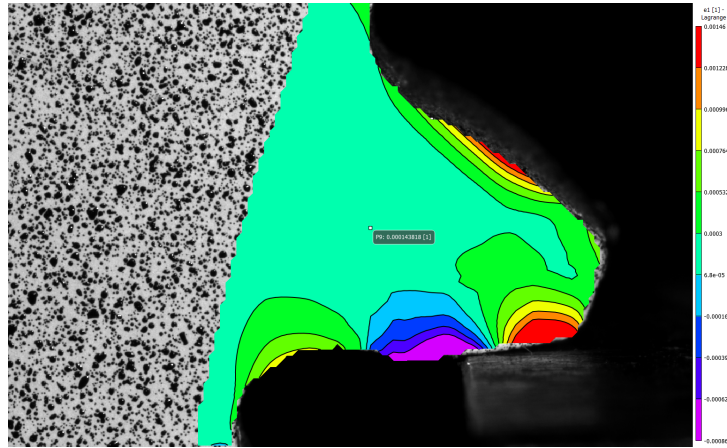


Figure 3.14: Shot-Peened Gear: major principal strain map ϵ_1 - Load 3

3.3.3. Local strain maps γ_1

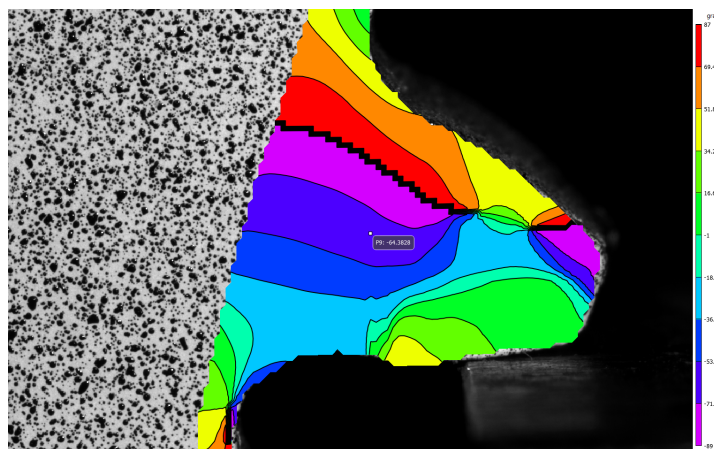


Figure 3.15: Shot-Peened Gear: principal strain angle map γ_1 - Load 3

3.4. Non-Shot-Peened Gear - Load 3

The experiment did not succeed because the gear moved while applying the load. This led to an inconsistent behavior, which excludes these gears from the results analysis. Below are the images 3.16, 3.17, 3.18 obtained with Digital Image Correlation (DIC) to identify the issues that may occur in such gears.

3.4.1. Local strain maps ϵ_{yy}

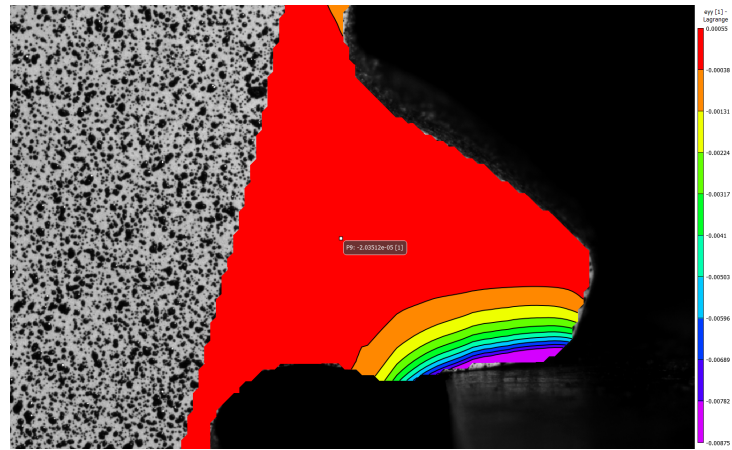


Figure 3.16: Non-shot-peened gear:local strain in the Y-direction map ϵ_{yy} - Load 3

3.4.2. Local strain maps ϵ_1

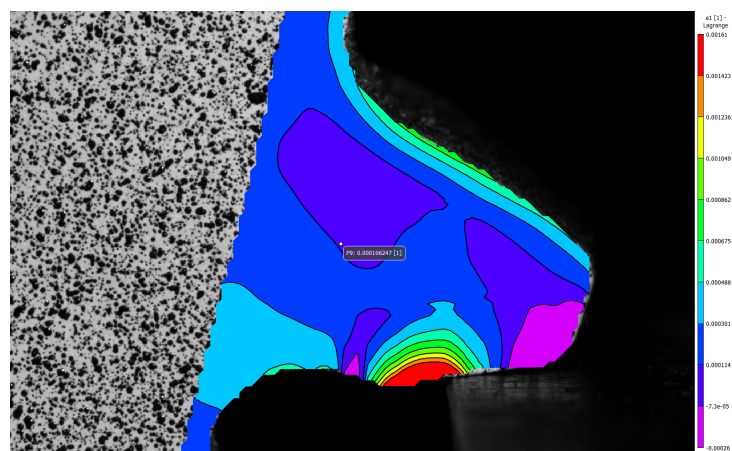


Figure 3.17: Non-shot-peened gear:local strain in the Y-direction map ϵ_1 - Load 3

3.4.3. Local strain maps γ_1

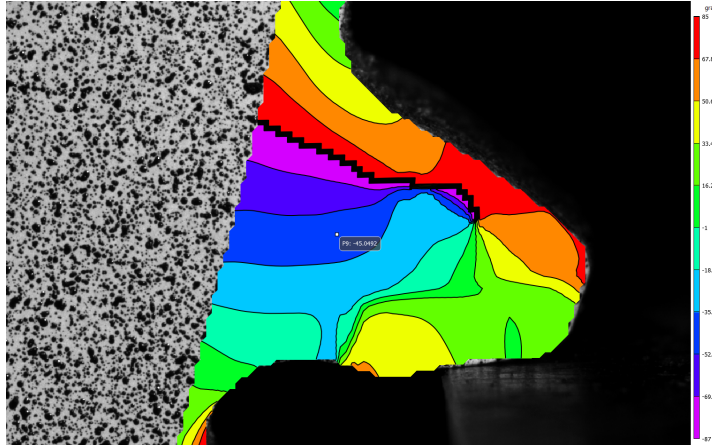


Figure 3.18: Non-shot-peened gear:local strain in the Y-direction map γ_1 - Load 3

3.5. Data Analysis - Load 4

In this section, the graphs of the data obtained from DIC are presented, analyzed along different contour lines to understand how they respond to the applied stresses. An effort has been made to compare their positions to understand any behavioral differences at the same point. In the appendix, the results of a Finite Element Model (FEM) are provided to validate the findings and confirm the accuracy of DIC. By adopting a theoretical approach first and a numerical approach later, an attempt has been made to assess the reliability of the data analysis results.

3.5.1. Local strain maps ϵ_{xx}

It can be observed that the behavior of the gear wheel exhibits a combination of compressive and tensile forces, with higher deformations in the lightweight wheel due to the lack of rigid elements in the material. Additionally, it is noticeable that the standard gear has a higher tensile value on the side where the tooth engages, while the Thin Rim experiences compression on that side. As one moves towards the interior of the rim, the deformations increase because lightweight wheels lack a wheel body that can withstand the load. In other words, the absence of rigid elements in the material of the thin rim gear leads to greater deformation when subjected to high stress or loads as in Figure 3.19, 3.20 and 3.21.

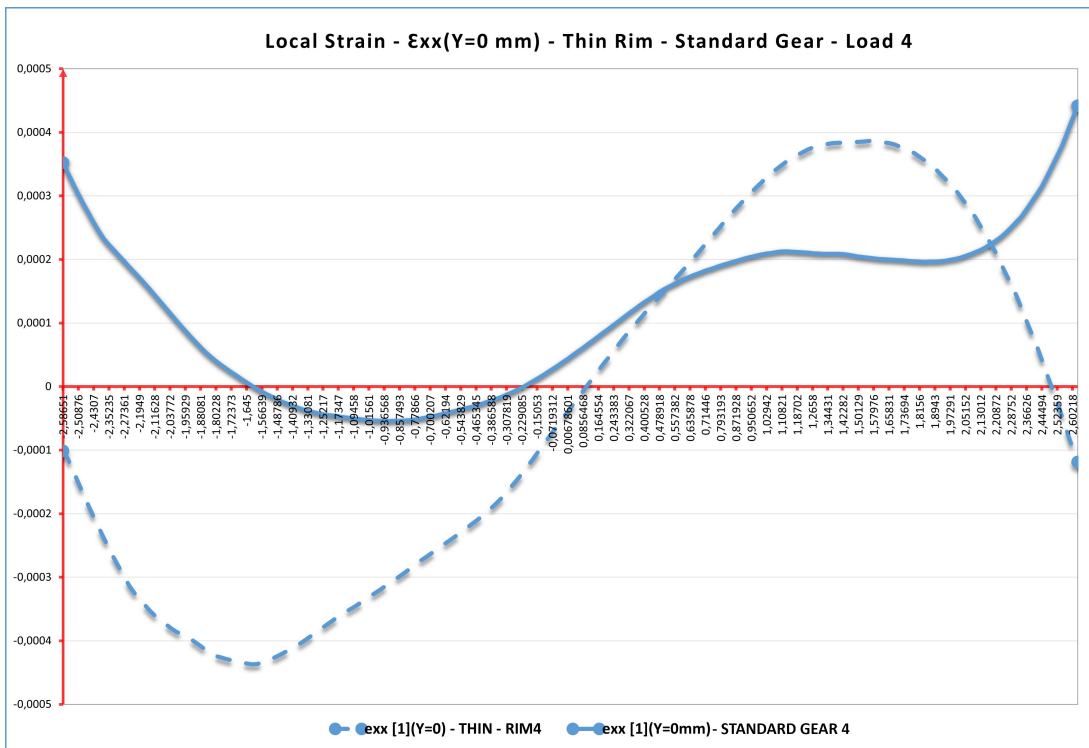


Figure 3.19: Local Strain - $\epsilon_{xx}(Y=0 \text{ mm})$ - Thin Rim - Standard Gear - Load 4

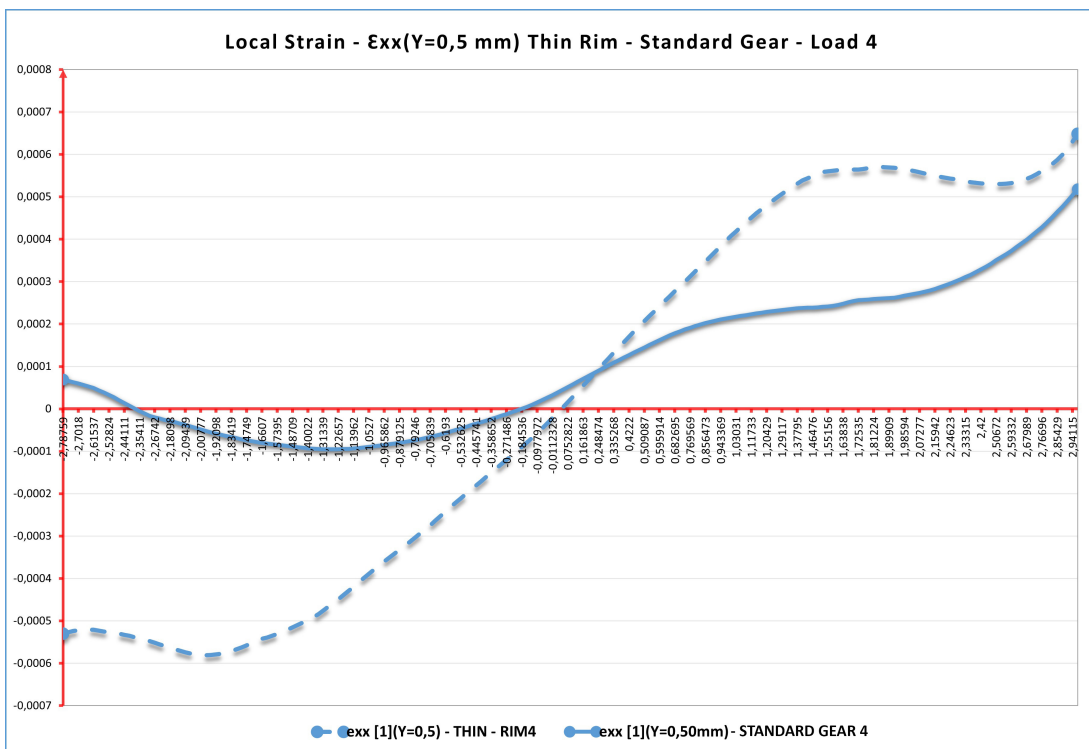


Figure 3.20: Local Strain - $\epsilon_{xx}(Y=0,5 \text{ mm})$ - Thin Rim - Standard Gear - Load 4

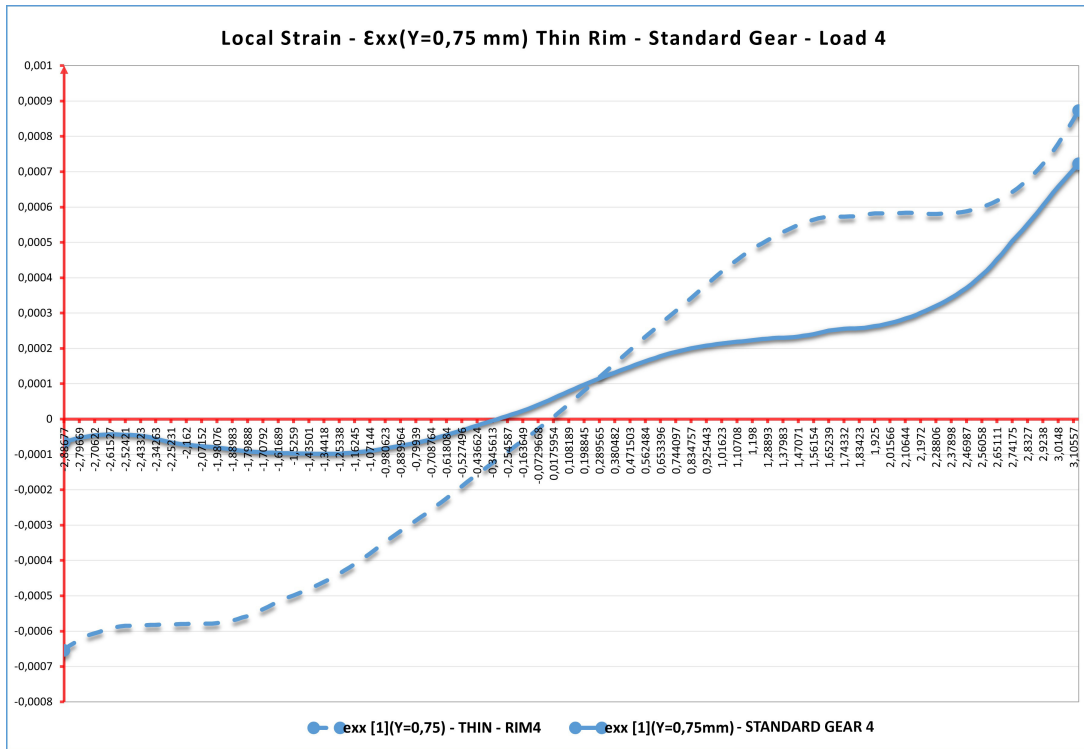


Figure 3.21: Local Strain - $\epsilon_{xx}(Y=0,75 \text{ mm})$ - Thin Rim - Standard Gear - Load 4

3.5.2. Local strain maps ϵ_{yy}

In 3.22, 3.23 and 3.24, it can be observed that at each tooth subjected to a load, there is simultaneous tension and compression due to bending (Lewis). At the tooth root, a more complex state of stress is observed, where the compressed side has a higher value of ϵ_{yy} deformation because the effects of bending and compression add up. As one moves towards the center, the ϵ_{yy} value increases on the compressed side, while in the Thin Rim gear, there is a smaller variation. The thin rim gear generates a local strain different, due to its low stiffness under the central part of the face width causing a tooth rotation during bending condition. [6].



Figure 3.22: Local Strain - $\epsilon_{yy}(Y=0 \text{ mm})$ - Thin Rim - Standard Gear - Load 4

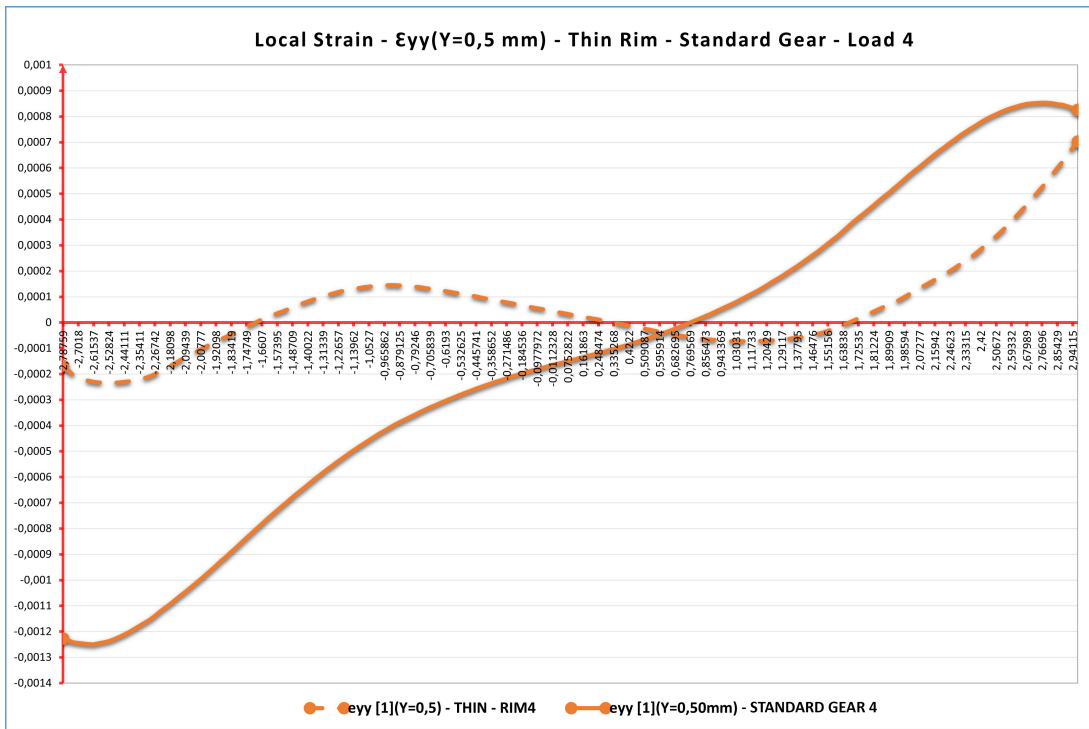


Figure 3.23: Local Strain - $\epsilon_{yy}(Y=0,5 \text{ mm})$ - Thin Rim - Standard Gear - Load 4

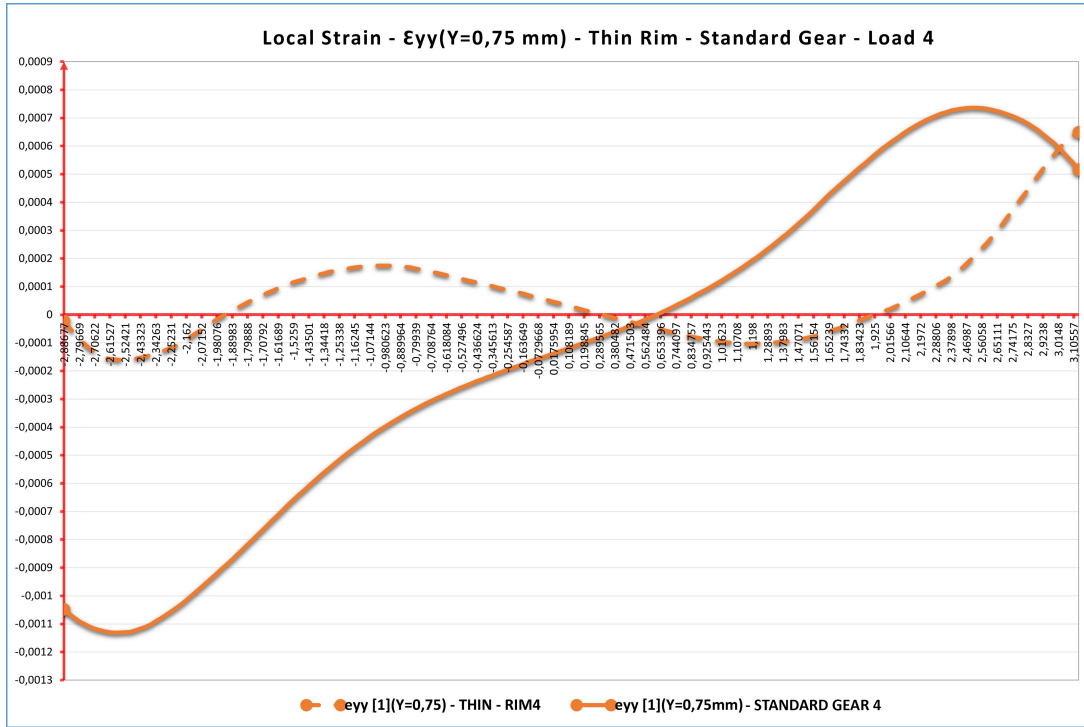


Figure 3.24: Local Strain - $\epsilon_{yy}(Y=0,75 \text{ mm})$ - Thin Rim - Standard Gear - Load 4

3.5.3. Local strain maps ϵ_{xy}

In these graphs 3.25, 3.26, 3.27 the shear values obtained along the baseline are observed. A convex trend was expected; however, the result showed a concave trend. These deformations are due to Hertzian stresses created by the contact between the punch and the gear tooth. It is observed that as we move closer to the center of the gear, the deformations decrease. There is also a lower deformation observed in the thin-rim gear compared to the standard one.

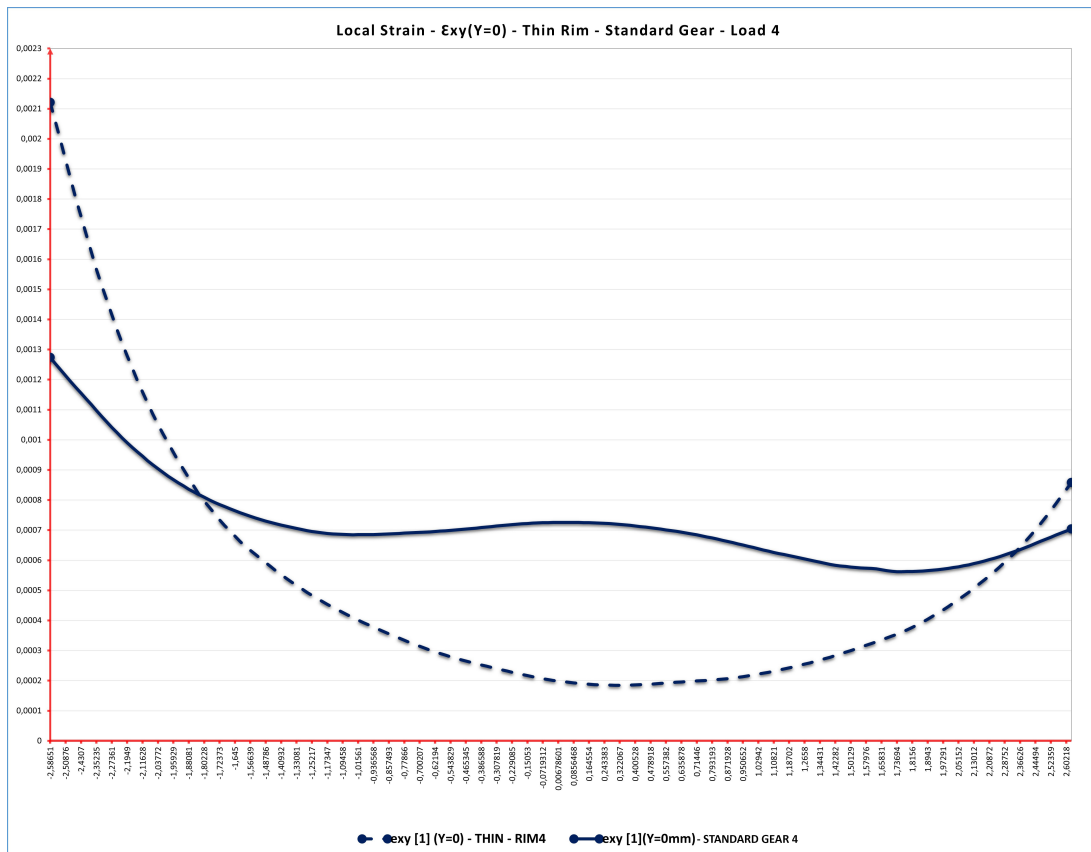


Figure 3.25: Local Strain - $\epsilon_{xy}(Y=0 \text{ mm})$ - Thin Rim - Standard Gear - Load 4

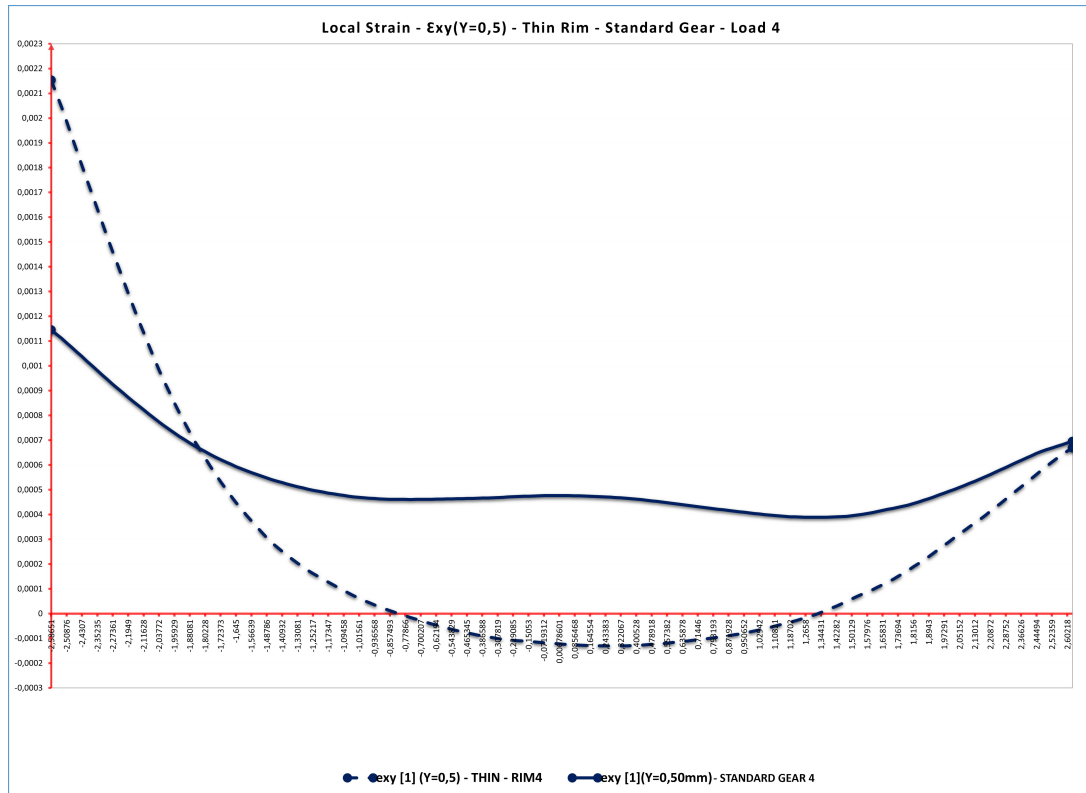


Figure 3.26: Local Strain - $\epsilon_{xy}(Y=0,5 \text{ mm})$ - Thin Rim - Standard Gear - Load 4

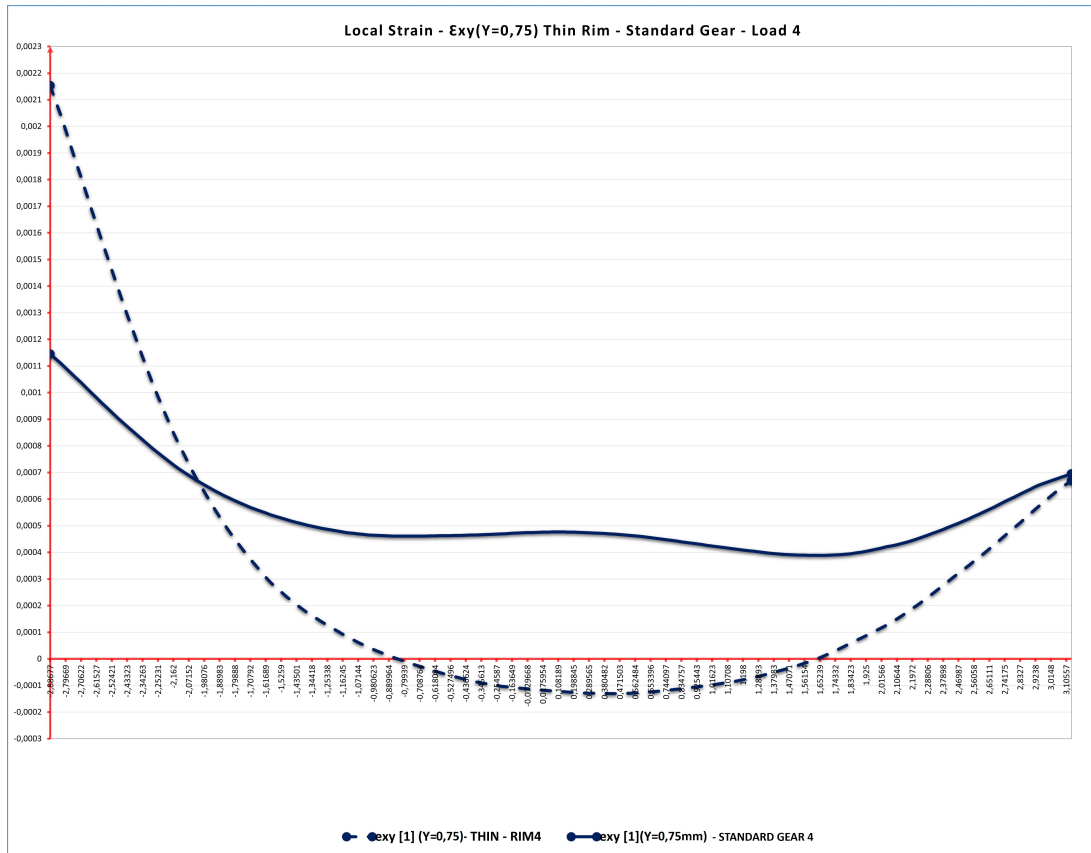


Figure 3.27: Local Strain - $\epsilon_{xy}(Y=0,75 \text{ mm})$ - Thin Rim - Standard Gear - Load 4

3.5.4. Local strain maps ϵ_1

It is observed that in the standard gear, the maximum deformation value is located on the tension side at the tooth root. In the thin-rim gear, the behavior is opposite, with the maximum tension located on the compression side. It has been determined that the maximum stress value is positioned at the center of the tooth band. However, thanks to Digital Image Correlation (DIC), a first approach is proposed for determining the maximum deformation that could cause failure.(Figure 3.28, 3.28, 3.28). [5]

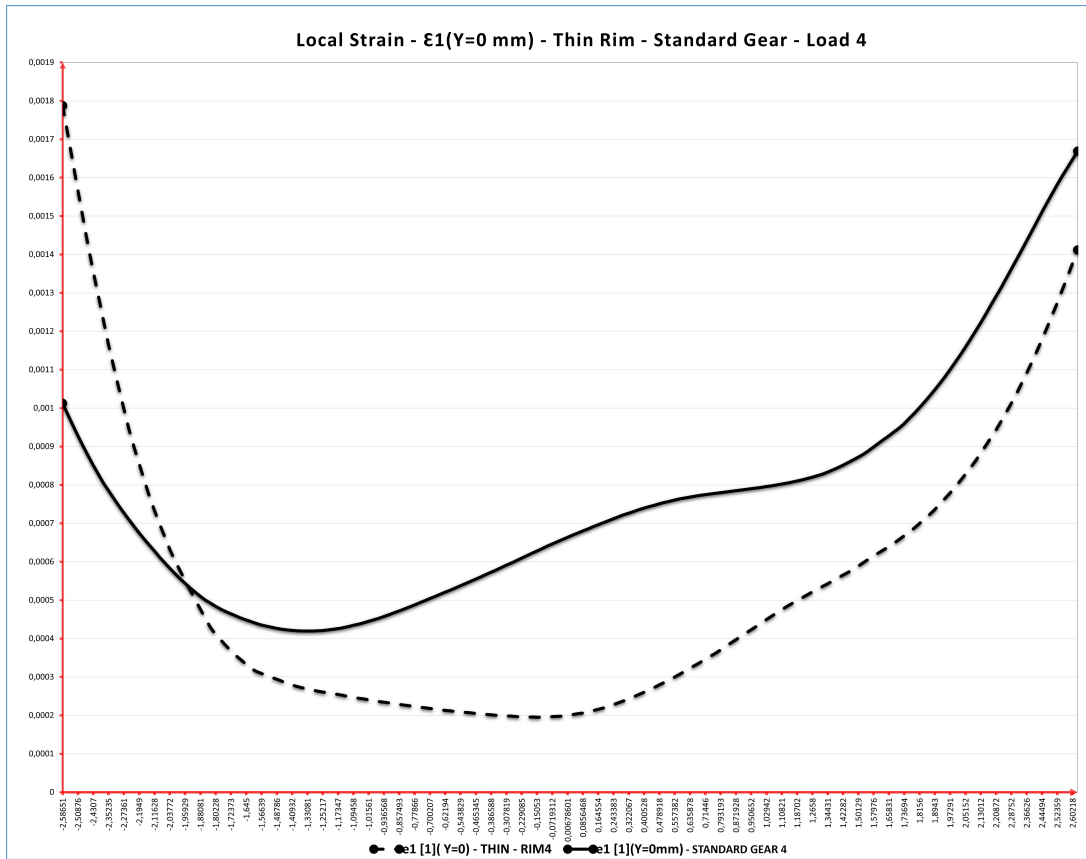


Figure 3.28: Local Strain - $\epsilon_1(Y=0$ mm) - Thin Rim - Standard Gear - Load 4

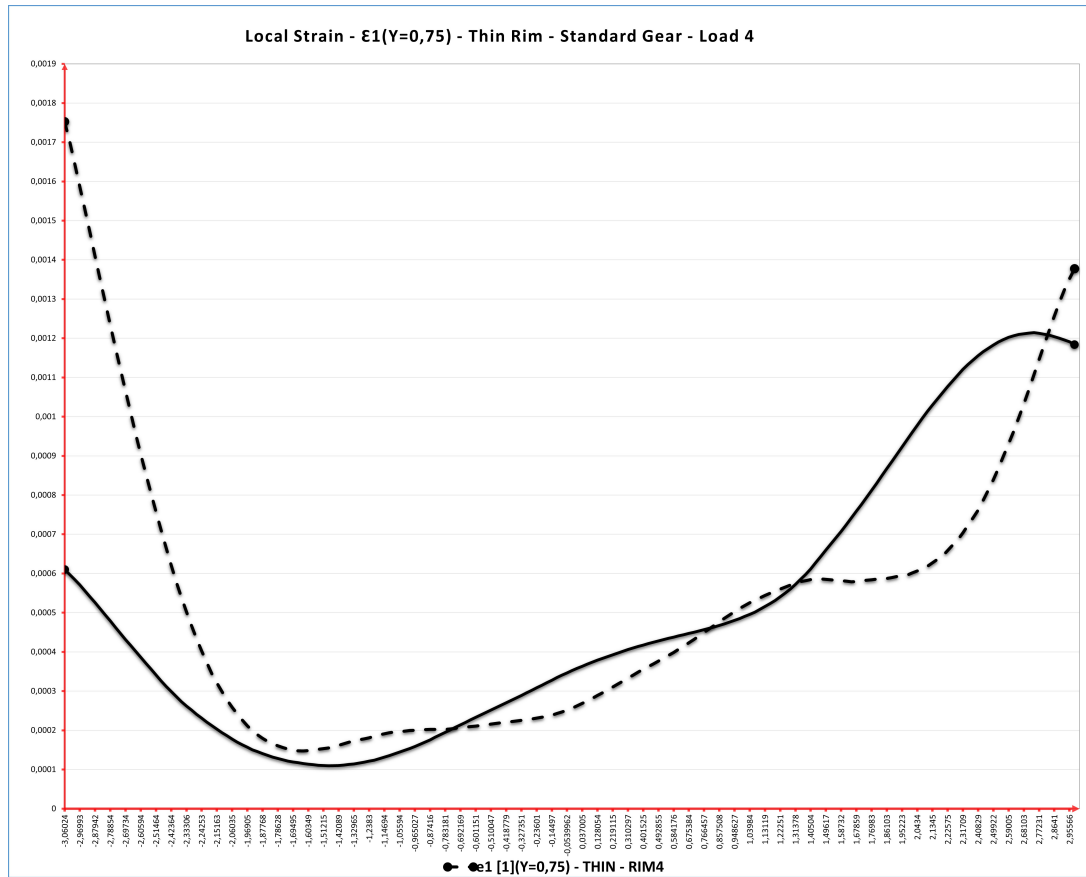


Figure 3.30: Local Strain - $\epsilon_1(Y=0,75)$ - Thin Rim - Standard Gear - Load 4

3.5.5. Local strain maps γ_1

Knowing the position of the point with maximum deformation is essential. In the standard gear, it was determined through numerical methodology that the position of the maximum value varies from 30° to 34° on the tooth side [5]. Meanwhile, in the thin-rim gear with a $mb=0.3$, a principal angle of 60° has been determined. It is observed that DIC closely approaches these results, validating its accuracy and reliability [9].

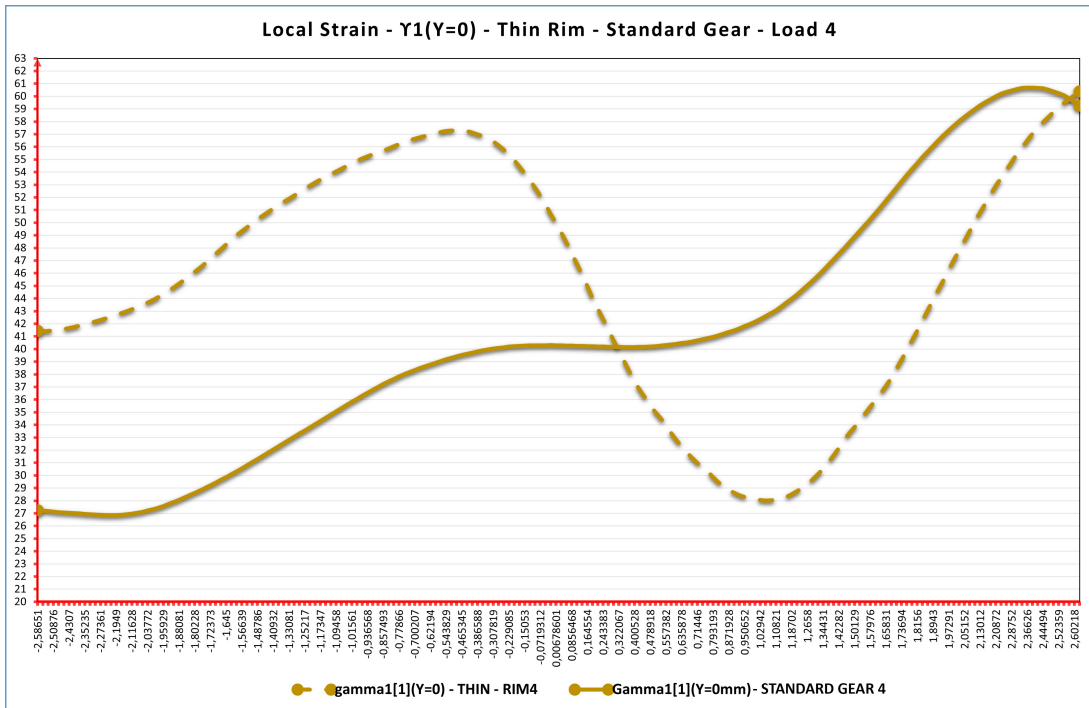


Figure 3.31: Local Strain - $\gamma_1(Y=0 \text{ mm})$ - Thin Rim - Standard Gear - Load 4

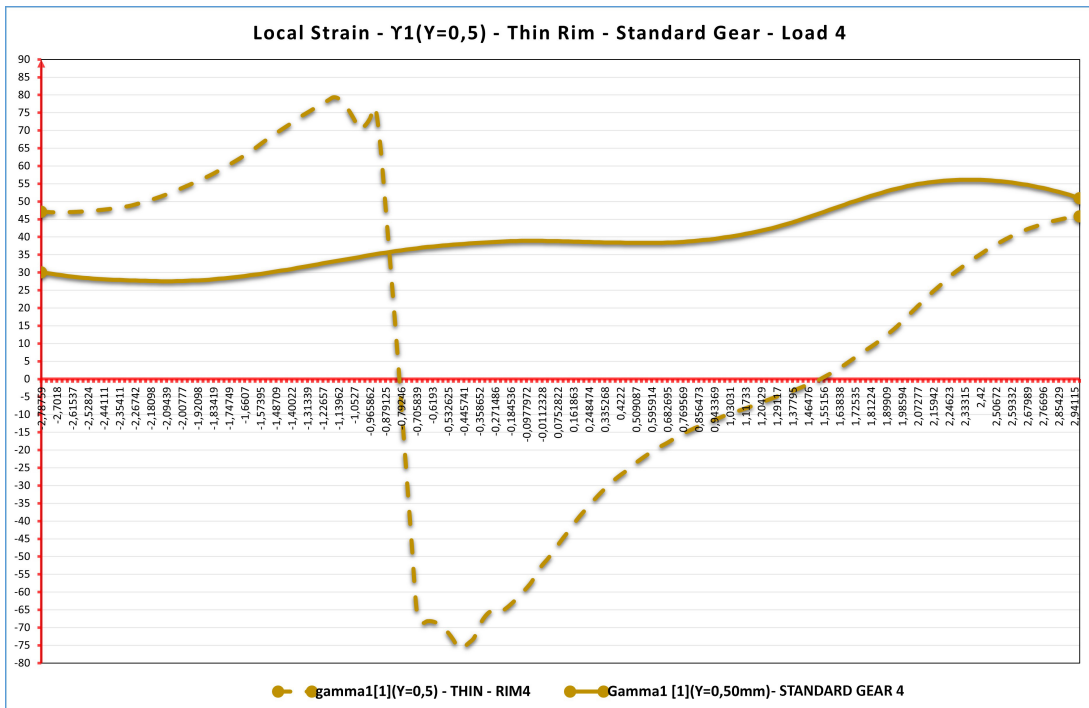


Figure 3.32: Local Strain - $\gamma_1(Y=0,5 \text{ mm})$ - Thin Rim - Standard Gear - Load 4

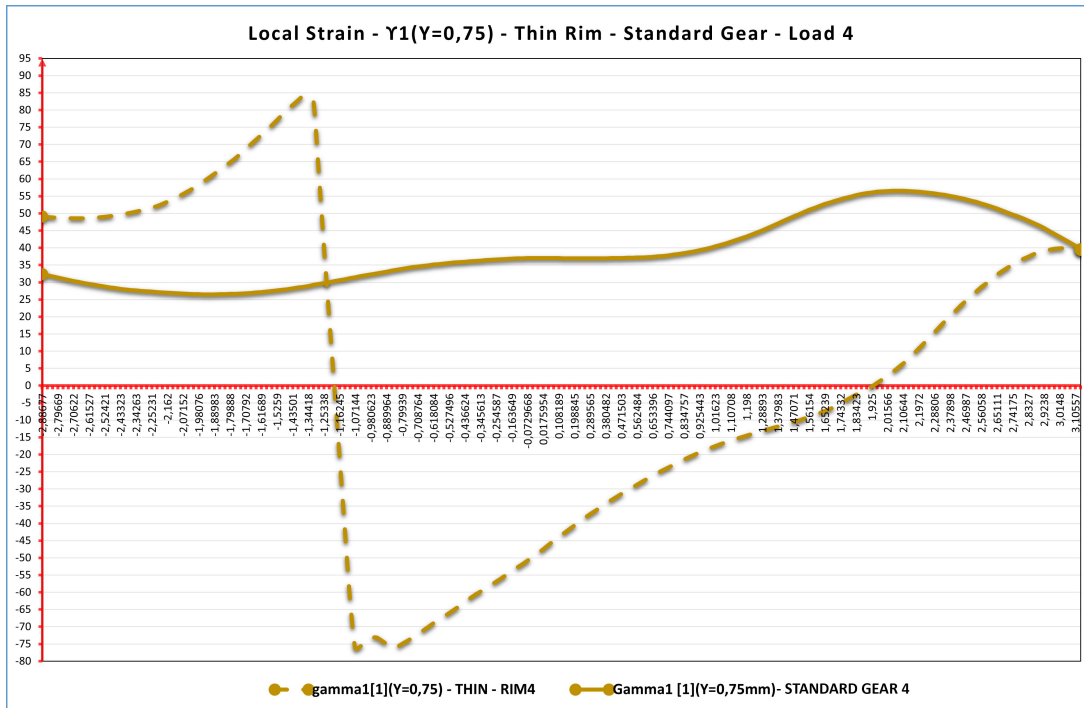


Figure 3.33: Local Strain - $\gamma_1(Y=0,75 \text{ mm})$ - Thin Rim - Standard Gear - Load 4

3.5.6. Local strain maps $L_1(X = 0)$

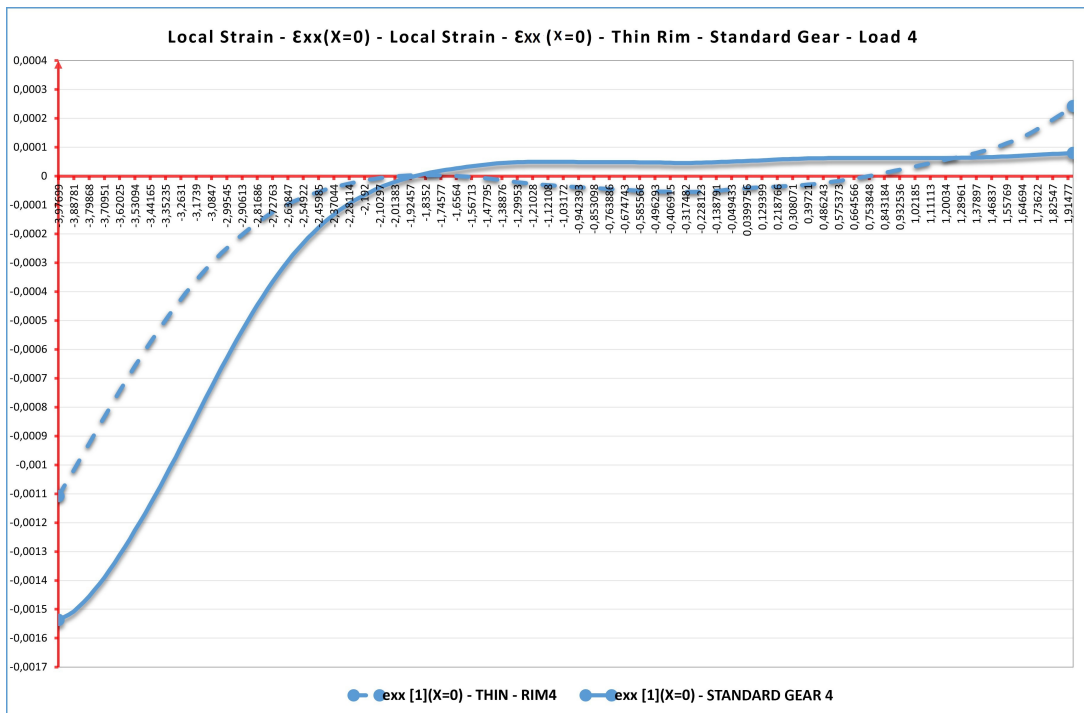
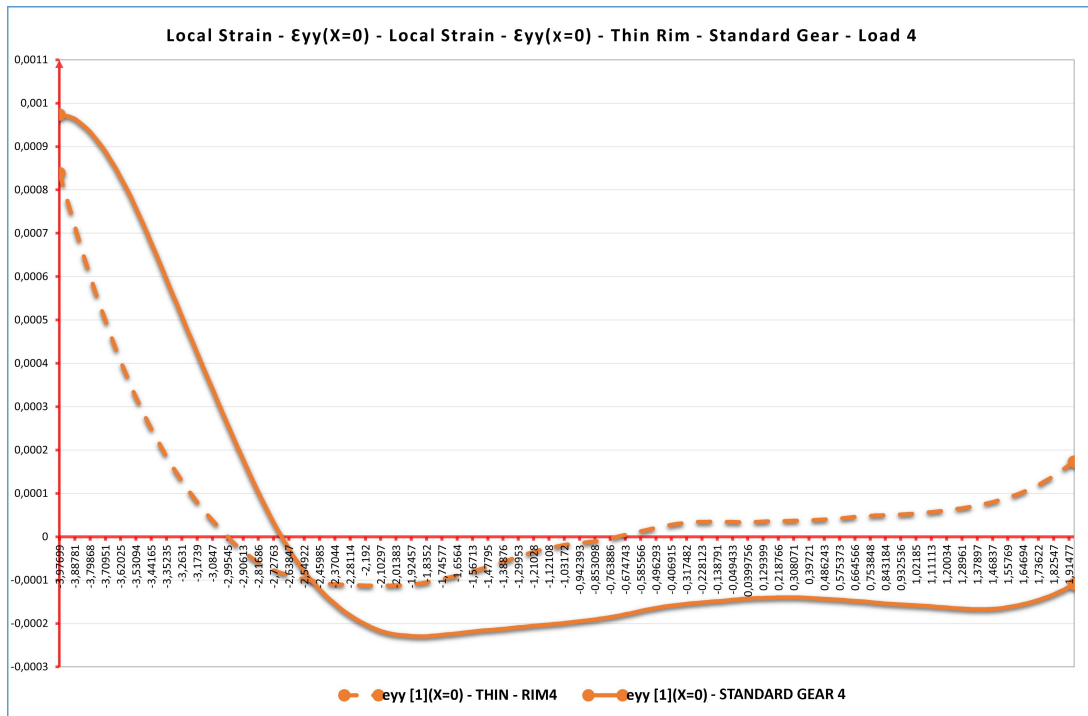


Figure 3.34: Local Strain - $\epsilon_{xx}(X=0 \text{ mm})$ - Local Strain - $\epsilon_{xx}(X=0 \text{ mm})$ Thin Rim - Standard Gear - Load 4

In the figure 3.34, a decrease in the exx stress along the wheel axis can be observed, with a nearly negligible trend as one moves towards the center of the wheels. A peak can be observed at the addendum of the wheels in compression only when different loads are applied.



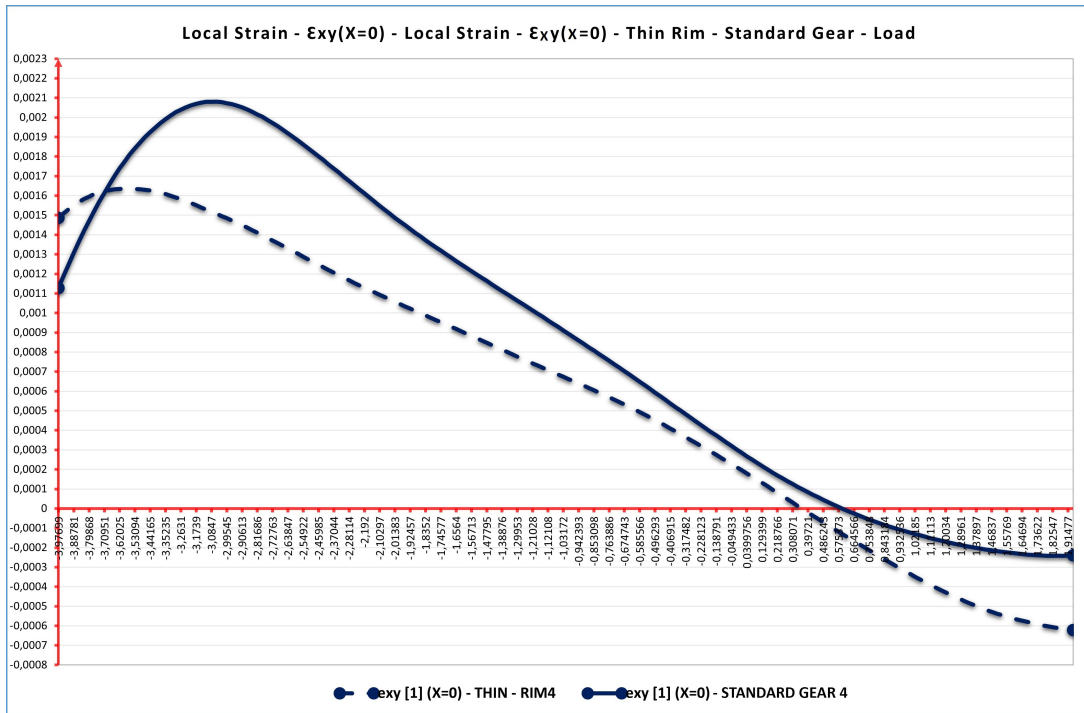
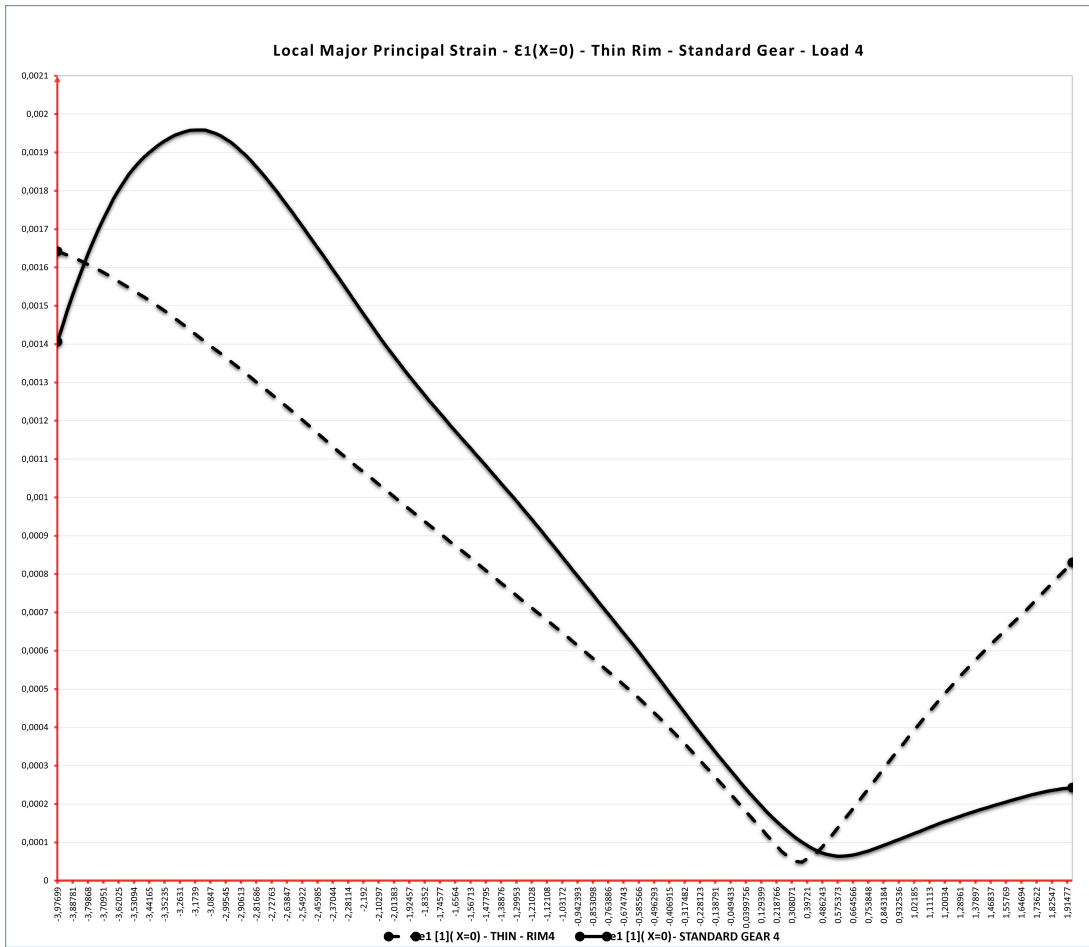


Figure 3.36: Local Strain - $\epsilon_{xy}(X=0 \text{ mm})$ - Local Strain - $\epsilon_{xy}(X=0 \text{ mm})$ Thin Rim - Standard Gear - Load 4



4 | Conclusions and future developments

In this work, experimental activities were conducted to investigate the bending behavior of standard gears, thin-rim gears, shot-peened gears and non-shot-peened gears. The thesis aims to validate the Digital Image Correlation (DIC) technique for material behavior characterization. The objective is to find a non-destructive technique for accurately determining the maximum value of RS (Residual Stress) of some gears provided by CRF. A Digital Image Correlation (DIC) technique was employed, involving the analysis of images of the gear's surface to obtain strain maps. The primary focus of the study was to comprehend how specific geometry parameters, such as rim and web, impact the position of the most stress point at the tooth root zone. Nevertheless, local strain maps were successfully obtained in standard and thin-rim gears, effectively characterizing the stress field near the tooth root.

Regrettably, the results of Shot-peened and Non-shot peened gears are not included in this study due to an experimental error. The gears accidentally moved while applying the loads, leading to unreliable data. As a result, these gears had to be excluded from the analysis. In the near future, two punches will be created on which to mount the gears to prevent their rotation during the application of high loads.

In conclusion, the DIC technique proved to be a valuable tool for studying complex mechanical components like lightweight gears. The careful calibration of the instrumentation and proper tuning of the loading system allowed for the acquisition of valuable information. This technique can assist designers in understanding stress distribution and predicting failure points, which are essential for optimizing gear design and ensuring reliability and safety.

Bibliography

- [1] Digital image correlation: Overview of principles and software by university of south carolina - correlated solutions inc. 2009.
- [2] Calculation of load capacity of spur and helical gears, part 1, 2019.
- [3] Calculation of load capacity of spur and helical gears, part 3, 2019.
- [4] D. Breuer and B. Matlock. Adaptation of shot peen parameters for gear geometry. In *11th International conference on shot peening (ICSP-11), South Bend*, pages 447–452, 2011.
- [5] E. Conrado, P. Davoli, et al. The “true” bending stress in spur gears. *Gear Technology*, 8:52–57, 2007.
- [6] F. Curà, A. Mura, L. Corsaro, and A. Revilla. Dic analysis of gears in bending condition. In *IOP Conference Series: Materials Science and Engineering*, volume 1275, page 012038. IOP Publishing, 2023.
- [7] A. Freddi, G. Olmi, and L. Cristofolini. Experimental stress analysis for materials and structures. *Stress analysis models for developing design methodologies. Series in solid and structural mechanics*, 1, 2015.
- [8] M. D. Lawrenz. Shot peening and its effect on gearing. Technical report, SAE Technical Paper, 1984.
- [9] D. G. Lewicki and R. Ballarini. Effect of rim thickness on gear crack propagation path. 1997.
- [10] D. V. Nelson. Residual stress determination using full-field optical methods. *Journal of Physics: Photonics*, 3(4):044003, 2021.
- [11] G. Niemann and H. Winter. *Maschineelement*, vol. 2, 1989.
- [12] J.-J. Orteu. 3-d computer vision in experimental mechanics. *Optics and lasers in engineering*, 47(3-4):282–291, 2009.

- [13] M. Palanca. Ottimizzazione dei parametri di acquisizione ed elaborazione per l'analisi di segmenti ossei tramite correlazione di immagini digitali.
- [14] B. Pan. Digital image correlation for surface deformation measurement: historical developments, recent advances and future goals. *Measurement Science and Technology*, 29(8):082001, 2018.
- [15] B. Pan, K. Qian, H. Xie, and A. Asundi. Two-dimensional digital image correlation for in-plane displacement and strain measurement: a review. *Measurement science and technology*, 20(6):062001, 2009.
- [16] B. Pan, J. Yuan, and Y. Xia. Strain field denoising for digital image correlation using a regularized cost-function. *Optics and Lasers in Engineering*, 65:9–17, 2015.
- [17] L. Y. PI, L. Smith, M. A. Gotheekar, and M. X. Chen. Measure strain distribution using digital image correlation (dic) for tensile tests. *Oakland University*, 2010.
- [18] W. N. Sharpe. *Springer handbook of experimental solid mechanics*. Springer Science & Business Media, 2008.
- [19] C. Solutions. Application note an-1701 speckle pattern fundamentals. *Speckle Pattern Fundam*, pages 1–13, 2017.
- [20] C. Solutions. Vic-3d software manual, version 9.2, 2022.
- [21] Y. Wang, J. Jiang, C. Wanintrudal, C. Du, D. Zhou, L. M. Smith, and L. Yang. Whole field sheet-metal tensile test using digital image correlation. *Experimental Techniques*, 34(2):54–59, 2010.

A | Appendix A

A.1. Experimental Results and Discussion

A.2. Standard Gear - Load 1

A.2.1. Local strain maps ϵ_{xx}

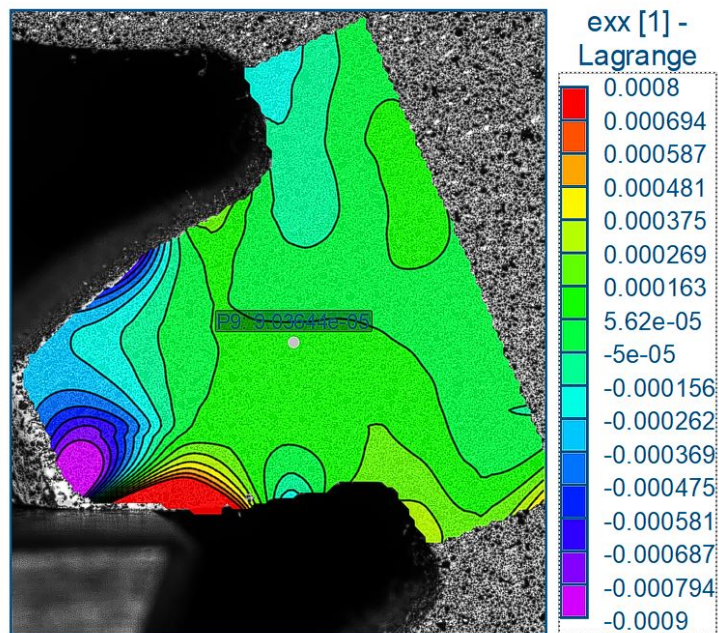
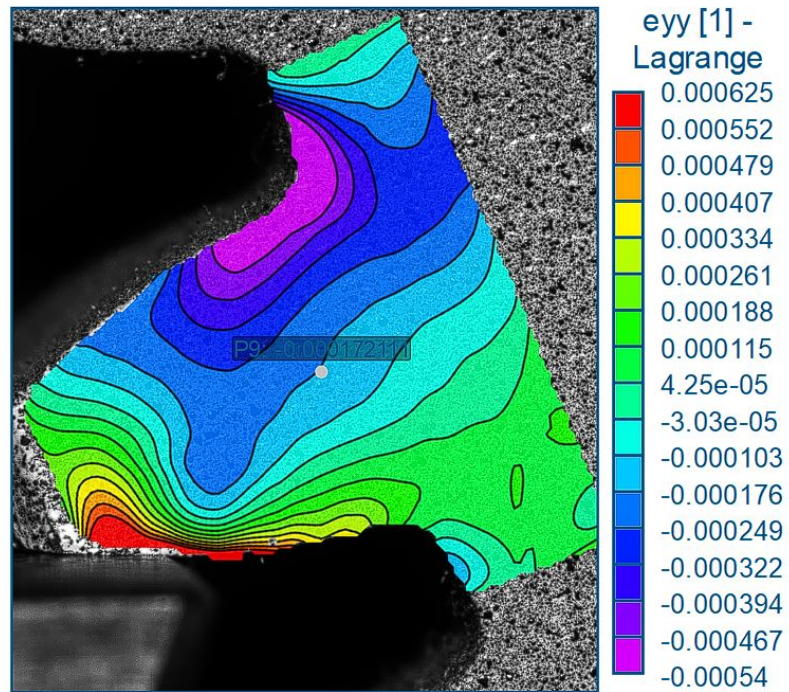
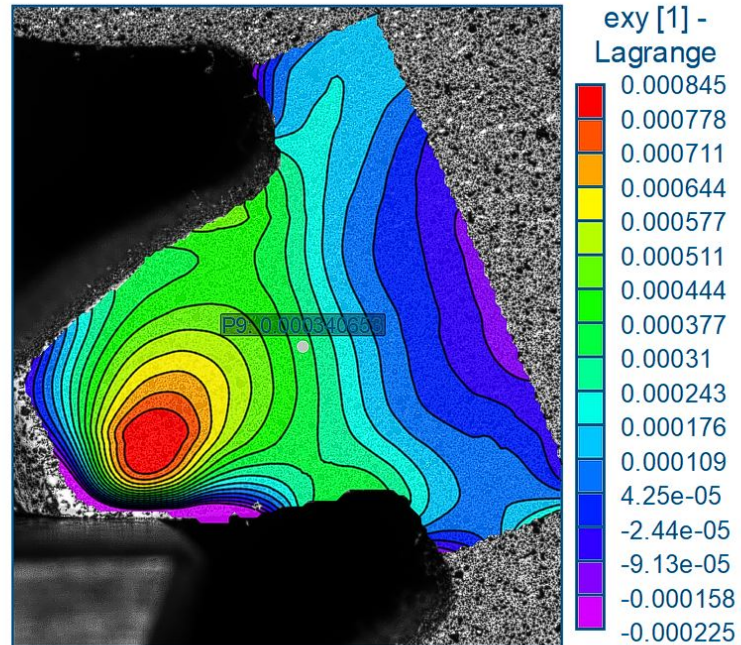
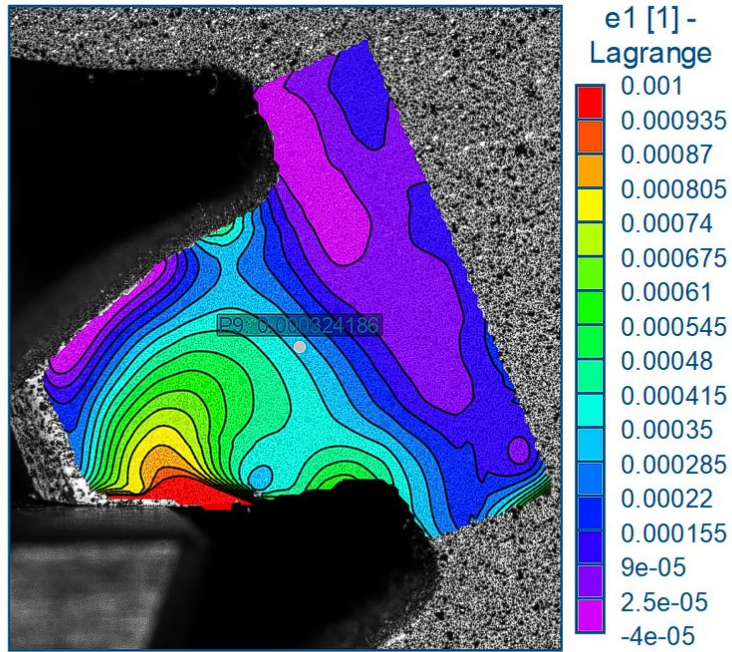
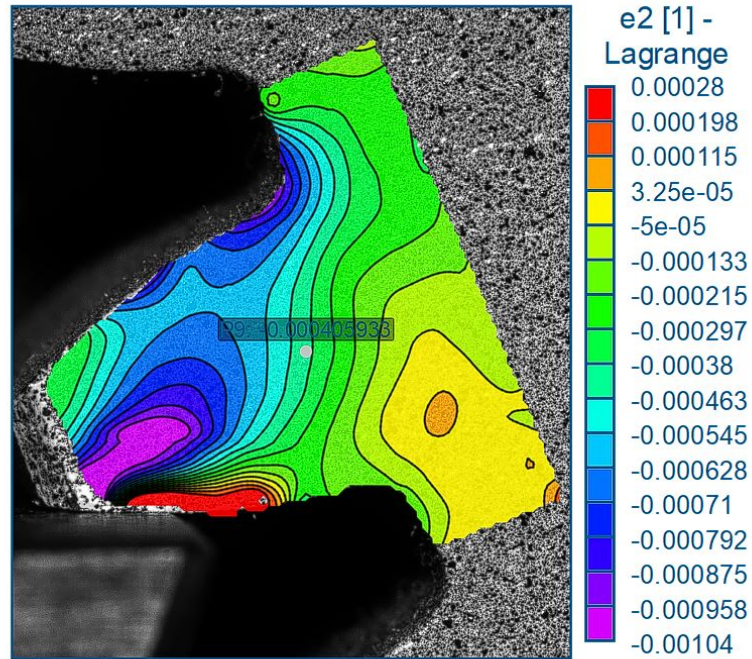


Figure A.1: Standard gear: local strain in the X-direction map ϵ_{xx} - Load 1

A.2.2. Local strain maps ϵ_{yy} Figure A.2: Standard gear: local strain in the Y-direction map ϵ_{yy} - Load 1

A.2.3. Local strain maps ϵ_{xy} Figure A.3: Standard gear: local shear strain map ϵ_{xy} - Load 1

A.2.4. Local strain maps ϵ_1 Figure A.4: Standard gear: major principal strain map ϵ_1 - Load 1

A.2.5. Local strain maps ϵ_2 Figure A.5: Standard gear: minor principal strain map ϵ_2 - Load 1

A.2.6. Local strain maps γ_1

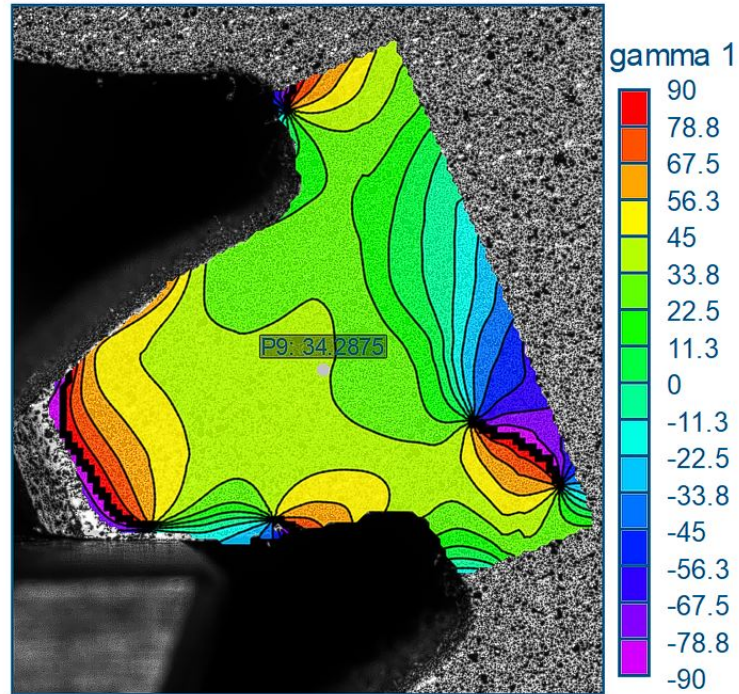
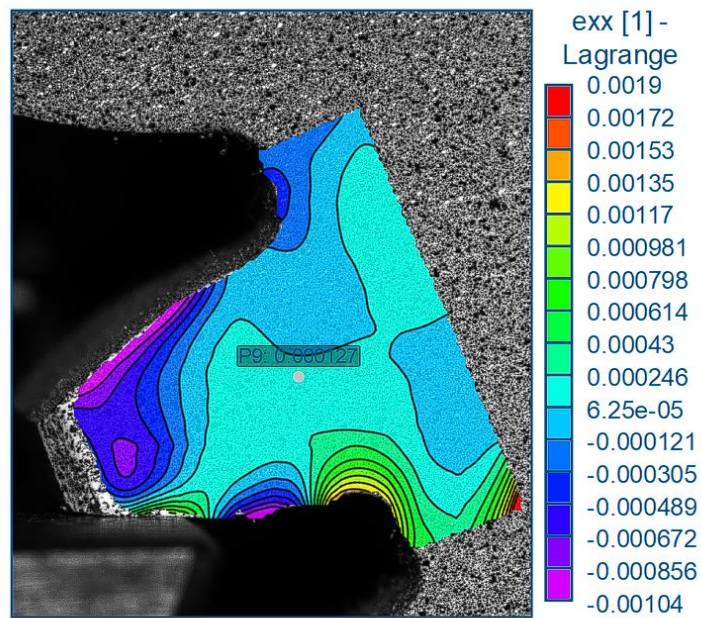
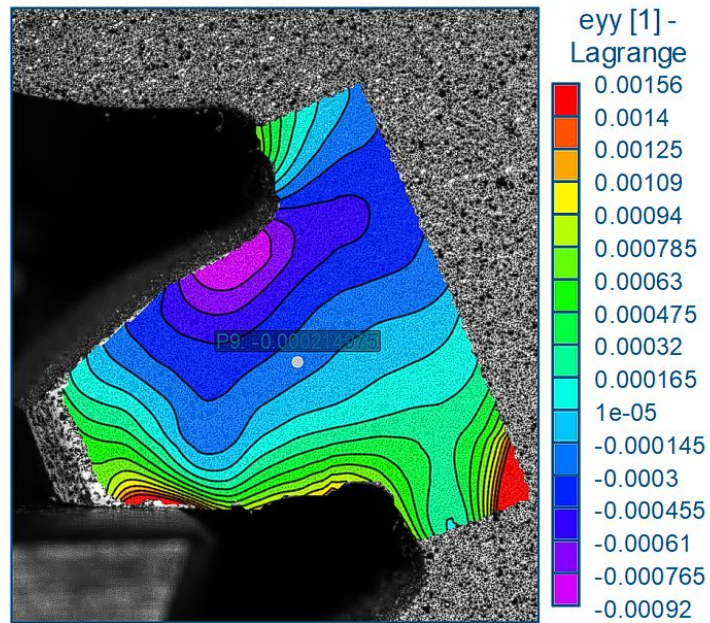
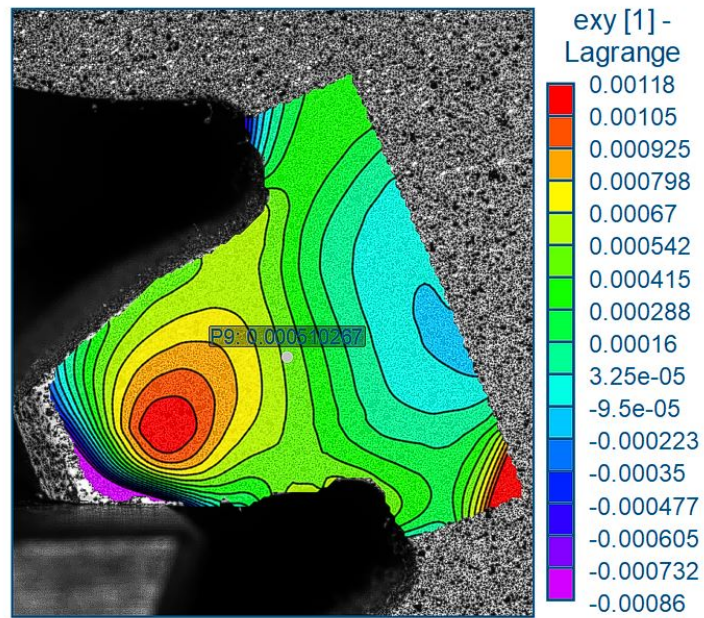


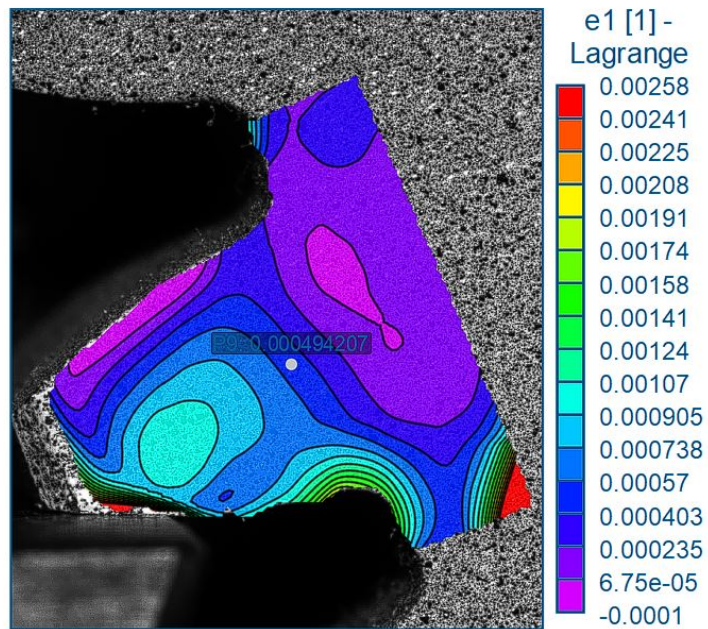
Figure A.6: Standard gear: principal strain angle map γ_1 - Load 1

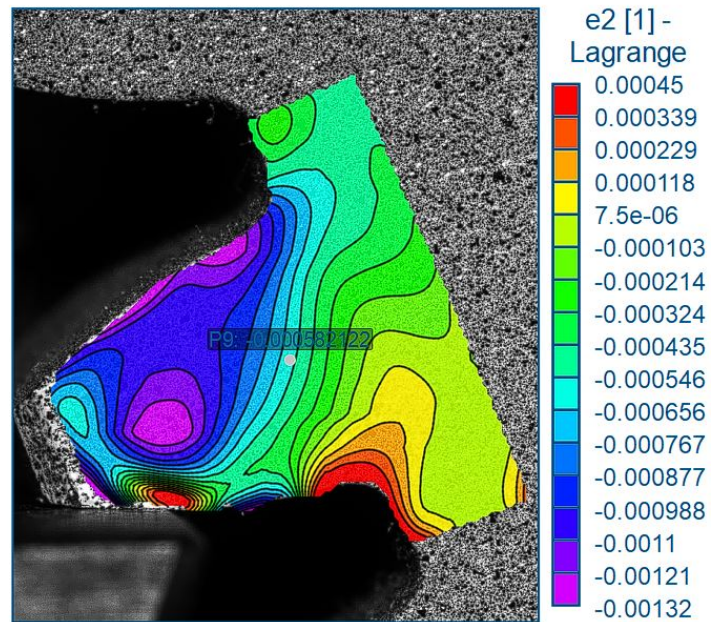
A.3. Standard gear - Load 2

A.3.1. Local strain maps ϵ_{xx} Figure A.7: Standard gear: local strain in the X-direction map ϵ_{xx} - Load 2

A.3.2. Local strain maps ϵ_{yy} Figure A.8: Standard gear: local strain in the Y-direction map ϵ_{yy} - Load 2

A.3.3. Local strain maps ϵ_{xy} Figure A.9: Standard gear: local shear strain map ϵ_{xy} - Load 2

A.3.4. Local strain maps ϵ_1 Figure A.10: Standard gear: major principal strain map ϵ_1 - Load 2

A.3.5. Local strain maps ϵ_2 Figure A.11: Standard gear: minor principal strain map ϵ_2 - Load 2

A.3.6. Local strain maps γ_1

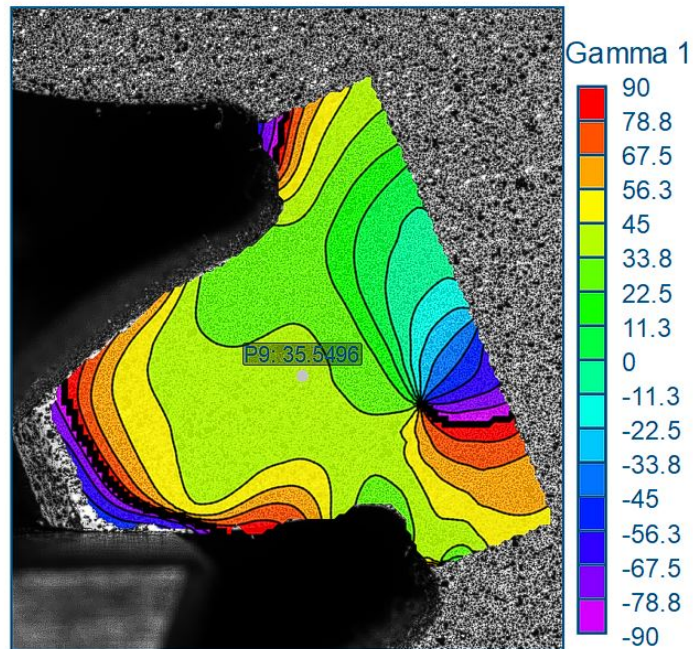
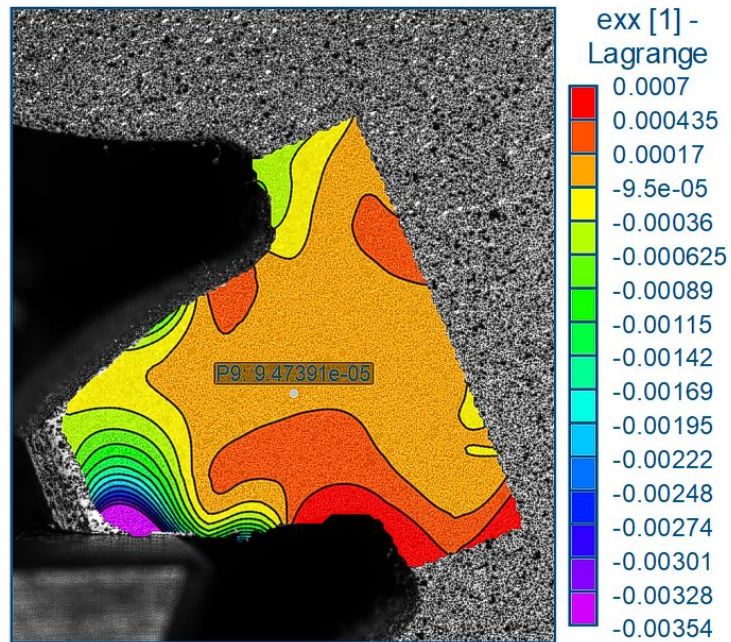


Figure A.12: Standard gear: principal strain angle map γ_1 - Load 2

A.4. Standard Gear - Load 3

A.4.1. Local strain maps ϵ_{xx} Figure A.13: Standard gear: local strain in the X-direction map ϵ_{xx} - Load 3

A.4.2. Local strain maps ϵ_{yy}

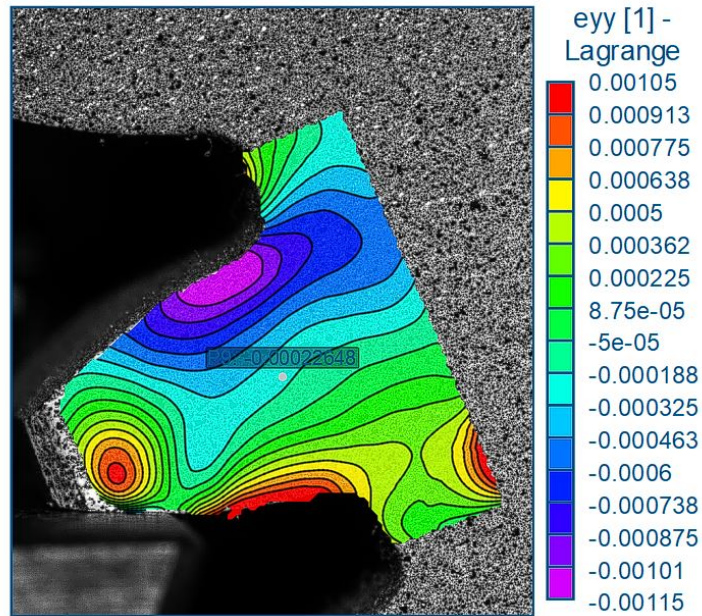
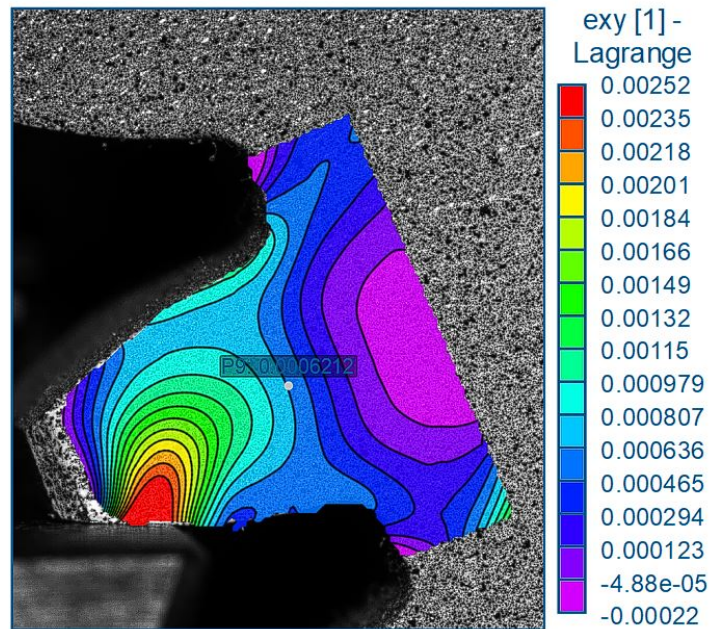
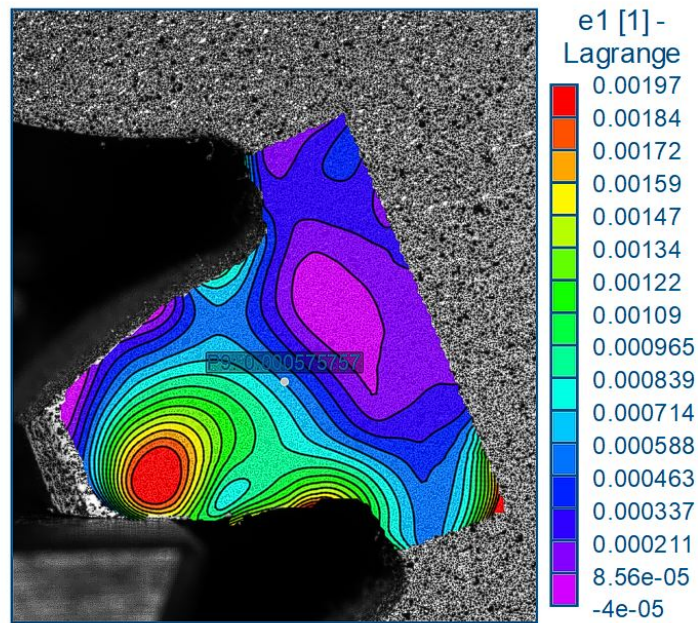
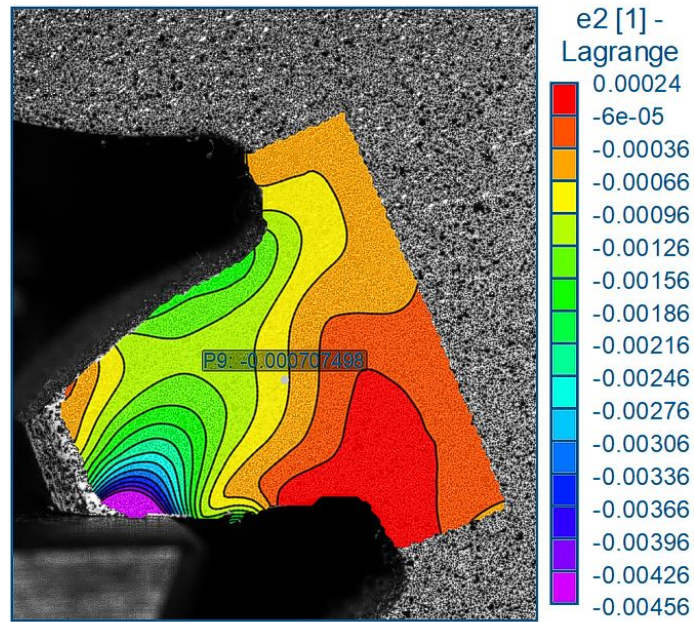


Figure A.14: Standard gear: local strain in the Y-direction map ϵ_{yy} - Load 3

A.4.3. Local strain maps ϵ_{xy} Figure A.15: Standard gear: local shear strain map ϵ_{xy} - Load 3

A.4.4. Local strain maps ϵ_1 Figure A.16: Standard gear: major principal strain map ϵ_1 - Load 3

A.4.5. Local strain maps ϵ_2 Figure A.17: Standard gear: minor principal strain map ϵ_2 - Load 3

A.4.6. Local strain maps γ_1

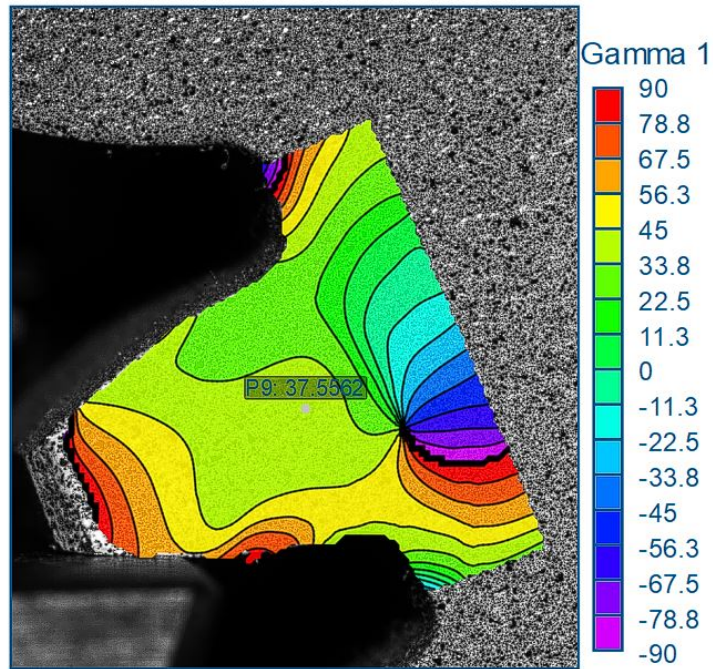
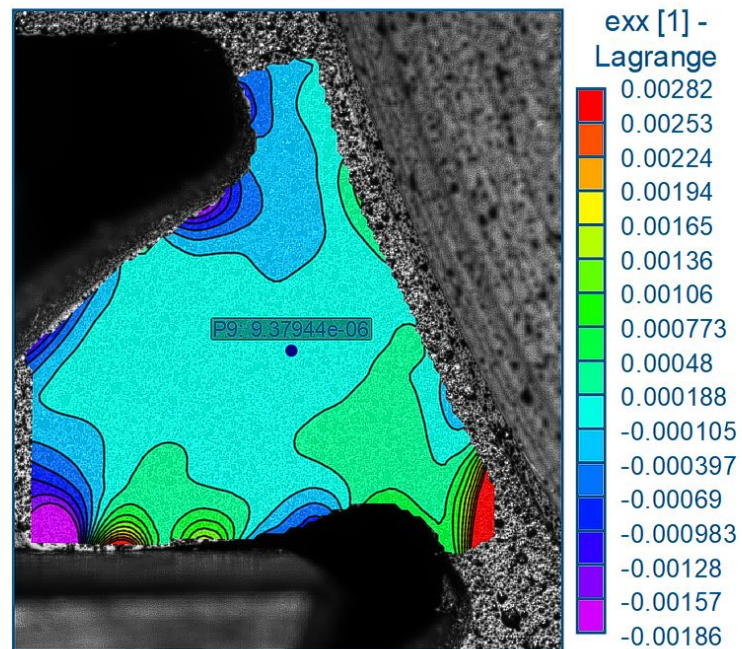
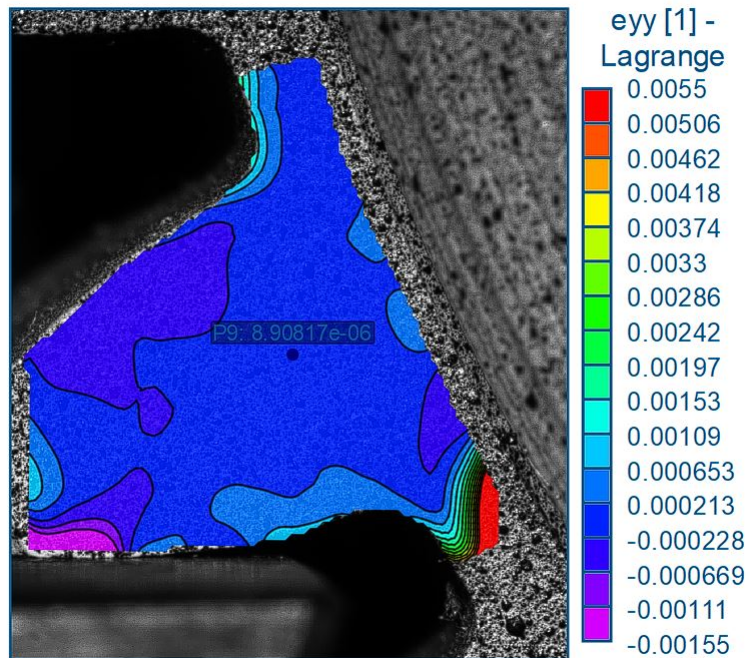


Figure A.18: Standard gear: principal strain angle map γ_1 - Load 3

A.5. Thin-Rim- Gear - Load 1

A.5.1. Local strain maps ϵ_{xx} Figure A.19: Thin-rim gear: local strain in the X-direction map ϵ_{xx} - Load 1

A.5.2. Local strain maps ϵ_{yy} Figure A.20: Thin-rim gear: local strain in the Y-direction map ϵ_{yy} - Load 1

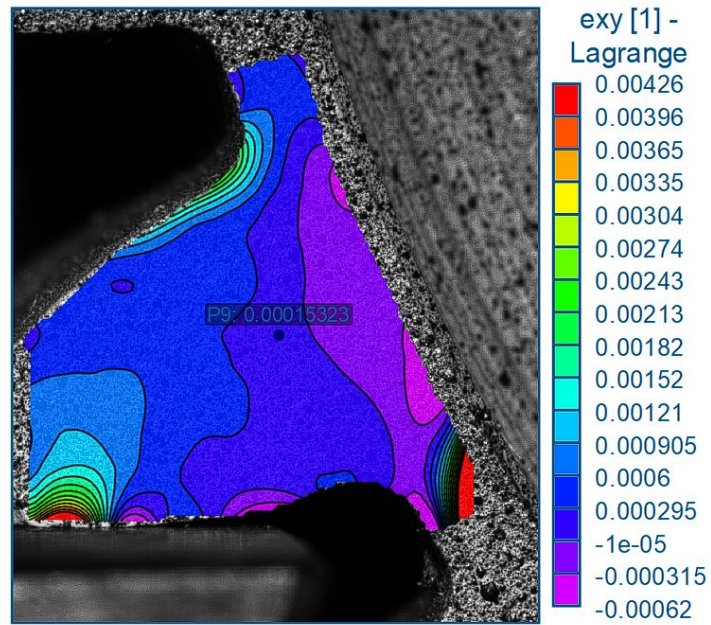
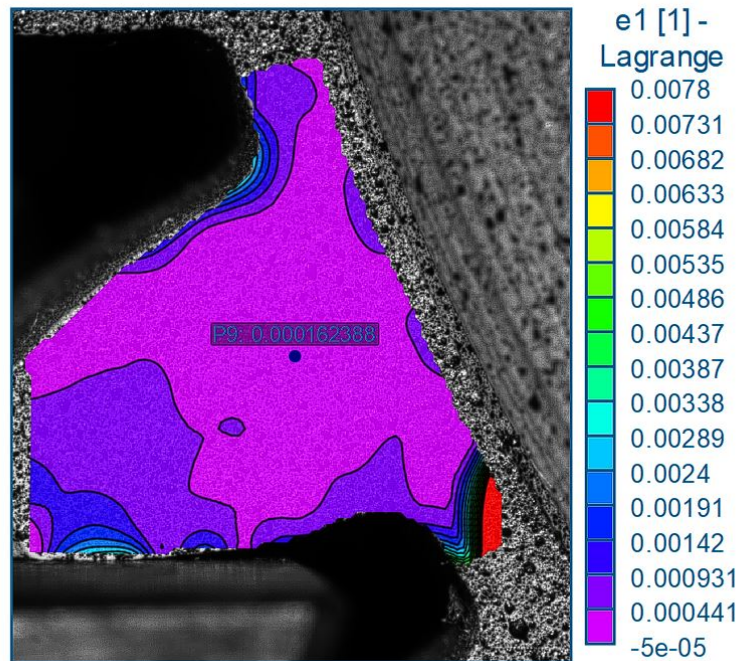
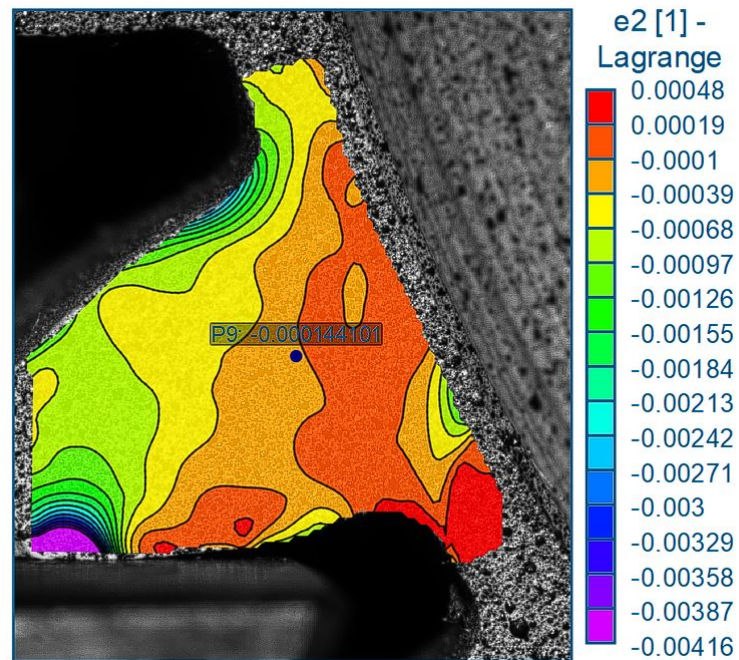
A.5.3. Local strain maps ϵ_{xy} 

Figure A.21: Thin-rim gear: local shear strain map ϵ_{xy} - Load 1

A.5.4. Local strain maps ϵ_1 Figure A.22: Thin-rim gear: major principal strain map ϵ_1 - Load 1

A.5.5. Local strain maps ϵ_2 Figure A.23: Thin-rim gear: minor principal strain map ϵ_2 - Load 1

A.5.6. Local strain maps γ_1

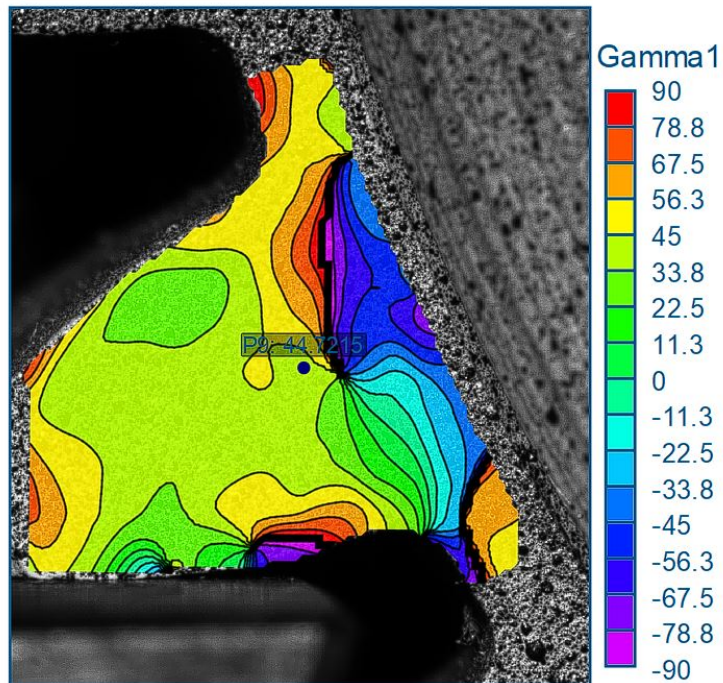
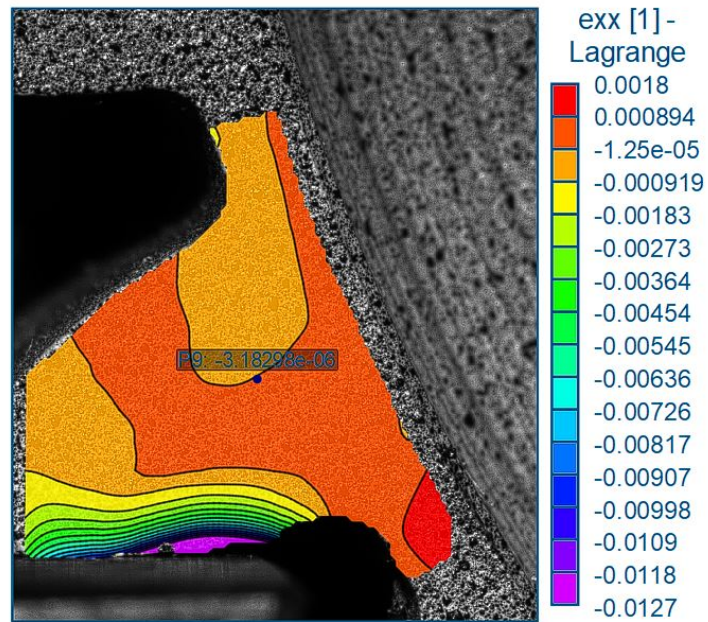


Figure A.24: Thin-rim gear: principal strain angle map γ_1 - Load 1

A.6. Thin-rim Gear - Load 2

A.6.1. Local strain maps ϵ_{xx} Figure A.25: Thin-rim gear: local strain in the X-direction map ϵ_{xx} - Load 2

A.6.2. Local strain maps ϵ_{yy}

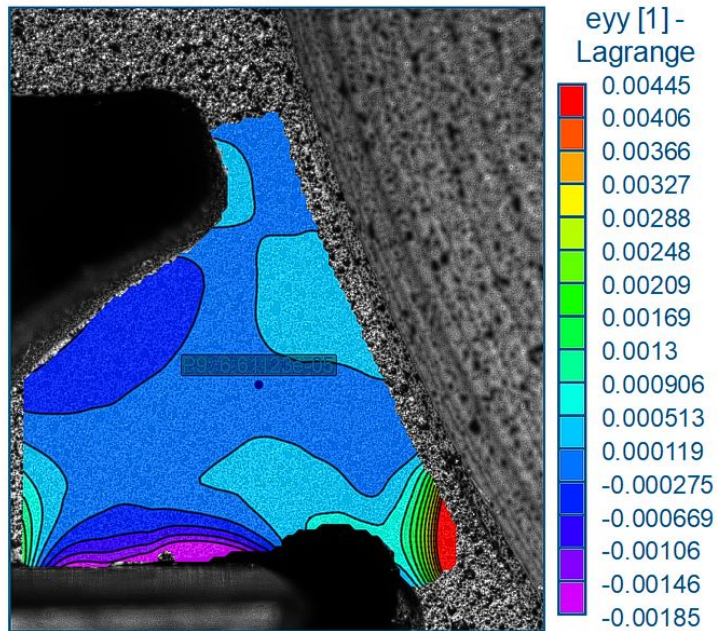
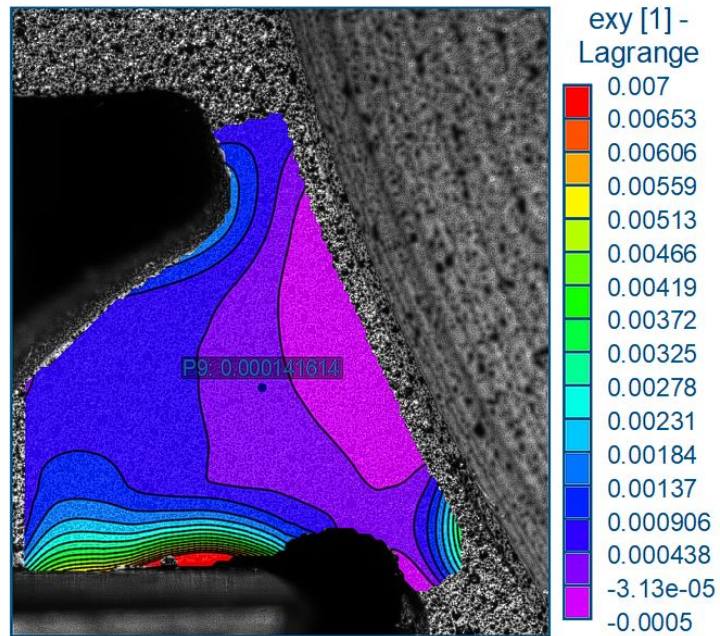
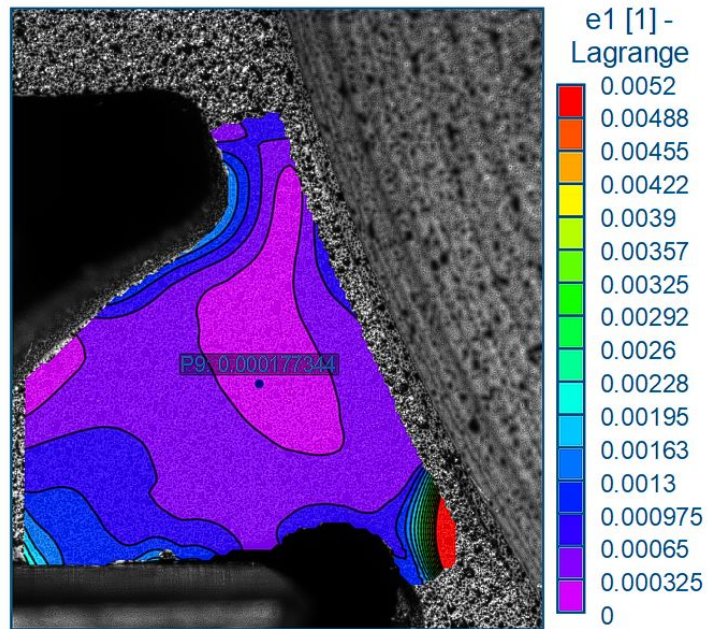
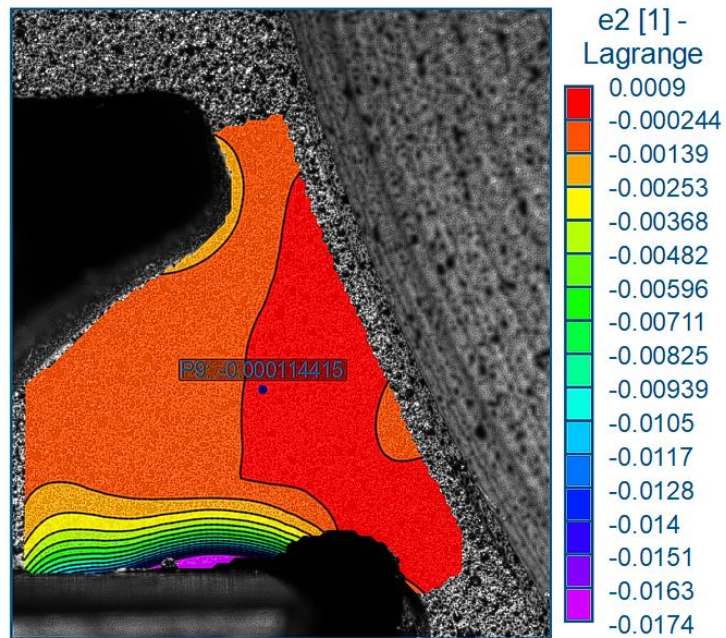


Figure A.26: Thin-rim gear: local strain in the Y-direction map ϵ_{yy} - Load 2

A.6.3. Local strain maps ϵ_{xy} Figure A.27: Thin-rim gear: local shear strain map ϵ_{xy} - Load 2

A.6.4. Local strain maps ϵ_1 Figure A.28: Thin-rim gear: major principal strain map ϵ_1 - Load 2

A.6.5. Local strain maps ϵ_2 Figure A.29: Thin-rim gear: minor principal strain map ϵ_2 - Load 2

A.6.6. Local strain maps γ_1

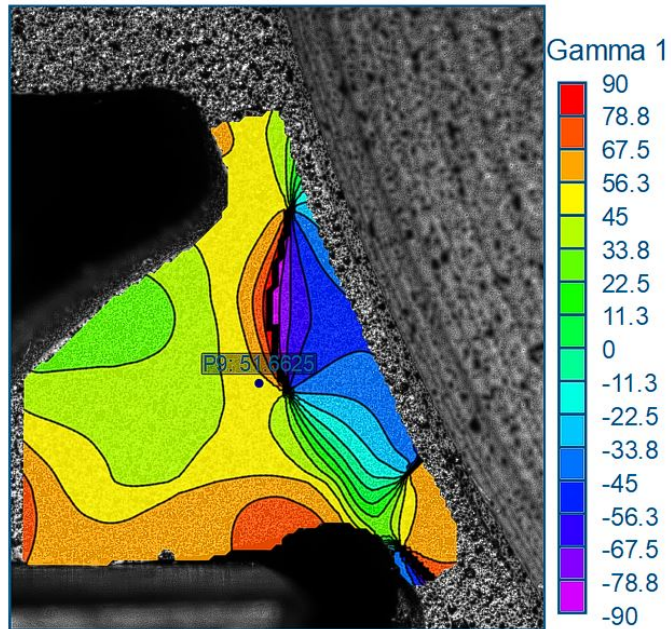
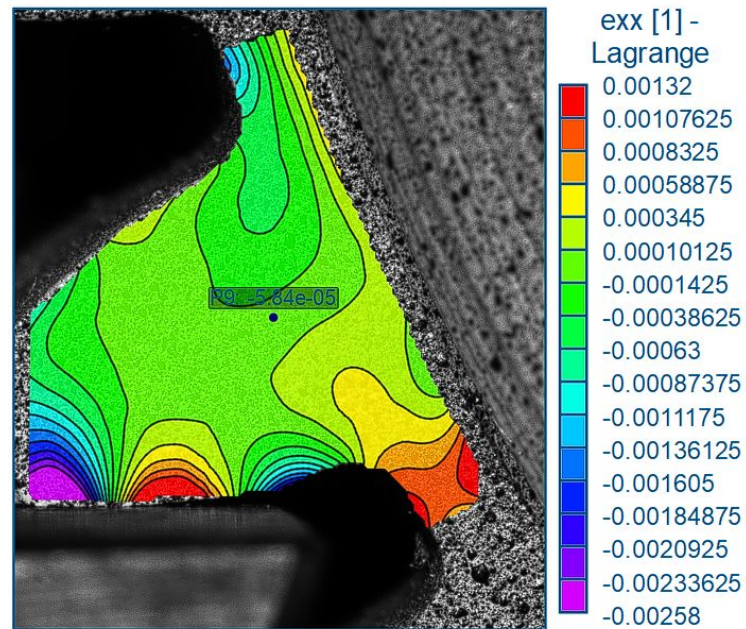
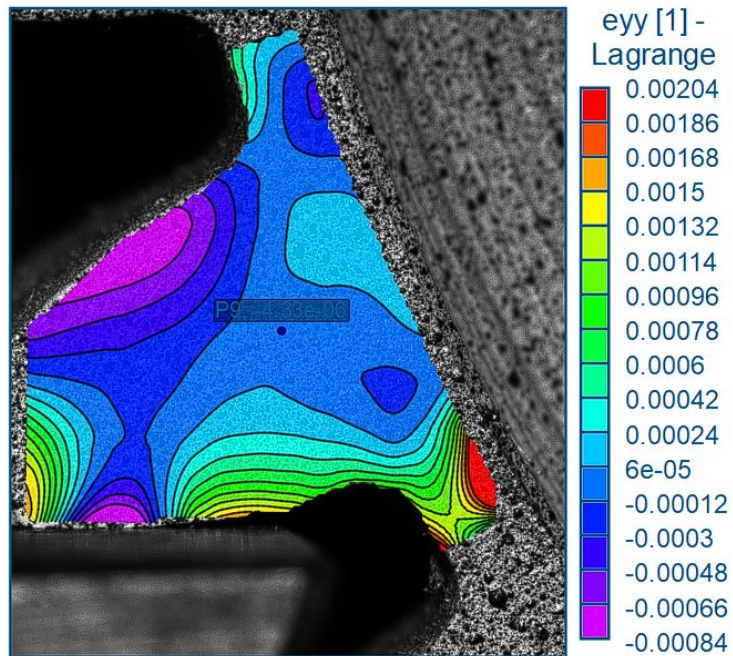
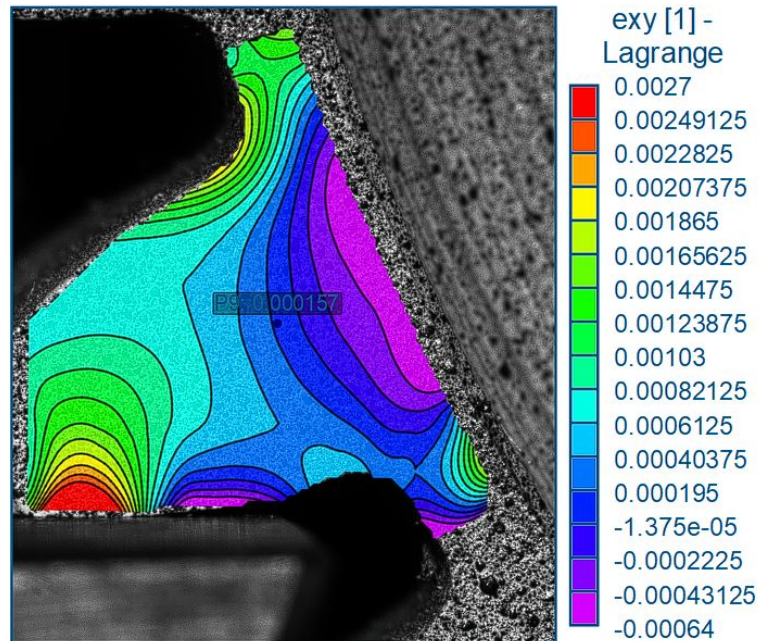


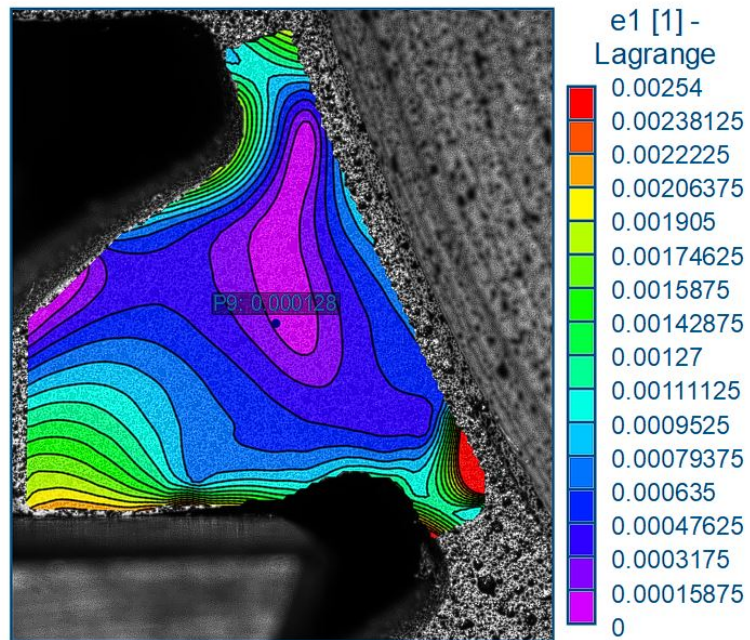
Figure A.30: Thin-rim gear: principal strain angle map γ_1 - Load 2

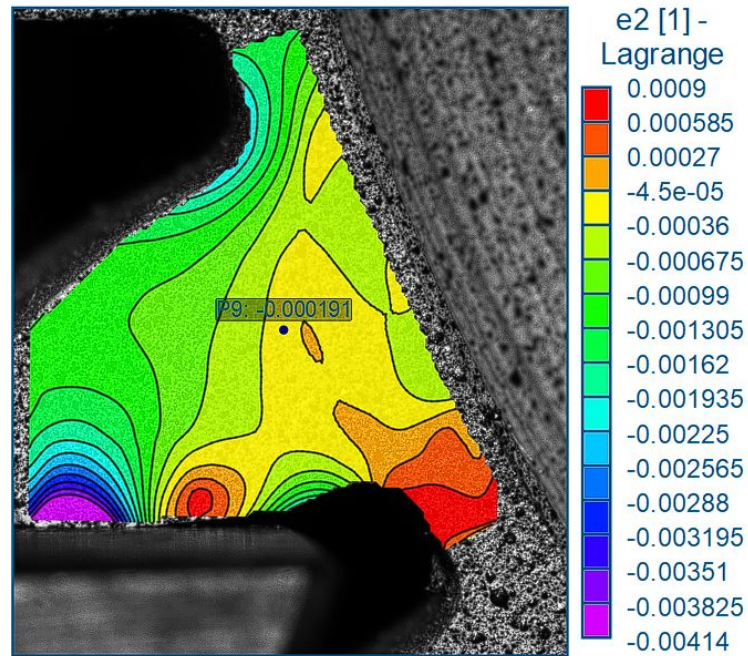
A.7. Thin-Rim Gear - Load 3

A.7.1. Local strain maps ϵ_{xx} Figure A.31: Thin-rim gear: local strain in the X-direction map ϵ_{xx} - Load 3

A.7.2. Local strain maps ϵ_{yy} Figure A.32: Thin-rim gear: local strain in the Y-direction map ϵ_{yy} - Load 3

A.7.3. Local strain maps ϵ_{xy} Figure A.33: Thin-rim gear: local shear strain map ϵ_{xy} - Load 3

A.7.4. Local strain maps ϵ_1 Figure A.34: Thin-rim gear: major principal strain map ϵ_1 - Load 3

A.7.5. Local strain maps ϵ_2 Figure A.35: Thin-rim gear: minor principal strain map ϵ_2 - Load 3

A.7.6. Local strain maps γ_1

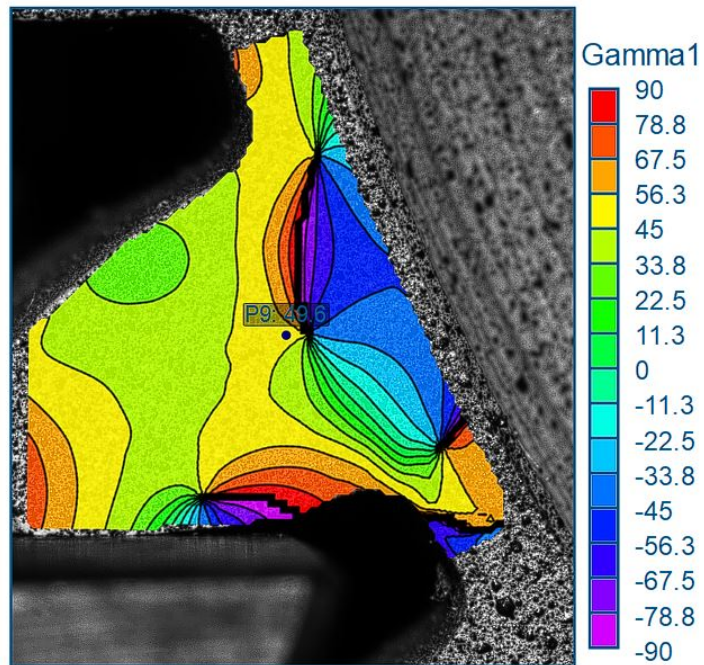
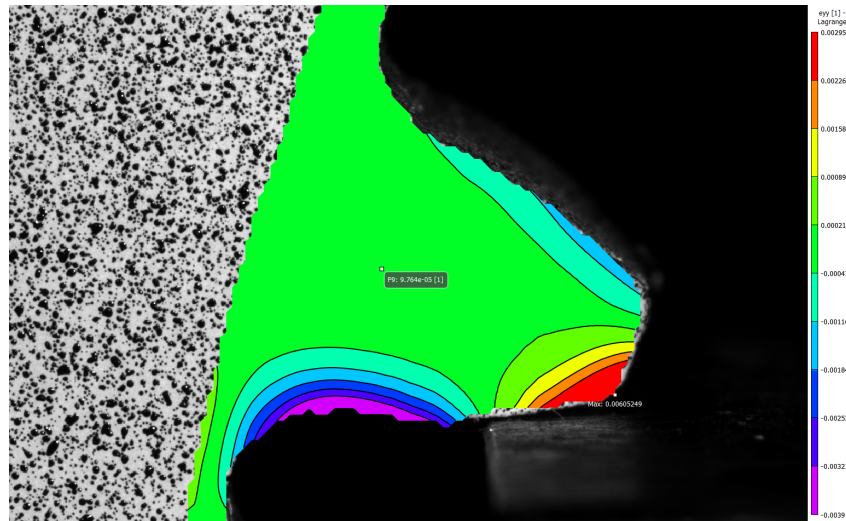
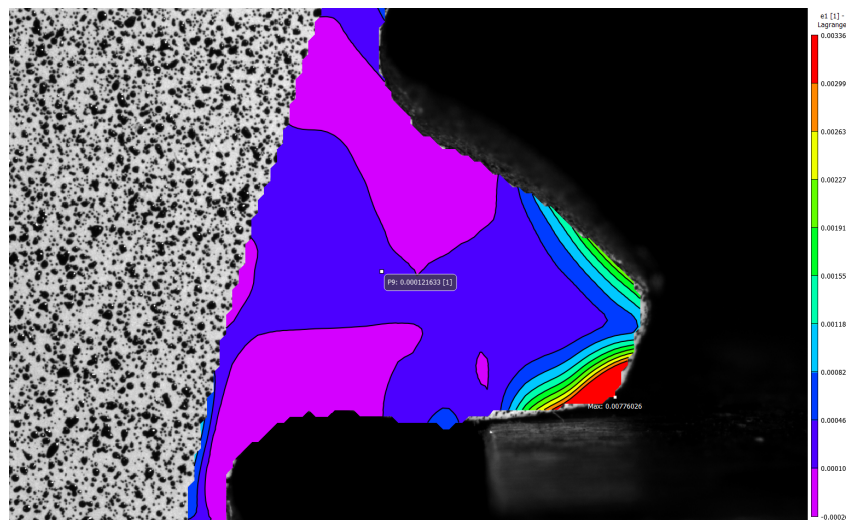


Figure A.36: Thin-rim gear: principal strain angle map γ_1 - Load 3

A.8. Shot-Peened Gear - Load 1

A.8.1. Local strain maps ϵ_{yy} Figure A.37: Shot-Peened Gear: local strain in the Y-direction map ϵ_{yy} - Load 1A.8.2. Local strain maps ϵ_1 Figure A.38: Shot-Peened Gear: major principal strain map ϵ_1 - Load 1

A.9.2. Local strain maps ϵ_1

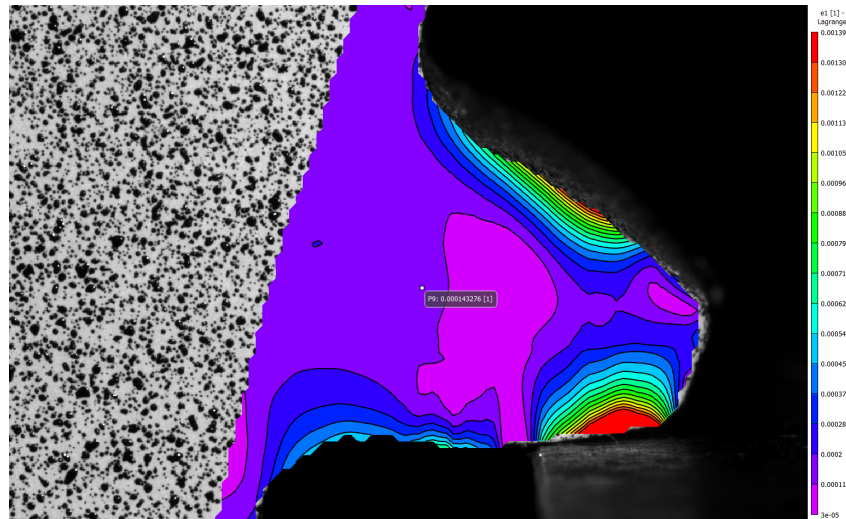


Figure A.41: Shot-Peened Gear: major principal strain map ϵ_1 - Load 2

A.9.3. Local strain maps γ_1

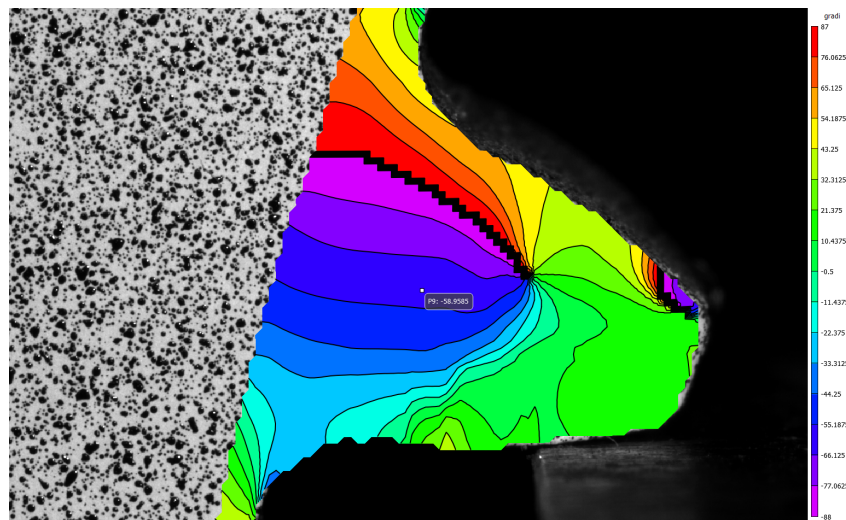


Figure A.42: Shot-Peened Gear: principal strain angle map γ_1 - Load 2

A.10. Non-Shot-Peened Gear - Load 1

A.10.1. Local strain maps ϵ_{yy}

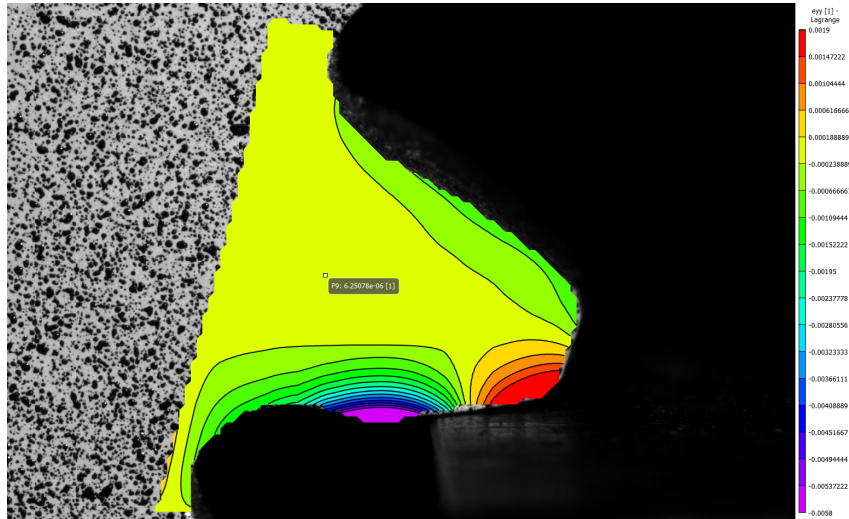


Figure A.43: Non-shot-peened gear:local strain in the Y-direction map ϵ_{yy} - Load 1

A.10.2. Local strain maps ϵ_1

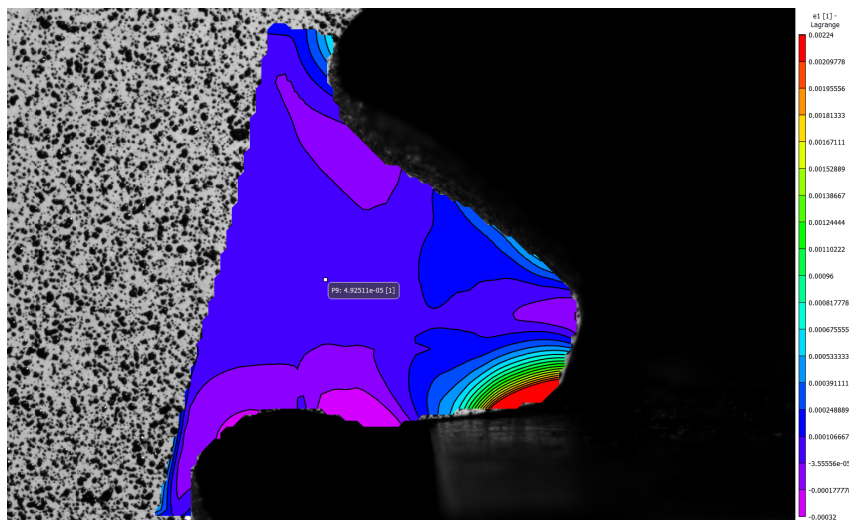


Figure A.44: Non-shot-peened gear:local strain in the Y-direction map ϵ_1 - Load 1

A.10.3. Local strain maps γ_1

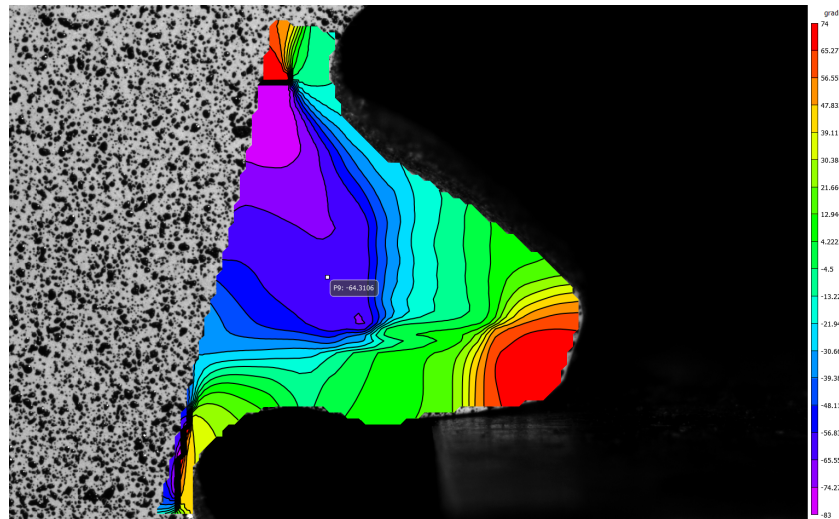


Figure A.45: Non-shot-peened gear:local strain in the Y-direction map γ_1 - Load 1

A.11. Non-Shot-Peened Gear - Load 2

A.11.1. Local strain maps ϵ_{yy}

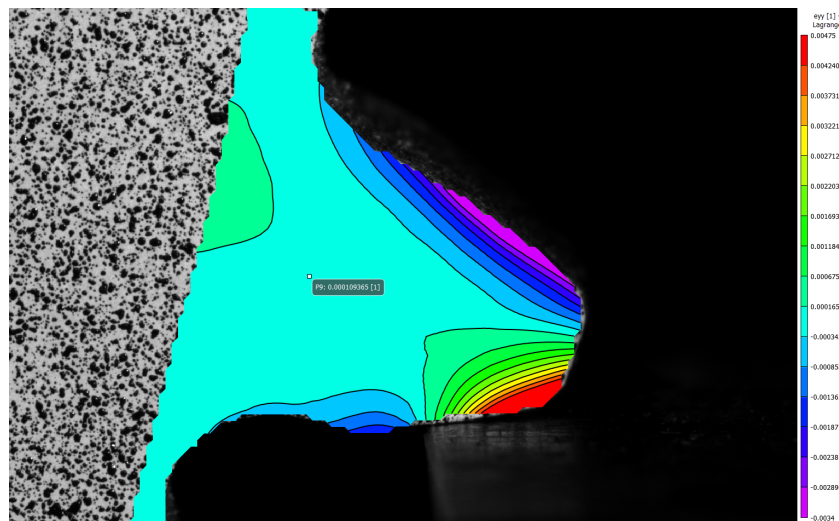


Figure A.46: Non-shot-peened gear:local strain in the Y-direction map ϵ_{yy} - Load 2

A.11.2. Local strain maps ϵ_1

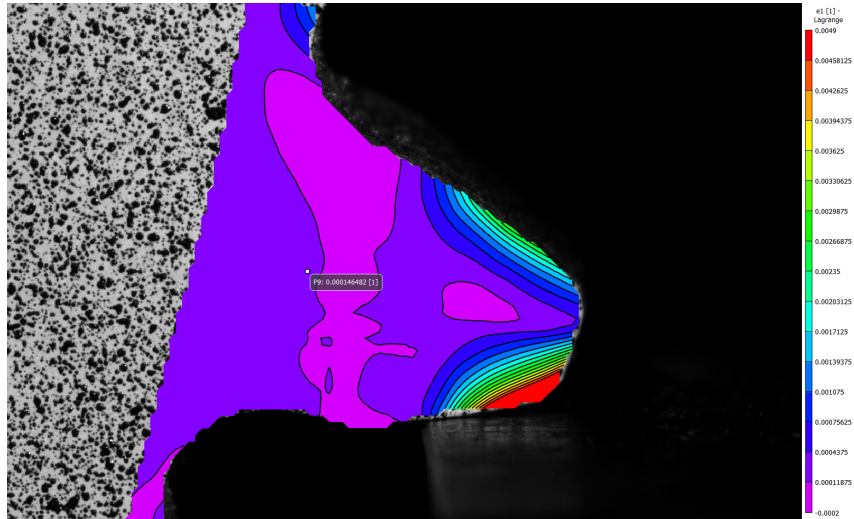


Figure A.47: Non-shot-peened gear:local strain in the Y-direction map ϵ_1 - Load 2

A.11.3. Local strain maps γ_1

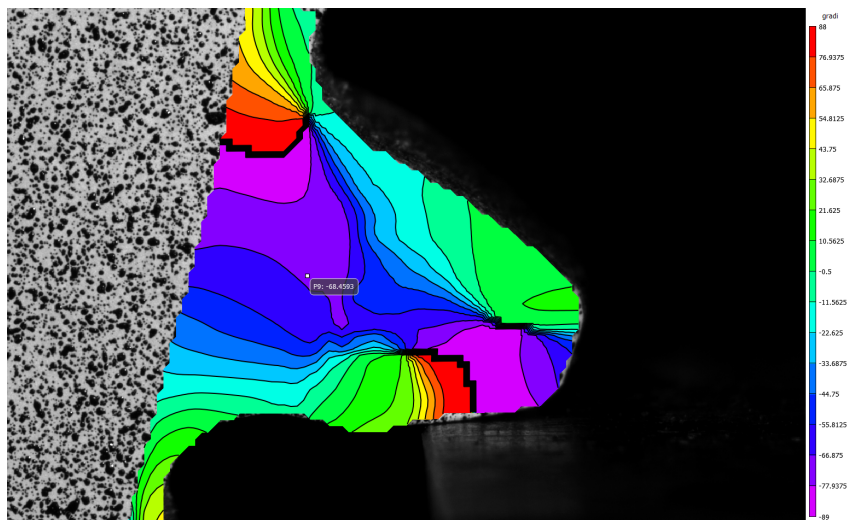


Figure A.48: Non-shot-peened gear:local strain in the Y-direction map γ_1 - Load 2

A.12. Load Analysis

A.13. Standard Gear - Load 3

A.13.1. Local strain maps ϵ_{xx}

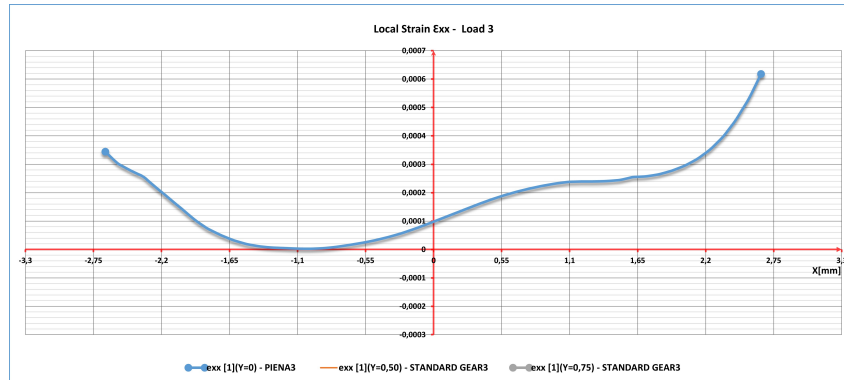


Figure A.49: Local strain ϵ_{xx} - Load 3

A.13.2. Local strain maps ϵ_{yy}

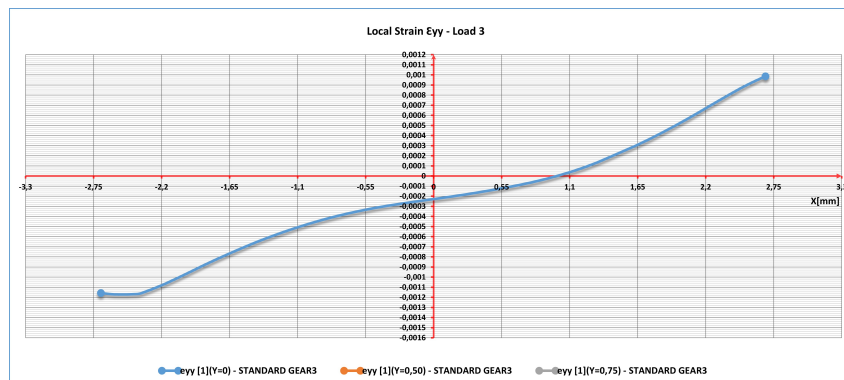


Figure A.50: Local strain ϵ_{yy} - Load 3

A.13.3. Local strain maps ϵ_{xy}

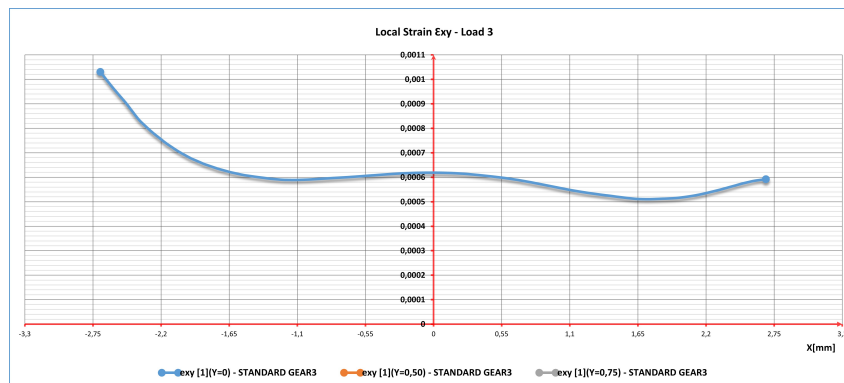


Figure A.51: Local strain ϵ_{xy} - Load 3

A.13.4. Local strain maps ϵ_1

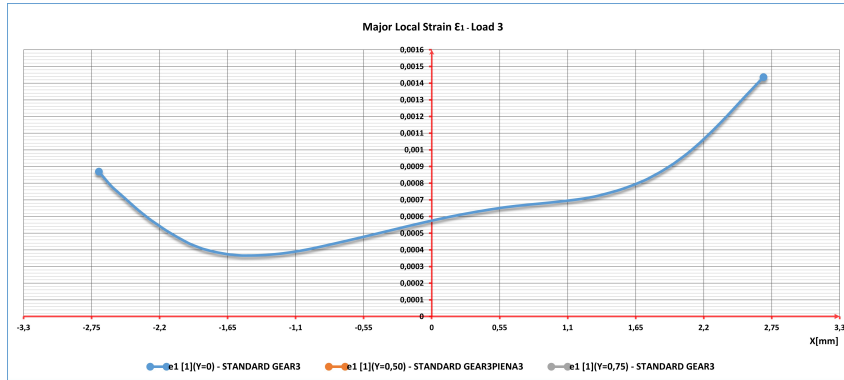


Figure A.52: major principal local strain ϵ_1 - Load 3

A.13.5. Local strain maps γ_1

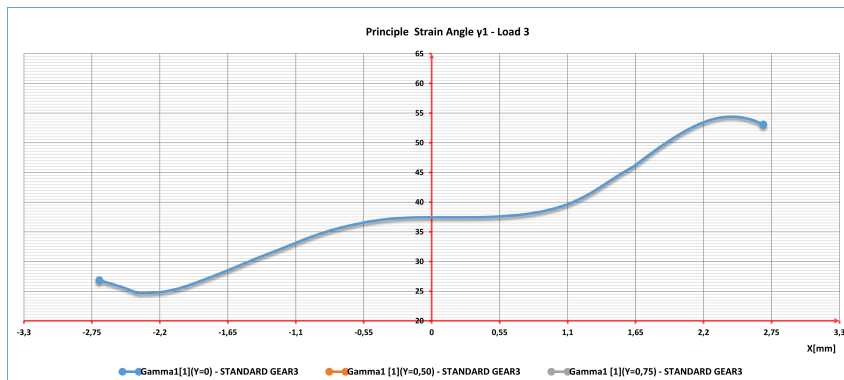


Figure A.53: Principal strain angle γ_1 - Load 3

A.13.6. Local strain maps $1(X = 0)$

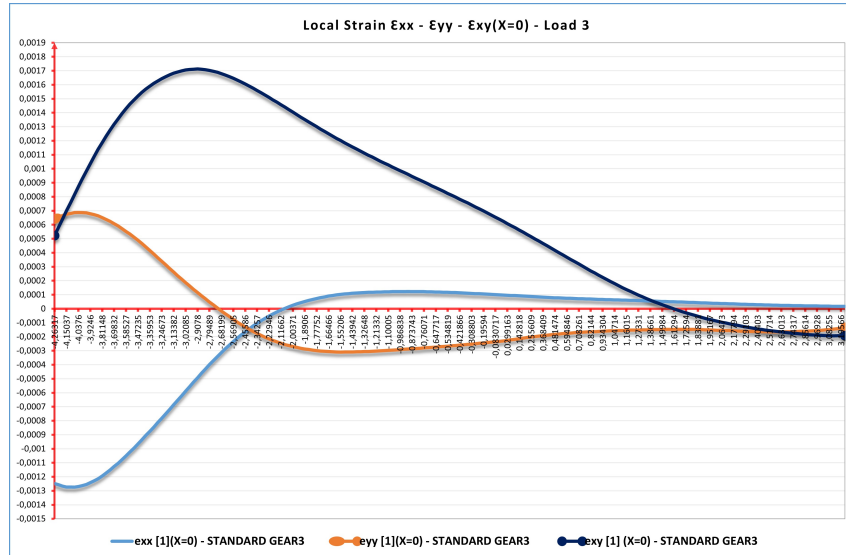


Figure A.54: Local Strain $\epsilon_{xx} - \epsilon_{yy} - \epsilon_{xy}(X=0)$ - Load 3

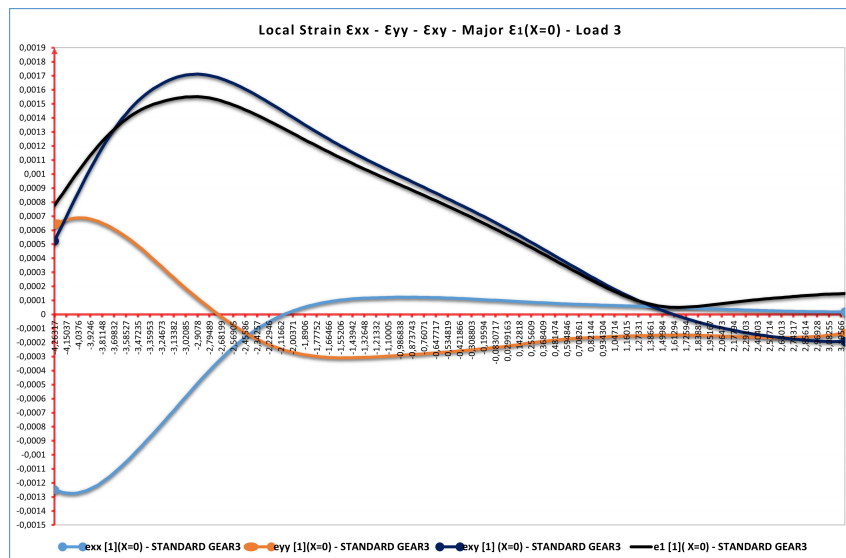


Figure A.55: Local Strain $\epsilon_{xx} - \epsilon_{yy} - \epsilon_{xy} - \text{Major } \epsilon_1(X=0)$ - Load 3

A.14. Standard Gear - Load 4

A.14.1. Local strain maps ϵ_{xx}

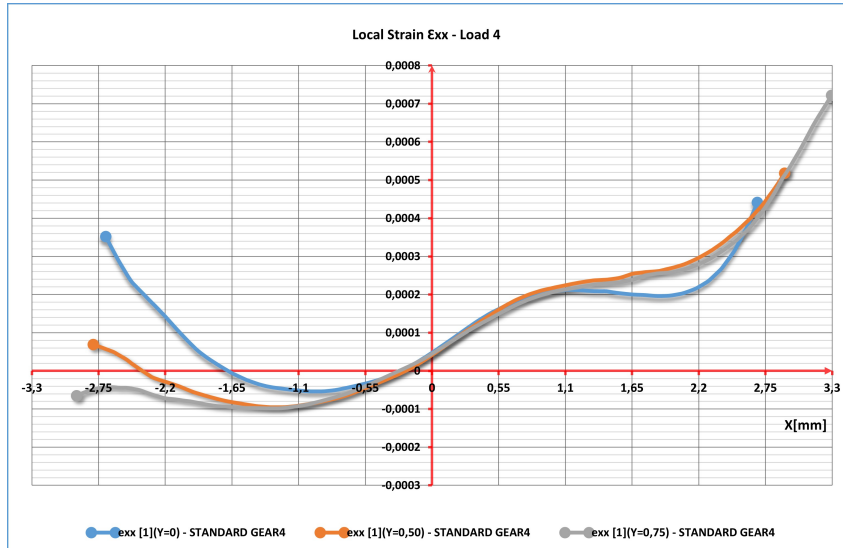


Figure A.56: Local strain ϵ_{xx} - Load 4

A.14.2. Local strain maps ϵ_{yy}

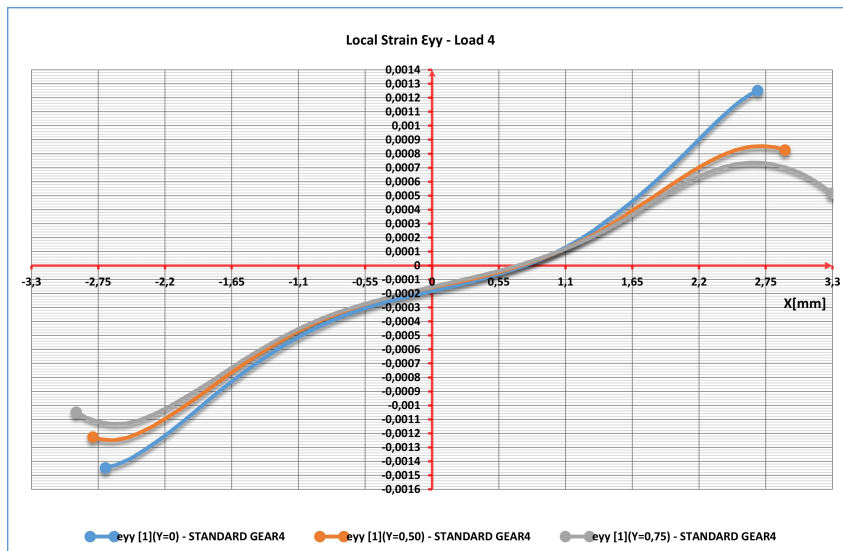


Figure A.57: Local strain ϵ_{yy} - Load 4

A.14.3. Local strain maps ϵ_{xy}

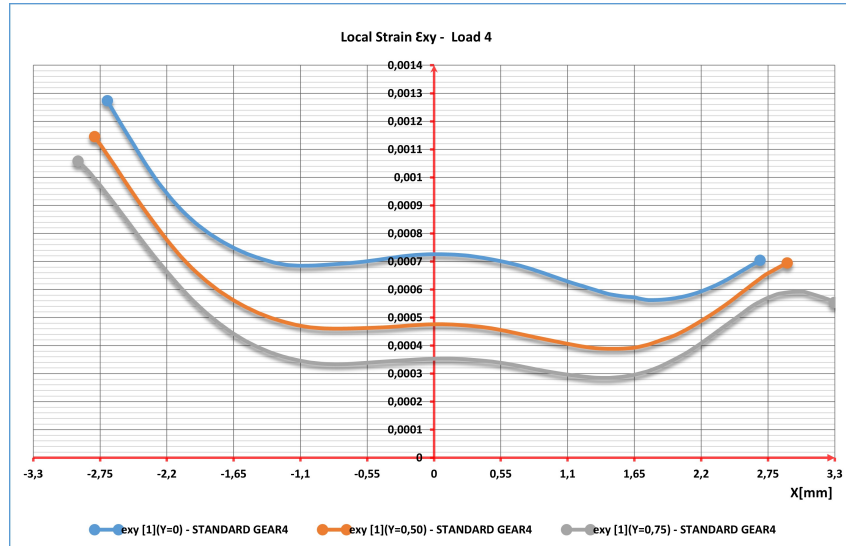


Figure A.58: Local strain ϵ_{xy} - Load 4

A.14.4. Local strain maps ϵ_1

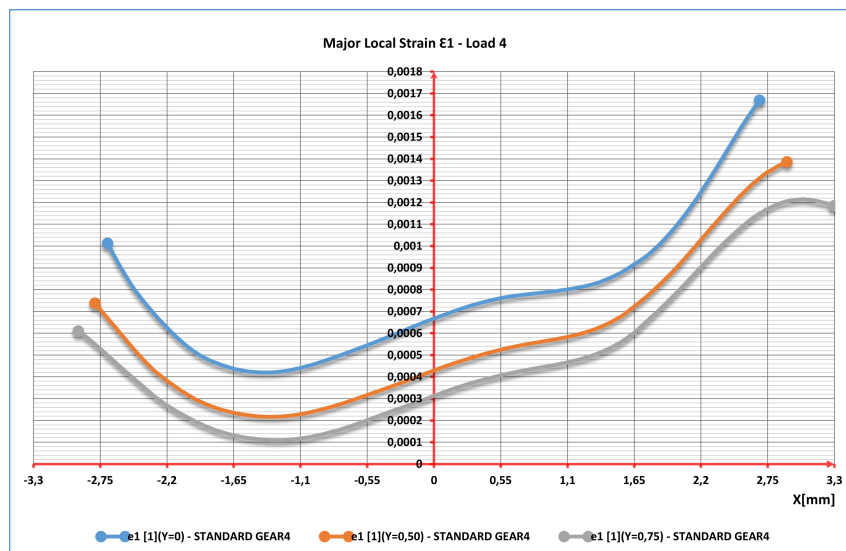


Figure A.59: major principal local strain ϵ_1 - Load 4

A.14.5. Local strain maps γ_1

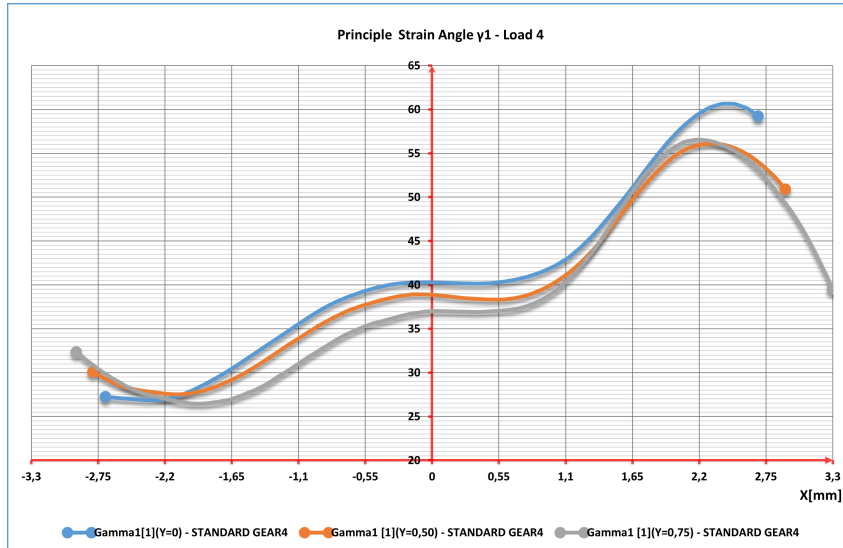


Figure A.60: Principal strain angle γ_1 - Load 4

A.14.6. Local strain maps $1(X = 0)$

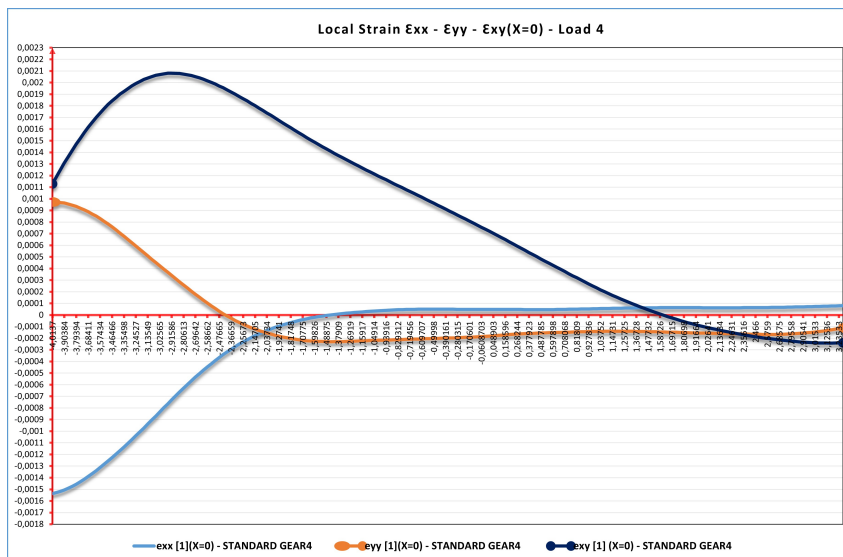


Figure A.61: Local Strain $\epsilon_{xx} - \epsilon_{yy} - \epsilon_{xy}(X=0)$ - Load 4

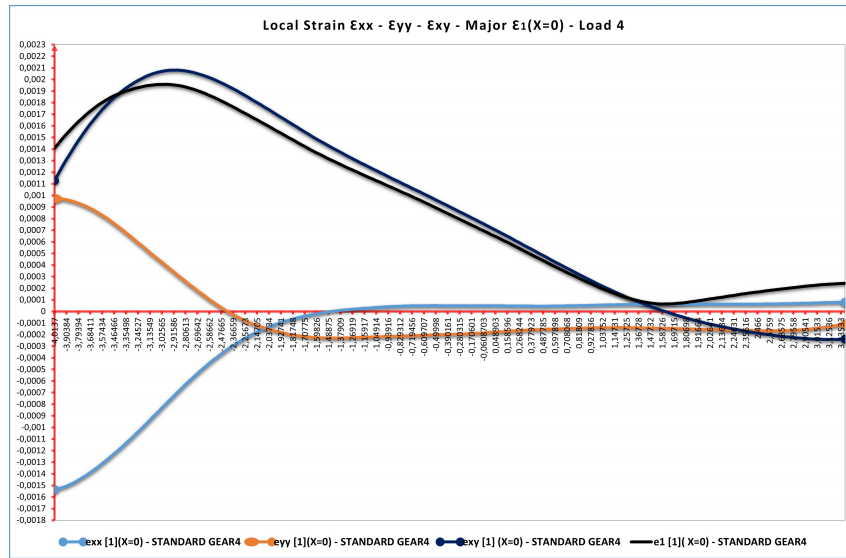


Figure A.62: Local Strain $\epsilon_{xx} - \epsilon_{yy} - \epsilon_{xy} - \text{Major } \epsilon_1(X=0) - \text{Load 4}$

A.15. Thin Rim Gear - Load 3

A.15.1. Local strain maps ϵ_{xx}

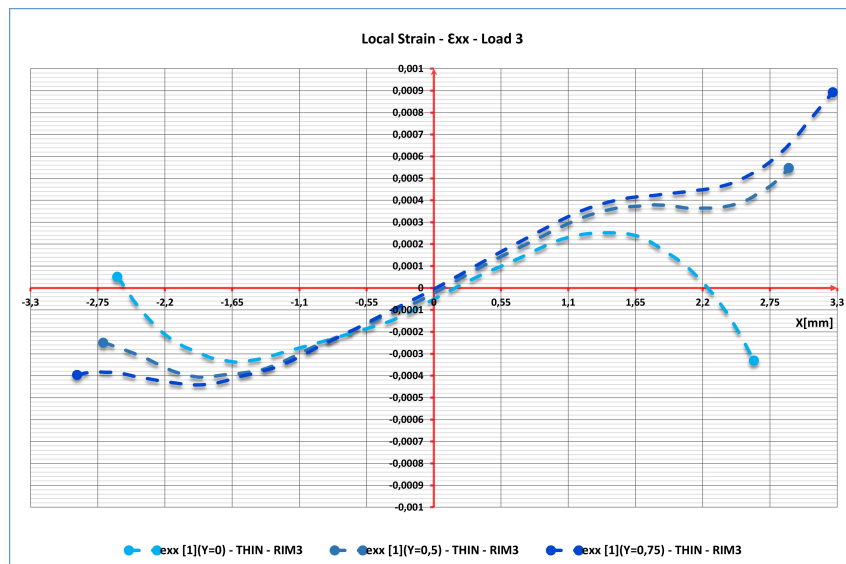


Figure A.63: Local strain $\epsilon_{xx} - \text{Load 3}$

A.15.2. Local strain maps ϵ_{yy}

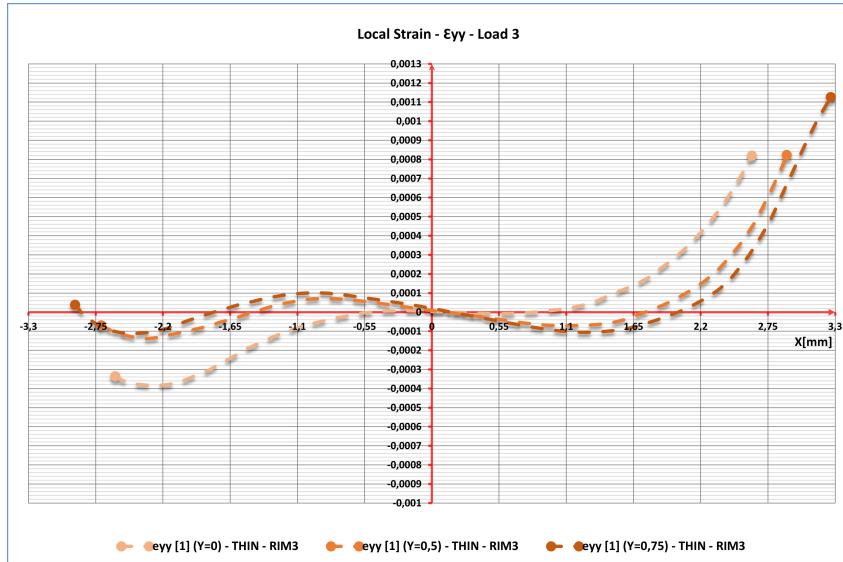


Figure A.64: Local strain ϵ_{yy} - Load 3

A.15.3. Local strain maps ϵ_{xy}

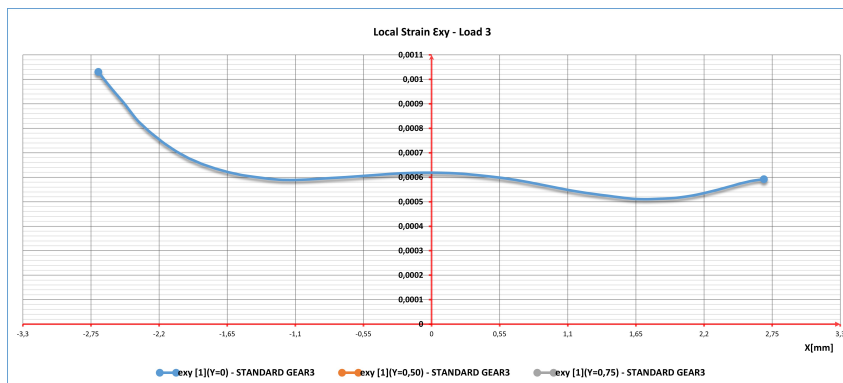


Figure A.65: Local strain ϵ_{xy} - Load 3

A.15.4. Local strain maps γ_1

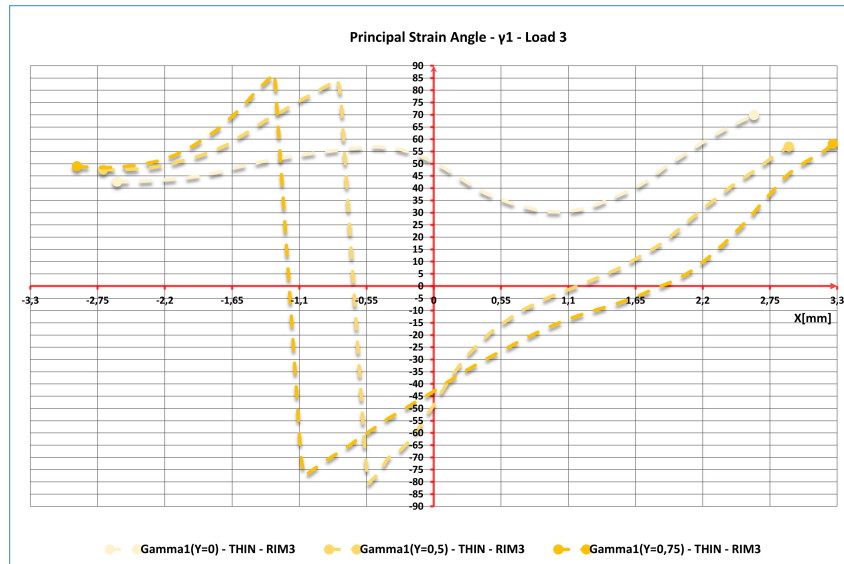


Figure A.66: Principal strain angle γ_1 - Load 3

A.15.5. Local strain maps $\epsilon_1(X = 0)$

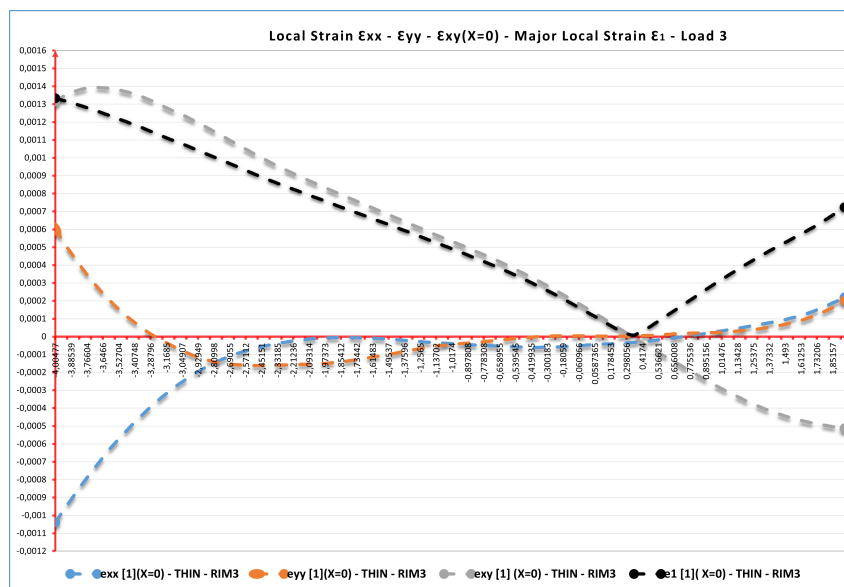


Figure A.67: Local Strain $\epsilon_{xx} - \epsilon_{yy} - \epsilon_{xy}$ - Major $\epsilon_1(X=0)$ - Load 3

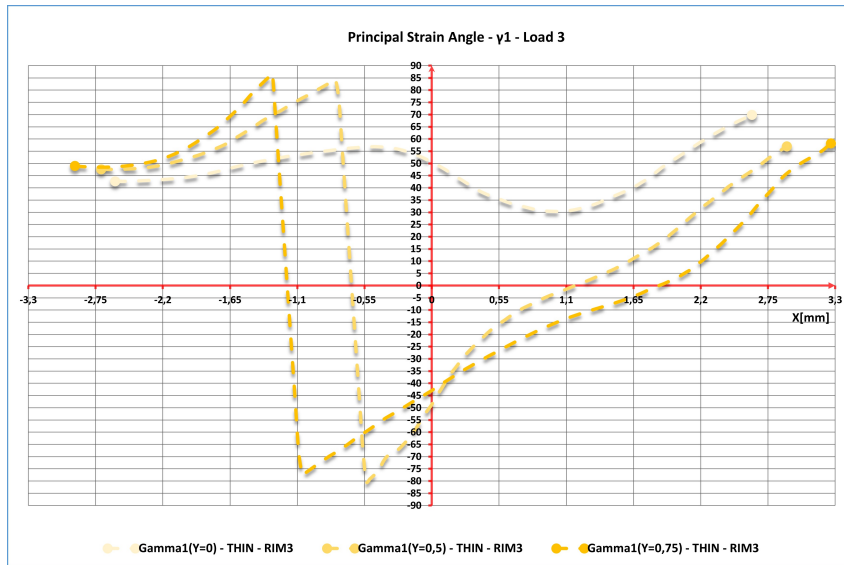


Figure A.68: Principal Strain Angle $\gamma_1(X=0)$ Load 3

A.16. Thin Rim Gear - Load 4

A.16.1. Local strain maps ϵ_{xx}

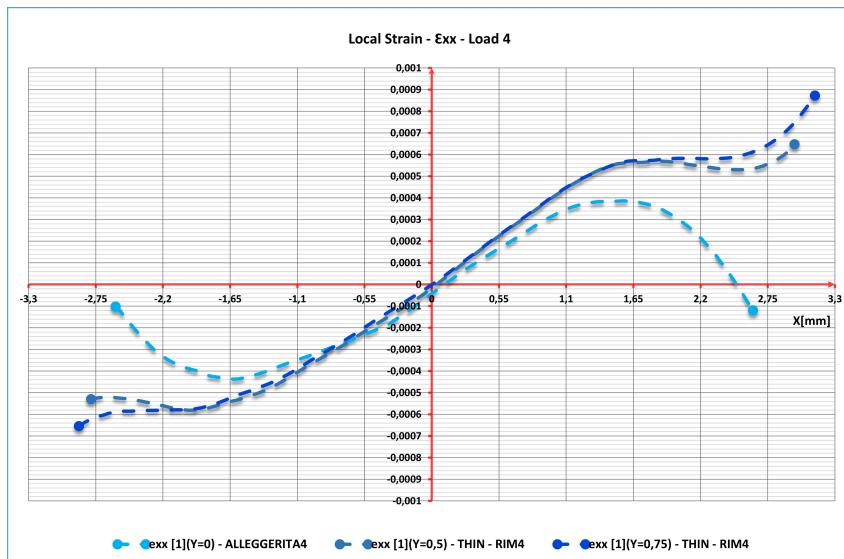


Figure A.69: Local strain ϵ_{xx} - Load 4

A.16.2. Local strain maps ϵ_{yy}

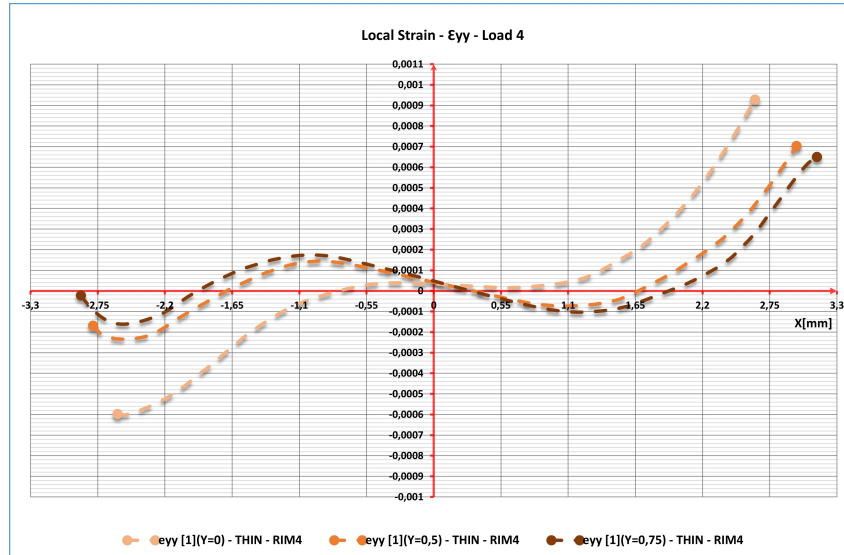


Figure A.70: Local strain ϵ_{yy} - Load 4

A.16.3. Local strain maps ϵ_1

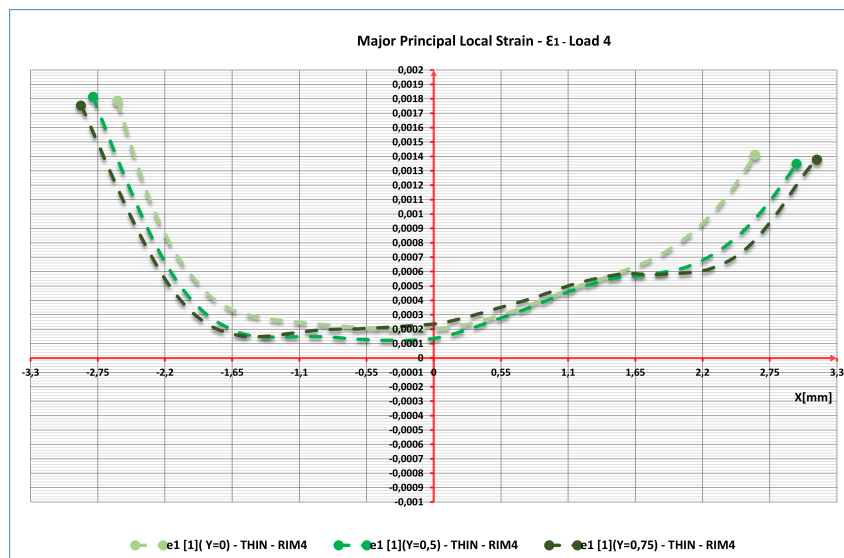


Figure A.71: Major Principal Local strain ϵ_1 - Load 4

A.16.4. Local strain maps γ_1

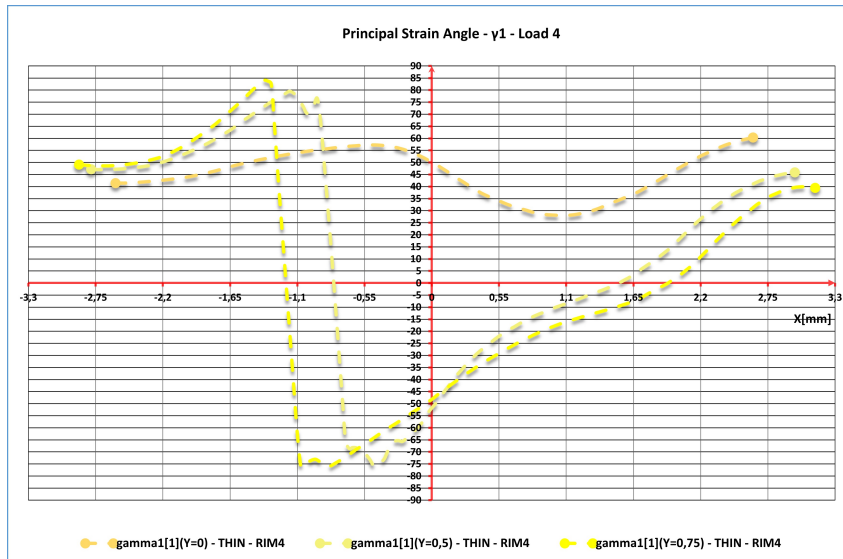


Figure A.72: Principal strain angle γ_1 - Load 4

A.16.5. Local strain maps $\epsilon_1(X = 0)$

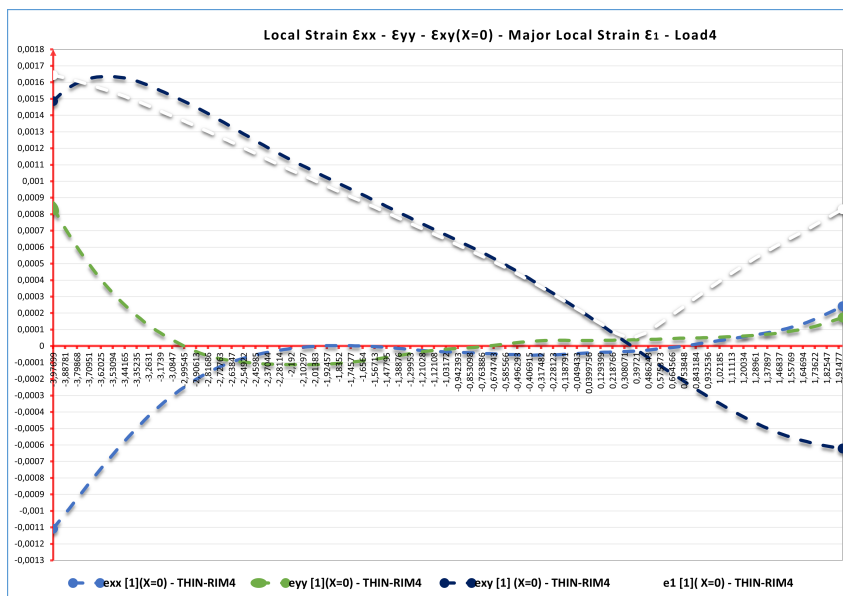


Figure A.73: Local Strain $\epsilon_{xx} - \epsilon_{yy} - \epsilon_{xy}$ - Major Local Strain $\epsilon_1(X=0)$ - Load 4

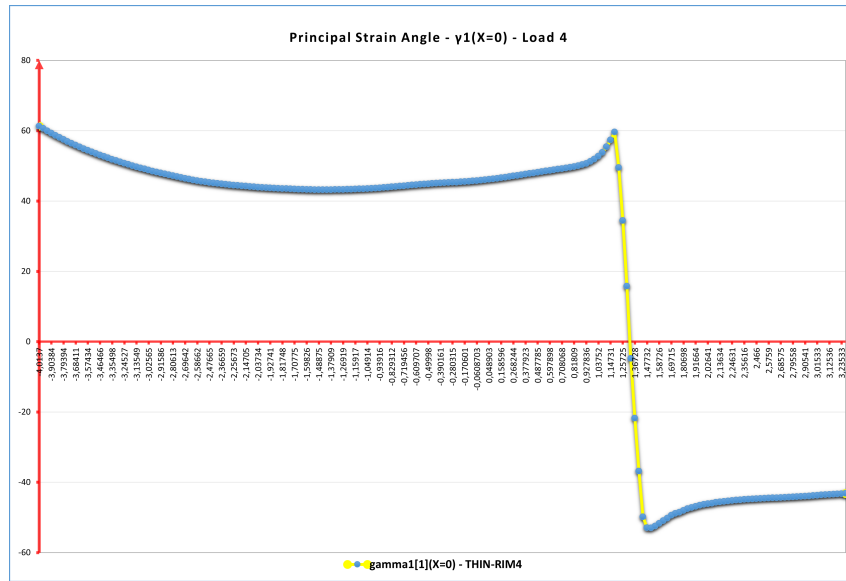


Figure A.74: Principal Strain Angle $\gamma_1(X=0)$ Load 4

A.17. Comparison with FEM results

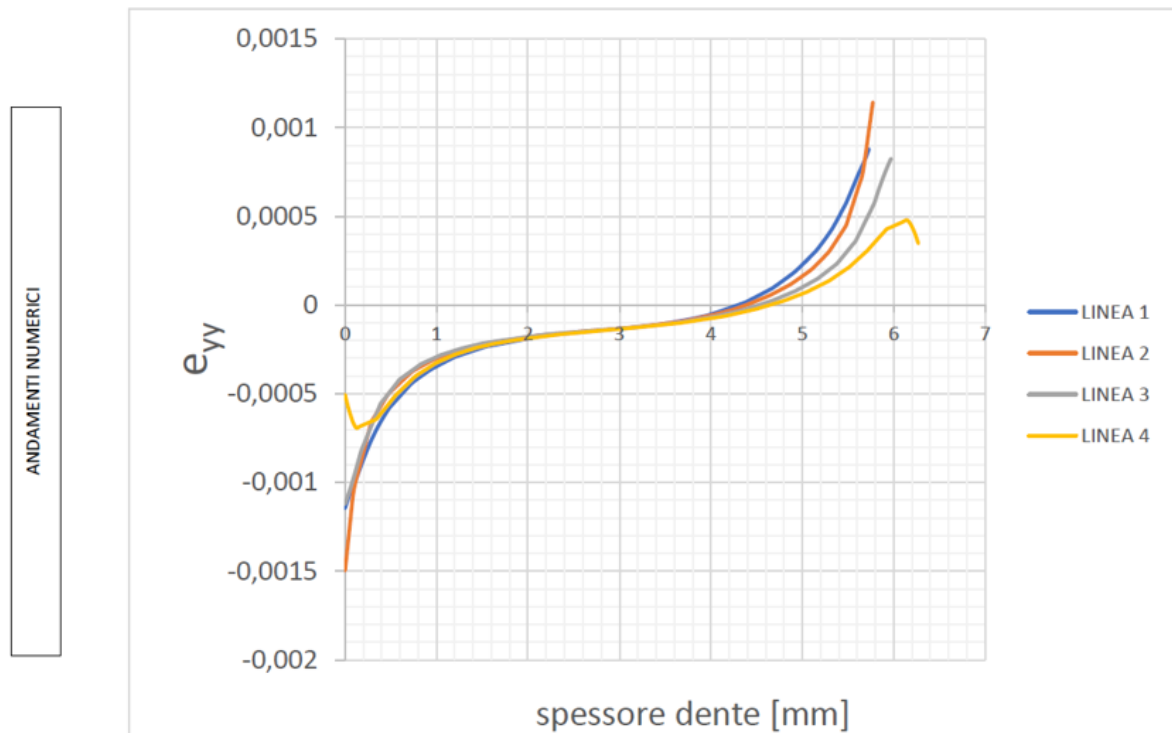


Figure A.75: FEM simulation - Standard Gear - Load 4

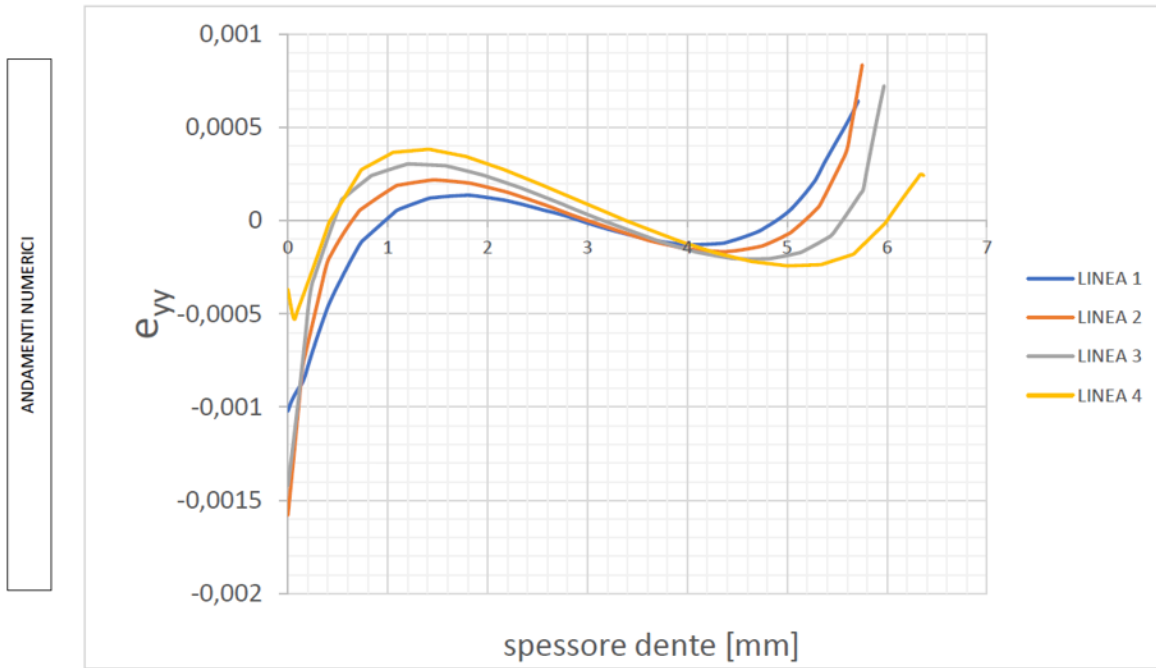


Figure A.76: FEM simulation - Thin-Rim Gear - Load 4

List of Figures

1.1	Types of Residual Stress (from biofotonica.it)	5
1.2	Shot peening process [8]	7
1.3	Distribution of stress in a shot-peened beam with no external Load [8] . . .	7
1.4	Peening continues to protect the surface from fatigue as long as tensile stress from applied load are less than residual stresses. [8]	8
1.5	Tensile and shear stresses cause pits and fatigue cracks.[8]	8
1.6	Application of hole-drilling and ring core methods [18]	9
1.7	Diffractionmeter	11
1.8	Typical thermoelastic image [18]	13
1.9	Thermoelastic response of a plate in uniaxia tension with a central hole [18]	13
1.10	(a) Schematic of holographic interferometry set-up, (b) interference fringes from in-plane displacements of a thin plate, stretched uniformly and (c) fringes from out-of-plane displacements of a disc supported around its circumference and loaded by a force normal to its surface and slightly off-center. [10]	14
1.11	Implementation procedures of 2D-DIC and stereo-DIC techniques [15] . . .	17
1.12	Visualization of subset tracking during movement and deformation [19] . .	18
1.13	Example of typical speckle patterns [12]	19
1.14	Basic principle of subset - based on DIC method [16]	20
1.15	Types of correlation criteria used in DIC [14]	21
1.16	Binocular Stereovision [12]	22
1.17	Epipolar plane [12]	23
1.18	Epipolar line [12]	24
2.1	DIC overview (from isi-sys DIC Setup Guide)	27
2.2	Basler ace ac4096-30um camera	28
2.3	Sensor Characteristics	29
2.4	Camera Characteristics	29
2.5	Hardware triggering (from Application Note AN-1703 Triggering Methods)	30
2.6	Selection of lenses to be used through the Mach Vis software.	31

2.7	Optical parameters of the Rodagon 135 mm lens	31
2.8	Assembly of lenses, cameras and extensive tubes	32
2.9	Control elements front layout of DAQ unit	32
2.10	DAQ-STD-8D	33
2.11	Schematic DAQ Operation (from isi-sys DAQ-unit)	34
2.12	Schematic view of sample image acquisition through 3D-DIC [14]	35
2.13	Improvements in terms of accuracy and precision of DIC [7]	35
2.14	Vic-3D Application Window [20]	36
2.15	Vic-3D start page [20]	36
2.16	The main toolbar [20]	37
2.17	Data Panel [20]	37
2.18	Calibration Panel [20]	38
2.19	Always present output [6]	39
2.20	Strain variables, velocity variables, confidence margin and 2D specific variables [6]	40
2.21	Deformed variables [6]	40
2.22	Technical drawings of standard gear [6]	41
2.23	Technical drawings of thin-rim gear [6]	42
2.24	Painted standard gear	44
2.25	Speckled standard gear	44
2.26	Painted thin-rim gear	45
2.27	Speckled thin-rim gear	45
2.28	Speckled non-shot-peened gear (a) and speckled shot-peened gear (b)	46
2.29	Photo of a speckled standard gear through DIC	47
2.30	Resulting data from Matlab analysis of speckled standard gear	47
2.31	Photo of a speckled thin-rim gear through DIC	48
2.32	Resulting data from Matlab analysis of speckled thin-rim gear	48
2.33	Photo of a speckled shot-peened gear through DIC	49
2.34	Resulting data from Matlab analysis of speckled shot-peened gear	50
2.35	Photo of a speckled shot-peened gear through DIC	51
2.36	Resulting data from Matlab analysis of speckled non-shot-peened gear	52
2.37	Side view of vertical support with mounted gear	53
2.38	Front view of vertical support with mounted gear	53
2.39	Vertical support permanently mounted on the apex of the Instron machine	54
2.40	The punch that will apply different loads to Standard Gear during the bending test	56
2.41	Contact moment between punch and gear	57

2.42	Reference length of the measurements	59
2.43	Main parameters of the target calibration	59
2.44	4-in-1 Calibration Glass Target	60
2.45	Glass target Used during experimentation	60
2.46	Representation of depth of field (f): a) If the lens aperture width is reduced, f has a high numerical value; b) If the lens aperture width is wider, f has a low numerical value. [1]	61
2.47	Brightness and Focus - Standard Gear	62
2.48	Brightness and Focus - Thin Rim Gear	62
2.49	Brightness and Focus - Shot-Peened Gear	63
2.50	Images/Experimental analysis with Digital Image Correlation	64
2.51	Image acquisition and loading application during bending test of a standard gear	65
2.52	Image acquisition and loading application during bending test of a thin-rim gear	65
2.53	Image acquisition and loading application during bending test of a shot-peened gear	66
2.54	Calibration acquisition before of bending test of a non-shot-peened gear	66
2.55	Region Of Interest (ROI) made with VIC 3D Software	67
2.56	Selection of subset parameters with indication of external noise using VIC 3D software	68
2.57	Geometric calculation for the determination of the reference system	69
2.58	Local Reference System - Standard Gear	69
2.59	Local Reference System - Thin Rim Gear	70
3.1	Standard gear: local strain in the X-direction map ϵ_{xx} - Load 4	72
3.2	Standard gear: local strain in the Y-direction map ϵ_{yy} - Load 4	73
3.3	Standard gear: local shear strain map ϵ_{xy} - Load 4	73
3.4	Standard gear: major principal strain map ϵ_1 - Load 4	74
3.5	Standard gear: minor principal strain map ϵ_2 - Load 4	75
3.6	Standard gear: principal strain angle map γ_1 - Load 4	76
3.7	Thin-rim gear: local strain in the X-direction map ϵ_{xx} - Load 4	77
3.8	Thin-rim gear: local strain in the Y-direction map ϵ_{yy} - Load 4	78
3.9	Thin-rim gear: local shear strain map ϵ_{xy} - Load 4	78
3.10	Thin-rim gear: major principal strain map ϵ_1 - Load 4	79
3.11	Thin-rim gear: minor principal strain map ϵ_2 - Load 4	80
3.12	Thin-rim gear: principal strain angle map γ_1 - Load 4	81

3.13	Shot-Peened Gear: local strain in the Y-direction map ϵ_{yy} - Load 3	81
3.14	Shot-Peened Gear: major principal strain map ϵ_1 - Load 3	82
3.15	Shot-Peened Gear: principal strain angle map γ_1 - Load 3	82
3.16	Non-shot-peened gear:local strain in the Y-direction map ϵ_{yy} - Load 3	83
3.17	Non-shot-peened gear:local strain in the Y-direction map ϵ_1 - Load 3	83
3.18	Non-shot-peened gear:local strain in the Y-direction map γ_1 - Load 3	84
3.19	Local Strain - $\epsilon_{xx}(Y=0 \text{ mm})$ - Thin Rim - Standard Gear - Load 4	85
3.20	Local Strain - $\epsilon_{xx}(Y=0,5 \text{ mm})$ - Thin Rim - Standard Gear - Load 4	85
3.21	Local Strain - $\epsilon_{xx}(Y=0,75 \text{ mm})$ - Thin Rim - Standard Gear - Load 4	86
3.22	Local Strain - $\epsilon_{yy}(Y=0 \text{ mm})$ - Thin Rim - Standard Gear - Load 4	87
3.23	Local Strain - $\epsilon_{yy}(Y=0,5 \text{ mm})$ - Thin Rim - Standard Gear - Load 4	87
3.24	Local Strain - $\epsilon_{yy}(Y=0,75 \text{ mm})$ - Thin Rim - Standard Gear - Load 4	88
3.25	Local Strain - $\epsilon_{xy}(Y=0 \text{ mm})$ - Thin Rim - Standard Gear - Load 4	89
3.26	Local Strain - $\epsilon_{xy}(Y=0,5 \text{ mm})$ - Thin Rim - Standard Gear - Load 4	90
3.27	Local Strain - $\epsilon_{xy}(Y=0,75 \text{ mm})$ - Thin Rim - Standard Gear - Load 4	91
3.28	Local Strain - $\epsilon_1(Y=0 \text{ mm})$ - Thin Rim - Standard Gear - Load 4	92
3.29	Local Strain - $\epsilon_1(Y=0,5 \text{ mm})$ - Thin Rim - Standard Gear - Load 4	93
3.30	Local Strain - $\epsilon_1(Y=0,75 \text{ mm})$ - Thin Rim - Standard Gear - Load 4	94
3.31	Local Strain - $\gamma_1(Y=0 \text{ mm})$ - Thin Rim - Standard Gear - Load 4	95
3.32	Local Strain - $\gamma_1(Y=0,5 \text{ mm})$ - Thin Rim - Standard Gear - Load 4	95
3.33	Local Strain - $\gamma_1(Y=0,75 \text{ mm})$ - Thin Rim - Standard Gear - Load 4	96
3.34	Local Strain - $\epsilon_{xx}(X=0 \text{ mm})$ - Local Strain - $\epsilon_{xx}(X=0 \text{ mm})$ Thin Rim - Standard Gear - Load 4	96
3.35	Local Strain - $\epsilon_{yy}(X=0 \text{ mm})$ - $\epsilon_{yy}(X=0 \text{ mm})$ Thin Rim - Standard Gear - Load 4	97
3.36	Local Strain - $\epsilon_{xy}(X=0 \text{ mm})$ - Local Strain - $\epsilon_{xy}(X=0 \text{ mm})$ Thin Rim - Standard Gear - Load 4	98
3.37	Local Major Principal Strain - $\epsilon_1(X=0 \text{ mm})$ - Thin Rim - Standard Gear - Load 4	99
A.1	Standard gear: local strain in the X-direction map ϵ_{xx} - Load 1	105
A.2	Standard gear: local strain in the Y-direction map ϵ_{yy} - Load 1	106
A.3	Standard gear: local shear strain map ϵ_{xy} - Load 1	107
A.4	Standard gear: major principal strain map ϵ_1 - Load 1	108
A.5	Standard gear: minor principal strain map ϵ_2 - Load 1	109
A.6	Standard gear: principal strain angle map γ_1 - Load 1	110
A.7	Standard gear: local strain in the X-direction map ϵ_{xx} - Load 2	111

A.8	Standard gear: local strain in the Y-direction map ϵ_{yy} - Load 2	112
A.9	Standard gear: local shear strain map ϵ_{xy} - Load 2	113
A.10	Standard gear: major principal strain map ϵ_1 - Load 2	114
A.11	Standard gear: minor principal strain map ϵ_2 - Load 2	115
A.12	Standard gear: principal strain angle map γ_1 - Load 2	116
A.13	Standard gear: local strain in the X-direction map ϵ_{xx} - Load 3	117
A.14	Standard gear: local strain in the Y-direction map ϵ_{yy} - Load 3	118
A.15	Standard gear: local shear strain map ϵ_{xy} - Load 3	119
A.16	Standard gear: major principal strain map ϵ_1 - Load 3	120
A.17	Standard gear: minor principal strain map ϵ_2 - Load 3	121
A.18	Standard gear: principal strain angle map γ_1 - Load 3	122
A.19	Thin-rim gear: local strain in the X-direction map ϵ_{xx} - Load 1	123
A.20	Thin-rim gear: local strain in the Y-direction map ϵ_{yy} - Load 1	124
A.21	Thin-rim gear: local shear strain map ϵ_{xy} - Load 1	125
A.22	Thin-rim gear: major principal strain map ϵ_1 - Load 1	126
A.23	Thin-rim gear: minor principal strain map ϵ_2 - Load 1	127
A.24	Thin-rim gear: principal strain angle map γ_1 - Load 1	128
A.25	Thin-rim gear: local strain in the X-direction map ϵ_{xx} - Load 2	129
A.26	Thin-rim gear: local strain in the Y-direction map ϵ_{yy} - Load 2	130
A.27	Thin-rim gear: local shear strain map ϵ_{xy} - Load 2	131
A.28	Thin-rim gear: major principal strain map ϵ_1 - Load 2	132
A.29	Thin-rim gear: minor principal strain map ϵ_2 - Load 2	133
A.30	Thin-rim gear: principal strain angle map γ_1 - Load 2	134
A.31	Thin-rim gear: local strain in the X-direction map ϵ_{xx} - Load 3	135
A.32	Thin-rim gear: local strain in the Y-direction map ϵ_{yy} - Load 3	136
A.33	Thin-rim gear: local shear strain map ϵ_{xy} - Load 3	137
A.34	Thin-rim gear: major principal strain map ϵ_1 - Load 3	138
A.35	Thin-rim gear: minor principal strain map ϵ_2 - Load 3	139
A.36	Thin-rim gear: principal strain angle map γ_1 - Load 3	140
A.37	Shot-Peened Gear: local strain in the Y-direction map ϵ_{yy} - Load 1	141
A.38	Shot-Peened Gear: major principal strain map ϵ_1 - Load 1	141
A.39	Shot-Peened Gear: principal strain angle map γ_1 - Load 1	142
A.40	Shot-Peened Gear: local strain in the Y-direction map ϵ_{yy} - Load 2	142
A.41	Shot-Peened Gear: major principal strain map ϵ_1 - Load 2	143
A.42	Shot-Peened Gear: principal strain angle map γ_1 - Load 2	143
A.43	Non-shot-peened gear:local strain in the Y-direction map ϵ_{yy} - Load 1	144
A.44	Non-shot-peened gear:local strain in the Y-direction map ϵ_1 - Load 1	144

A.45 Non-shot-peened gear:local strain in the Y-direction map γ_1 - Load 1 . . .	145
A.46 Non-shot-peened gear:local strain in the Y-direction map ϵ_{yy} - Load 2 . . .	145
A.47 Non-shot-peened gear:local strain in the Y-direction map ϵ_1 - Load 2 . . .	146
A.48 Non-shot-peened gear:local strain in the Y-direction map γ_1 - Load 2 . . .	146
A.49 Local strain ϵ_{xx} - Load 3	147
A.50 Local strain ϵ_{yy} - Load 3	147
A.51 Local strain ϵ_{xy} - Load 3	147
A.52 major principal local strain ϵ_1 - Load 3	148
A.53 Principal strain angle γ_1 - Load 3	148
A.54 Local Strain $\epsilon_{xx} - \epsilon_{yy} - \epsilon_{xy}(X=0)$ - Load 3	149
A.55 Local Strain $\epsilon_{xx} - \epsilon_{yy} - \epsilon_{xy}$ - Major $\epsilon_1(X=0)$ - Load 3	149
A.56 Local strain ϵ_{xx} - Load 4	150
A.57 Local strain ϵ_{yy} - Load 4	150
A.58 Local strain ϵ_{xy} - Load 4	151
A.59 major principal local strain ϵ_1 - Load 4	151
A.60 Principal strain angle γ_1 - Load 4	152
A.61 Local Strain $\epsilon_{xx} - \epsilon_{yy} - \epsilon_{xy}(X=0)$ - Load 4	152
A.62 Local Strain $\epsilon_{xx} - \epsilon_{yy} - \epsilon_{xy}$ - Major $\epsilon_1(X=0)$ - Load 4	153
A.63 Local strain ϵ_{xx} - Load 3	153
A.64 Local strain ϵ_{yy} - Load 3	154
A.65 Local strain ϵ_{xy} - Load 3	154
A.66 Principal strain angle γ_1 - Load 3	155
A.67 Local Strain $\epsilon_{xx} - \epsilon_{yy} - \epsilon_{xy}$ - Major $\epsilon_1(X=0)$ - Load 3	155
A.68 Principal Strain Angle $\gamma_1(X=0)$ Load 3	156
A.69 Local strain ϵ_{xx} - Load 4	156
A.70 Local strain ϵ_{yy} - Load 4	157
A.71 Major Principal Local strain ϵ_1 - Load 4	157
A.72 Principal strain angle γ_1 - Load 4	158
A.73 Local Strain $\epsilon_{xx} - \epsilon_{yy} - \epsilon_{xy}$ - Major Local Strain $\epsilon_1(X=0)$ - Load 4	158
A.74 Principal Strain Angle $\gamma_1(X=0)$ Load 4	159
A.75 FEM simulation - Standard Gear - Load 4	159
A.76 FEM simulation - Thin-Rim Gear - Load 4	160

List of Tables

2.1	Standard Gear Geometry	42
2.2	Thin-rim Gear Geometry	43
2.3	3D Digital Image Correlation Parameters	64

List of Symbols

Variable	Description	SI unit
\boldsymbol{u}	solid displacement	m
\boldsymbol{u}_f	fluid displacement	m

Acknowledgements

Questo capitolo risulta essere il più difficile da scrivere perchè non si imparano sui libri le parole giuste da dire in questi momenti. E forse, proprio per questo, inizierò in un modo inusuale, ringraziando me stesso. Questo percorso è stato lungo e faticoso, ma se posso stringere questa tesi in mano è principalmente grazie alla mia determinazione, la mia forza di volontà, la mia voglia di farcela e non arrendersi mai, anche di fronte ai molti ostacoli che si sono presentati. Devo ammettere, però, che al mio fianco ho avuto delle persone speciali senza le quali non sarei in piedi ora, letteralmente. Grazie alla mia famiglia per averci creduto fino alla fine, questo traguardo lo dedico a mia madre: grazie ai suoi sacrifici siamo grandi esseri umani. Ringrazio mia sorella per avermi spinto a non mollare nei momenti più difficili, ad essere sempre me stesso. Grazie per i suoi abbracci e il suo supporto morale. Ringrazio alla mia fidanzata Giada Ferrero che mi ha donato la sua pazienza, il suo amore e la sua determinazione per lottare per questo sogno. Grazie alla vita che mi ha donato la possibilità di conoscere bellissime persone che mi hanno insegnato il significato della vita, dell'amicizia e dell'eccellenza. Ringrazio i miei relatori che mi hanno portato ad imparare in ogni momento, mi hanno sempre sostenuto e hanno creduto in me sin dall'inizio. In particolare a Luca Corsaro, che è stato al mio fianco in tutto questo percorso di tesi. Si è sempre dimostrato un amico che mi ha donato tanta conoscenza e tante allegrie assieme. Ad Andrea Ferrarese che mi ha sostenuto in questo progetto complicato, ma si è mostrato sempre disponibile a donare le sue conoscenze sulla tecnologia. Grazie mille a Francesca Curà che dal primo momento in cui l'ho conosciuta è stata una mentor, che mi ha fatto capire che il valore di una persona non è un voto ma un sorriso. La ringrazio per ogni sua parola.

Grazie Politecnico per avermi regalato questa bella esperienza che porterò sempre nel cuore...

